



TAMPEREEN TEKNILLINEN YLIOPISTO
TAMPERE UNIVERSITY OF TECHNOLOGY

Juho Sormunen

TRANSIENT LOAD SIMULATION OF FORWARDER REAR
FRAME

Master of Science Thesis

Examiner: Professor Reijo Kouhia
Examiner and topic approved by the
Council of the Faculty of Engineer-
ing Sciences meeting on February
3rd 2016

ABSTRACT

JUHO SORMUNEN: Transient Load Simulation of Forwarder Rear Frame

Tampere University of Technology

Master of Science Thesis, 94 pages, 7 Appendix pages

June 2016

Master's Degree Programme in Mechanical Engineering

Major: Applied Mechanics and Thermal Sciences

Examiner: Professor Reijo Kouhia

Keywords: Explicit time integration, FEM, Forwarder, John Deere, LS-DYNA, Transient

One difficulty in the design of load bearing components of mobile machines is the transient and non-linear nature of loads acting on them. In addition to the dynamic characteristics of the machine, the magnitude of these loads also depends on the properties of the ground the machine is operating in. A common method for tracking these loads is to use strain gauges and force transducers on a physical test machine.

An alternative method for determining the transient loads by means of a mathematical model that intends to describe the response of John Deere 1010E forwarder as it crosses a test track is utilized in this thesis. The model is based on finite element method and it is solved using explicit time integration and LS-DYNA® software. The most challenging aspect of the simulation turned out to be the modeling of the tires, specifically the control of their high frequency vibrations.

The evaluation of the machine response using a mathematical model, at its best, is faster, cheaper and more versatile compared to physical testing. The model will be validated by comparing simulation results to measured results.

As a result of this thesis a model capable of replicating the real world with a reasonable accuracy was obtained. The forces acting on tires, which can be considered the most important results of this work, can be used as boundary conditions in consequent analyses, such as fatigue simulation. It was found out that the global stress state in the load space is dominated, at least at high loads, by the forces exerting from the cargo and not much affected by the tire forces. Tire forces do, however, affect the stress state of the welded frame itself.

In the future, this model can be used early in the design phase as a basis for a model that helps in determining the response of different machine configurations at different terrains and loading conditions.

TIIVISTELMÄ

JUHO SORMUNEN: Kuormatraktorin takarungon aikariippuvaisten kuormien simulointi

Tampereen teknillinen yliopisto

Diplomityö, 94 sivua, 7 liitesivua

Kesäkuu 2016

Konetekniikan diplomi-insinöörin tutkinto-ohjelma

Pääaine: Sovellettu mekaniikka ja lämpötekniikka

Tarkastaja: Professori Reijo Kouhia

Avainsanat: Aikariippuvainen, Eksplisiittinen aikaintegrointi, FEM, John Deere, Kuormatraktori, LS-DYNA

Liikkuvien työkonoiden kuormaa kantavien osien mitoituksessa yhtenä ongelmana on usein rakenteeseen kohdistuvien kuormitusten ajasta riippuva ja epälineaarinen luonne, joiden suuruus riippuu koneen dynaamisten ominaisuuksien lisäksi myös maastosta, jossa se työskentelee. Yleisin menetelmä saada kuormitukset selville on anturoida testikone venymäliuskein sekä voima-anturein.

Tässä työssä tarkastellaan kuormitusten selvittämiseksi vaihtoehtoisia menetelmiä rakentamalla matemaattinen malli, jolla pyritään kuvaamaan John Deere 1010E kuormakoneen takarunkoon välittyviä voimia, kun sillä ajetaan testiradan yli. Malli perustuu elementtimenetelmään ja se ratkaistaan käyttäen eksplisiittistä aikaintegrointia ja LS-DYNA® -ohjelmistoa. Simuloinnin haastavimmaksi osioksi osoittautui renkaiden mallinnus, erityisesti niiden korkeataajusten värähtelyjen hallinnan osalta.

Matemaattisella mallilla kuormitusten arviointi on parhaimmillaan nopeampaa, halvempaa ja monipuolisempaa kuin fyysisellä mittauksella. Laskentamalli validoidaan vertaamalla laskennallisia tuloksia fyysisestä mallista mitattuihin arvoihin.

Tuloksena työstä saatiin kohtuullisella tarkkuudella reaali-aikaa kuvaava malli. Renkaihin kohdistuvia voimia, joita voidaan pitää työn tärkeimpinä tuloksina, voidaan käyttää reunaehtoina seuraavissa analyyseissä, kuten väsymissimuloinneissa. Työssä saatiin selville, että kuormatilan jännityskenttään vaikuttaa, ainakin suurilla kuormilla, enimmäkseen vain kuorman painosta aiheutuvat voimat eivätkä niinkään renkaista johtuvat voimat. Rengasvoimat kuitenkin vaikuttavat hitsatun takarungon jännitystilaan.

Tulevaisuudessa mallia voidaan käyttää pohjana aikaisen suunnitteluvaiheen aputyökätluna määrittämään erilaisten rakenteiden vastetta erilaisissa kuormitusympäristöissä.

PREFACE

This thesis was done for John Deere Forestry Oy by request of Jouni Valkila, whom I would like to thank for providing such an interesting and challenging subject.

I would also like to thank Prof. Reijo Kouhia for guiding me through the writing process and providing excellent assistance for the thesis, especially regarding the theoretical section of this report.

Finally I would like to thank my fiancée for the patience and support during the endless hours and long nights of writing this thesis.

Tampere, 30.6.2016

Juho Sormunen

CONTENTS

1.	INTRODUCTION	1
1.1	Motivation for analysis.....	1
1.2	John Deere Forestry Oy.....	2
1.3	Cut to length forestry equipment.....	2
1.4	Structure of the report	3
2.	COMPUTATIONAL METHOD	4
2.1	Software	4
2.1.1	ANSYS®	4
2.1.2	LS-DYNA®	5
2.2	Validation and verification.....	5
2.3	Finite element method.....	6
2.4	Time integration	6
2.4.1	Implicit method	6
2.4.2	Explicit method.....	7
2.4.3	Time step controls	9
2.5	Contact algorithms	11
2.6	Dynamic relaxation	12
2.7	Elements	13
2.7.1	Solid	16
2.7.2	Shell	18
2.8	Energy conservation	24
3.	FIELD TEST	26
3.1	Test machine	26
3.2	Test track	26
3.3	Test loads.....	28
3.4	Measured quantities.....	28
3.5	Test results.....	28
4.	MODEL	31
4.1	Bogie	32
4.2	Boom	33
4.3	Bump track	34
4.4	Front frame.....	35
4.5	Load space.....	36
4.6	Logs.....	36
4.7	Middle joint	38
4.8	Rear frame	39
4.9	Tires.....	42
4.9.1	Mesh density	43
4.9.2	Material properties	44

4.9.3	Damping.....	47
4.9.4	Inflation.....	48
4.9.5	Cross-section layup.....	49
4.9.6	Static testing.....	53
4.9.7	Friction.....	55
4.10	Analysis sequence.....	55
5.	RESULTS.....	57
5.1	Tire forces.....	57
5.1.1	12 ton.....	59
5.1.2	9 ton.....	64
5.1.3	Unloaded.....	66
5.2	Global stress state.....	69
5.3	Deformations.....	71
5.4	Solution accuracy.....	73
5.4.1	Energy conservation.....	73
5.4.2	Floating point number accuracy.....	75
5.4.3	Mass scaling.....	75
5.4.4	Tire friction.....	77
5.5	Computing time.....	79
6.	SUGGESTED FURTHER WORK.....	80
6.1	Cargo loading.....	80
6.2	Collision simulation.....	80
6.3	Implicit dynamic fatigue model.....	80
6.4	Other machines.....	81
6.5	Power train.....	81
6.5.1	Differential.....	81
6.5.2	Torque limiter.....	83
6.6	Special terrains.....	84
6.7	Tire model improvement.....	85
7.	SUMMARY.....	86
	REFERENCES.....	88
APPENDIX A	GENERAL CONTROLS, LS-DYNA INPUT.....	1
APPENDIX B	MANUAL INPUT, RELATIVE DAMPING.....	2
APPENDIX C	MANUAL INPUT, MASS DAMPING.....	3
APPENDIX D	MANUAL INPUT, DIFFERENTIAL GEAR.....	4
APPENDIX E	MANUAL INPUT, TORQUE LIMITER.....	6
APPENDIX F	ANALYSIS WALKTHROUGH.....	7

LIST OF FIGURES

Figure 1.1.	John Deere 1010E forwarder, 6 wheel configuration [33].....	1
Figure 2.1.	Calculation process of a single cycle (time step) in explicit analysis [46 p. 620]. The starting point for the algorithm does not necessarily have to be in the position shown by this figure; it can be changed based on type of initial conditions used [58 p. 21].....	8
Figure 2.2.	Principle of penalty based contact formulation [4].	12
Figure 2.3.	Stress components in 3D case [3].	14
Figure 2.4.	Local coordinate parameters (ξ , η and ζ) and geometry of eight node solid hexahedral DYNA3D element [46 p. 52]. Each node has three translational degrees of freedom (DOFs) which results as a total of 24 DOFs for a single element.	16
Figure 2.5.	Displacements and force resultants in a shell with supports and loads independent of y-coordinate, adapted from [68 p. 326].....	19
Figure 2.6.	Construction of the embedded element coordinate system [46 p. 144].....	22
Figure 2.7.	Local coordinate system node numbering for 4-noded shell element.....	23
Figure 2.8.	The hourglass effect of a reduced integration element subjected to pure bending [19]. The length of both dotted lines (lines drawn from integration point) remain unchanged, thus resulting as zero stresses.....	25
Figure 3.1.	Bump track general view. Driving direction shown by red arrow. Bumps are numbered to be referenced later in the results.....	27
Figure 3.2.	Detailed view of the bump.	27
Figure 3.3.	Bump track dimensions.....	28
Figure 3.4.	Notation of tires.....	29
Figure 4.1.	Mesh for the entire simulation model has approximately 151 thousand elements. The initial position of the machine is shown.....	32
Figure 4.2.	Mesh for bogie.	32
Figure 4.3.	Approximate boom positions with different loads.....	33
Figure 4.4.	Simplified boom model (position according to 12 ton configuration shown in Figure 4.3 a)) and joint types used in it.	34
Figure 4.5.	Mesh for bump track.....	35
Figure 4.6.	All DOFs are fixed at the highlighted edges (blue) of bump track. The structure has RHS tubes as reinforcement at these edges even though they are not visible in Figure 3.1.	35
Figure 4.7.	Mesh for load space.....	36

Figure 4.8.	<i>Pine logs used in test runs have diameters ranging from 200 mm at top to 500 mm at base. Length for all logs is approximately 5200 mm.</i>	37
Figure 4.9.	<i>Log dimensions in simulation.</i>	37
Figure 4.10.	<i>Mesh used in modeling logs. One section is removed to view mesh inside the log.</i>	37
Figure 4.11.	<i>Mesh for middle joint.</i>	38
Figure 4.12.	<i>Joints in middle joint. Steering cylinders are modeled using spherical joints (rotational DOFs free, translational DOFs fixed).</i>	38
Figure 4.13.	<i>Coarse and fine meshes.</i>	40
Figure 4.14.	<i>First three non-rigid eigenmodes of rear frame.</i>	40
Figure 4.15.	<i>Studied tire, 710/40-24.5/20 Nokian Forest King F2 SF TT [50].</i>	43
Figure 4.16.	<i>Coarse mesh on left, fine mesh on right.</i>	44
Figure 4.17.	<i>Tire sidewall eigenmode leading to instabilities.</i>	48
Figure 4.18.	<i>Tire instability (all front tires) leading to rupture (RF tire) can be seen as sidewall mesh distortion.</i>	48
Figure 4.19.	<i>Mesh of tire model with solid treads. Nodes of solid and shell tire components are merged.</i>	50
Figure 4.20.	<i>Comparison of contact pressures of different tread modeling techniques (100 kN compressing load). Pressure is higher with solid treads since the contacting area is smaller.</i>	50
Figure 4.21.	<i>Comparison of deflected states on different tread modeling techniques (from two perpendicular cross sections).</i>	51
Figure 4.22.	<i>Default fiber orientation is tangential to the red line.</i>	52
Figure 4.23.	<i>Layers of tire laminate (layer thicknesses are out of scale for better visualization).</i>	52
Figure 4.24.	<i>Analysis sequence. Zero time is set to the phase when velocities are applied (this is done only for convenience since the results of the damping phase prior to setting initial velocities are not interesting).</i>	56
Figure 5.1.	<i>The right-side tires of the rear frame crossing bump no. 1 at $t \approx 2.7$ s.</i>	61
Figure 5.2.	<i>Von Mises stresses of the rear frame before first impact and at the impact (see Chart 5.18 for notation).</i>	70
Figure 5.3.	<i>Von Mises stresses due to log-load space interactions after applying gravity. See Section 5.3 for more information on forces acting on load space.</i>	71
Figure 5.4.	<i>The rearmost posts bend approximately 55 mm (laterally) due to forces generated by the logs and the grapple.</i>	71
Figure 5.5.	<i>Deformations viewed from another angle. Initial state (see Chart 5.19 for notation) shown on left and deformed state, after applying gravity, shown on right.</i>	72

<i>Figure 5.6.</i>	<i>Vertical deflections at $t=0$ s. Rear frame vertical movement is higher as the mass of the rear frame is higher than that of the front frame.....</i>	<i>72</i>
<i>Figure 5.7.</i>	<i>Elements with mass scaling (zero in blue elements and maximum in red elements).</i>	<i>76</i>
<i>Figure 6.1.</i>	<i>Components of differential gear.....</i>	<i>82</i>
<i>Figure 6.2.</i>	<i>Flowchart clarifying the ideal torque limiter.....</i>	<i>84</i>
<i>Figure 6.3.</i>	<i>Mesh at tire cross section.....</i>	<i>85</i>
<i>Figure 6.4.</i>	<i>Highly distorted elements at cross section of a tire inflated to 400 kPa and compressed using a force of 100 kN.....</i>	<i>85</i>

LIST OF TABLES

<i>Table 2.1.</i>	<i>Calculation of characteristic dimensions for low order elements with equal edge lengths [5; 46 pp. 599-601].</i>	<i>10</i>
<i>Table 4.1.</i>	<i>Measured weights of test machine components [65].</i>	<i>31</i>
<i>Table 4.2.</i>	<i>Minimum allowed element dimensions to reach a time step of 2 μs, based on Table 2.1 and Equation (9).</i>	<i>31</i>
<i>Table 4.3.</i>	<i>Results of mesh convergence study.</i>	<i>44</i>
<i>Table 4.4.</i>	<i>Rubber orthotropic properties (E and G in GPa).</i>	<i>46</i>
<i>Table 4.5.</i>	<i>Comparison of normalized computing times and deflections between tread modeling styles.</i>	<i>51</i>
<i>Table 4.6.</i>	<i>Properties of tire layers. Fiber orientations shown with respect to default orientation (Figure 4.22).</i>	<i>52</i>
<i>Table 5.1.</i>	<i>Studied friction coefficient combinations and resulting force peaks (12 ton load case) in kN. Combination 6-4 is used in the simulation model.</i>	<i>77</i>
<i>Table 7.1.</i>	<i>Comparison of measured and simulated radial force peaks [kN].</i>	<i>86</i>

LIST OF CHARTS

Chart 2.1.	<i>Using a high damping value the static equilibrium is found significantly faster compared to a low damping value.....</i>	13
Chart 3.1.	<i>Rear frame wheel radial reaction forces measured at the test track with 12 ton load.</i>	29
Chart 3.2.	<i>Results zoomed to crossing of the first bump track.</i>	30
Chart 4.1.	<i>Converging behavior of natural modes shown in Figure 4.14.....</i>	41
Chart 4.2.	<i>Resulting number of elements for each studied global element size.</i>	41
Chart 4.3.	<i>Measured static radii and trend lines crossing at origin.</i>	54
Chart 4.4.	<i>Comparison of simulation results to measured data show satisfactory agreement.....</i>	54
Chart 5.1.	<i>Measured radial reaction forces of RF tire compared for different load cases.</i>	58
Chart 5.2.	<i>Simulated radial reaction forces of RF tire compared for different load cases.</i>	58
Chart 5.3.	<i>The horizontal forces of the right-side tires of the rear-frame.....</i>	60
Chart 5.4.	<i>Sum of horizontal forces of right hand side tires (RF and RR in Figure 3.4).....</i>	61
Chart 5.5.	<i>The vertical forces of the right-side tires of the rear-frame.....</i>	62
Chart 5.6.	<i>RF tire radial reactions. Simulated radial peak force of RF tire hitting bump no. 1 is 5 % larger than the measured one.</i>	63
Chart 5.7.	<i>LF tire radial reactions. Simulated radial peak force of LF tire hitting bump no. 2 is 27 % larger than the measured one.</i>	63
Chart 5.8.	<i>LR tire radial reactions.</i>	64
Chart 5.9.	<i>RR tire radial reactions.</i>	64
Chart 5.10.	<i>RF tire radial reactions, 9 ton load.....</i>	65
Chart 5.11.	<i>LF tire radial reactions, 9 ton load.</i>	65
Chart 5.12.	<i>LR tire radial reactions, 9 ton load.</i>	66
Chart 5.13.	<i>RR tire radial reactions, 9 ton load.....</i>	66
Chart 5.14.	<i>RF tire radial reactions, unloaded case.</i>	67
Chart 5.15.	<i>LF tire radial reactions, unloaded case.</i>	67
Chart 5.16.	<i>RR tire radial reactions, unloaded case.</i>	68
Chart 5.17.	<i>LR tire radial reactions, unloaded case.</i>	68
Chart 5.18.	<i>Maximum von Mises stress time history of the rear frame.....</i>	69
Chart 5.19.	<i>Von Mises stress time history of the load space.</i>	70
Chart 5.20.	<i>Different forms of energies as fractions of total energy throughout the simulation.</i>	74
Chart 5.21.	<i>Energy ratio.....</i>	74
Chart 5.22.	<i>Comparative results of horizontal force on the right front tire of rear frame for single and double precision solutions. Note that</i>	

	<i>these results are from a model used early in the simulation process.</i>	
	<i>The results of this chart therefore differ from results presented in</i>	
	<i>Section 5.1.</i>	<i>75</i>
<i>Chart 5.23.</i>	<i>Added mass as a percentage of total mass.</i>	<i>76</i>
<i>Chart 5.24.</i>	<i>Comparison of effect of different friction coefficient combinations</i>	
	<i>of Table 5.1 to RF radial tire forces.</i>	<i>78</i>
<i>Chart 5.25.</i>	<i>Comparison of effect of different friction coefficient combinations</i>	
	<i>of Table 5.1 to LF radial tire forces.</i>	<i>78</i>

NOMENCLATURE

Abbreviations

ALE	Arbitrary Lagrangian Eulerian
CAD	Computer Aided Design
CFL	Courant-Friedrichs-Lewy
CoG	Center of Gravity
CR	Corotational
CTL	Cut to Length
DEM	Discrete Element Method
DOF	Degree of Freedom
FEM	Finite Element Method
FMG	Forest Machine Group
FOPS	Falling Object Protection System
HHT	Hilber-Hughes-Taylor
LF	Left Front
LMF	Lagrange Multiplier Formulation
LR	Left Rear
MPP	Massively Parallel Processing
OSU	Objective Stress Updates
PCG	Preconditioned Conjugate Gradient
RF	Right Front
ROPS	Rollover Protection System
RR	Right Rear
SASI	Swanson Analysis System Inc.
SRI	Selective Reduced Integration

Latin letters

A	Area of the element
\mathbf{A}	General vector
b	Body force
$[B]$	Linear strain-displacement transformation matrix
c	Speed of sound
C_{01}, C_{10}	Mooney-Rivlin material parameters
$[C]$	Damping matrix
$[D]$	Elasticity matrix
d	Decay constant
\mathbf{e}	Unit vector in corotational coordinate system
E	Elastic modulus, System energy
f	Time step safety factor
$\mathbf{f}(t)$	External load vector
$\mathbf{F}(t)$	Total load vector
G	Shear modulus
$[G]$	Non-linear strain-displacement transformation matrix
h	Element characteristic dimension
J_1, J_2, J_3	Deviatoric strain invariants
J	Determinant of Jacobian matrix
$[J]$	Jacobian matrix
$[K(\mathbf{x})]$	Stiffness matrix

L	Shell dimension
M	Shell bending moment
m	Shell inertial force
$[M]$	Mass matrix
N	Shape/interpolation function
$[N]$	Shape function matrix (or interpolation function matrix)
P	Shell membrane force
\mathbf{r}, \mathbf{s}	Vectors in shell element
S	Shell shear force
$[S]$	2 nd Piola-Kirchhoff stress matrix
Δt	Time step
t	Time, shell thickness
$[T]$	Transformation matrix for shell element
\mathbf{u}	Global displacement vector
u, v, w	Displacements in global Cartesian coordinate directions
V	Volume
w	Weight factor in numerical integration (Gaussian quadrature rule)
W	Strain energy function
\mathbf{x}	Nodal displacement vector
x, y, z	Cartesian coordinate directions

Greek letters

β	Newmark parameter
γ	Newmark parameter, Shear strain
Δ	Coefficient in orthotropic elasticity matrix
ε	Strain
κ	Shear stress correction factor for shells
λ	Lamé constant
μ	Lamé constant, Coefficient of friction
ν	Poisson's ratio
ξ, η, ζ	Element local coordinates
ρ	Density
σ	Stress
φ	Elemental damping
ϕ	Angular displacement
ω	Angular velocity

Sub-/superscripts

-1	Matrix inverse
0	Initial
<i>cont</i>	Contact
<i>d</i>	Dynamic
<i>damp</i>	Damping
<i>e</i>	Elemental
<i>f</i>	Friction
<i>hg</i>	Hourglass
<i>I</i>	Notation for summation over shell element nodes
<i>int</i>	Internal
<i>i, j, k</i>	Tensor components

<i>kin</i>	Kinetic
<i>m</i>	Midsurface
<i>n</i>	Normal
<i>p</i>	Penalty
<i>s</i>	Static
<i>t</i>	Time
Δt	Time step
<i>T</i>	Matrix transpose
<i>w</i>	Work
Accents	
.	First time derivative
..	Second time derivative
^	Local (elemental)

1. INTRODUCTION

The purpose of this work is to build a simulation model that is capable of replicating the reaction forces measured from physical field test of John Deere 1010E forwarder (Figure 1.1) during June 2015. If results are consistent, the resulting simulation model can be used as basis for simulating the response of larger forwarder models. Simulating the entire product family would reduce the need for physical testing which in turn would speed up the design process and possibly reduce the cost machine development and the time spent on the design phase.



Figure 1.1. John Deere 1010E forwarder, 6 wheel configuration [33].

1.1 Motivation for analysis

As forestry machines are driven in rough, constantly altering forest terrains, the forces acting on them are difficult to predict without physical testing. These forces depend on stiffness properties of both the machine and the terrain, velocity of the machine, total mass of the machine and the geometry of the terrain. Comprehensive physical tests are expensive and they are unsuitable for testing new models early in the design phase. By using a simulation model that is capable of determining the forces exerted from the terrain to the machine and computing the response to these forces in desired operation

conditions, new designs and effects of geometry modifications in them can be easily studied.

The frames of forestry machines consist of welded sheet metal parts. Weld seams exposed to high stresses are prone to fatigue damage. By using finite element method and the right loading conditions, the optimum design can be found. When the machine is as light as possible while still maintaining the required stiffness and fatigue life, the mass of the cargo is maximized and the cost for manufacturing is minimized.

1.2 John Deere Forestry Oy

The manufacturing of John Deere cut-to-length forestry machines in Finland began in 1972. At that time the factory was called *Rauma-Repola Forest Machine Group*. The company had different names (*Lokomo Forest*, *FMG (Forest Machine Group)* *Lokomo Forest*, *FMG Timberjack* and *Timberjack*) before Deere & Company acquired the business in the year 2000. The company name was changed from Timberjack Oy to John Deere Forestry Oy and product labels from Timberjack to John Deere in 2005. [34]

John Deere Forestry Oy is a part of a subdivision (Construction & Forestry) of Deere & Company, which was founded in 1837 by blacksmith John Deere in Illinois, USA. The company's first product was a polished plow made from broken steel sawmill blade. At that time plowing was constantly interrupted by soil sticking to the plow which needed to be cleaned in order to continue working. John Deere's new innovation removed this problem. [21]

Today Deere & Company has approximately 60 000 employees (end of 2014) globally with net sales and revenues of \$36.1 billion. In addition to Construction & Forestry, Deere & Company has Agriculture, Turf, Power Systems and Financial divisions. The managing director of Deere & Company is currently Samuel R. Allen. [20]

1.3 Cut to length forestry equipment

Mechanized methods for tree harvesting can be divided into *cut-to-length (CTL)*, *tree-length* and *whole-tree* methods. In the whole-tree method the entire tree is felled and transported from the forest. The tree-length method is similar to the whole-tree method with the exception of delimiting the tree after felling. Cut-to-length method further refines these methods by cutting the delimiting tree into prescribed lengths right after felling. [52]

The advantages of CTL method compared to the other two are lower damage to forest floor and trees, versatility in working with all silvicultural activities (thinning, clearcutting and individual tree selection operations) and better sorting and storage of felled trees. [52]

The forwarder studied in this thesis is the machine used for transporting logs processed by CTL harvester from the forest to the roadside.

1.4 Structure of the report

The methods for solving the problem introduced in the previous sections are presented in Chapter 2, in which theory of the utilized numerical integration schemes and discretization are discussed.

Chapter 3 introduces the general arrangement and measured quantities of the physical field test, the replication of which will be attempted in the simulation.

The discretized mathematical model constructed to simulate the forwarder is described in Chapter 4. Generated grids and the material models used will be presented. The effects of idealizations made in the mathematical model compared to the real structure will also be estimated (i.e. model verification will be made).

The results obtained from the model will be presented and discussed in Chapter 5. The model will be validated by comparing the simulated results to the measured data.

Suggestions for further development of the model and further cases to simulate are presented in Chapter 6.

2. COMPUTATIONAL METHOD

As will be further discussed in Section 2.4, an analytical solution for the studied problem cannot be found. The numerical methods addressed to solve the case are considered in this chapter.

The simulation can be divided to three sections; *pre-processing*, *solving* and *post-processing*.

Pre-processing includes the initial geometry modifications, discretization (mesh generation), material settings, boundary and initial conditions. All of these are presented in Chapter 4.

General principles of solution methods are discussed in Sections 2.3-2.8.

Evaluation of calculated results and processing them in order to establish a readable and an understandable form is performed during post-processing. See Chapter 5 for results.

2.1 Software

ANSYS Workbench 16.1-17.0 and ANSYS SpaceClaim 16.1-17.0 were used for pre-processing, LS-DYNA® R7.1.1/R8.0.0 revision 88541/95309 for solving and ANSYS Workbench 16.2 / LS-DYNA® PrePost 4.3 for post-processing.

2.1.1 ANSYS®

The history of ANSYS Inc., as the company is known today, dates back to 1970 when it was founded by John A. Swanson in Pittsburgh, United States of America. Swanson worked with structural analyses in the 1960s, when some of the finite element calculations in the nuclear industry were still calculated by hand. As the computing power began to increase in the 1970s, Swanson started developing a computer program called *SASI* (*Swanson Analysis System Inc.*) for solving static and dynamic structural problems and heat transfer. [8]

The company continued to grow 10-20 % annually parallel with the growth of computing power. In 1994 SASI was sold. The new name for the company was ANSYS Inc. and the program was now called ANSYS®. Today ANSYS Inc. is one of the world's leading engineering simulation software providers and it focuses on providing a fully integrated set of tools for solving multiphysical problems. [8]

ANSYS® was chosen as pre- and post-processing tool due its versatility and ability to directly write (with limitations) input files for LS-DYNA® to solve.

2.1.2 LS-DYNA®

The development of LS-DYNA® started in 1974 at the Lawrence Livermore National Laboratory. At that time the program was called *DYNA3D*. For the next decades the code was improved and new features were constantly added. [46 p. 21]

The main solution methodology today is still explicit time integration even though implicit time integration with limited capabilities is also included in the modern versions of the program. [46 p. 19]

LS-DYNA® was chosen as the solving software due to its capabilities in structural analyses employing explicit time integration scheme.

2.2 Validation and verification

Validation and verification are separate processes that are used when evaluating the ability of the simulation model to predict the behavior of the studied subject.

Verification is defined as a means for ensuring that the computer program and its implementation are both correct [57]. Points to be considered in the verification of a finite element simulation model are [16]:

- The effect of idealizations in studied geometry. Imperfections are always incorporated in real life structures.
- Material models. Materials often exhibit very complex non-linear behavior and not all necessary data are available to create an accurate model.
- Discretization. A finite element solution should always approach the continuum solution as the mesh element size is reduced [69, p. 1], and therefore the feasible mesh size depends on the desired level of accuracy and other limitations.
- Boundary conditions. These include the effect of initial conditions and applied supports.

These verification steps are considered in Chapter 4.

The validation process ensures that the simulation model output accuracy is satisfactory for the purpose it is intended for [16, 57]. The following points should be covered for validation [16]:

- Test results. Comparison of the simulation and the test results is significant if comprehensive test data are available.

- Analytical solutions. Comparison of the simulation model or a part of it to a closed form solution.
- Comparison to similar models.

These validation steps are considered in Chapters 4 and 5.

2.3 Finite element method

The *Finite Element Method (FEM)*, in general, is a numerical method used for solving partial differential equations by discretizing the studied geometry using finite amount of different types of elements (see Section 2.7) [69 p. 2]. FEM is used for complex geometries in situations where analytical solutions cannot be found. Procedures for obtaining a solution in transient structural finite element analysis are presented in Section 2.4.

2.4 Time integration

The method used in this simulation uses explicit time integration. Some differences of implicit and explicit time integrations in a *structural mechanics solution* are discussed in the following sections. Implicit method is not used in this simulation; it is only briefly introduced to highlight the differences between the two integration methods.

The equation to be solved in transient structural mechanics is

$$[M]\ddot{\mathbf{x}} = \mathbf{F}(t), \quad (1)$$

where the load vector is denoted with $\mathbf{F}(t)$, nodal acceleration vector (second time derivative of nodal displacement \mathbf{x}) with $\ddot{\mathbf{x}}$ and mass matrix with $[M]$. The load vector includes internal, external, damping and hourglass forces, thus $\mathbf{F} = \mathbf{F}(\mathbf{f}, \dot{\mathbf{x}}, \mathbf{x}, t)$. Equation (1) represents the equilibrium equation for *d'Alembert's principle*, which states that external forces $\mathbf{f}(t)$ acting on the domain must be equal to the sum of inertial ($[M]\ddot{\mathbf{x}}$), damping ($[C]\dot{\mathbf{x}}$), and internal forces due to stiffness of the structure (see Section 2.7). Hourglass forces included in the load vector are unphysical and therefore the accumulated energy generated by these forces should be as low as possible as the solution proceeds (see Section 2.8). Due to the displacement dependency of internal force vector, Equation (1) becomes a *non-linear ordinary differential equation*, for which analytical solutions cannot be found and numerical methods must be used instead. [46 pp. 611-612]

2.4.1 Implicit method

In the implicit method the solution for Equation (1) is obtained by using either the *Newmark* (Equations (2) and (3)) or *HHT (Hilber-Hughes-Taylor)* time integration with

a series of linear approximations (*Newton-Raphson iterations*). In order for solving nodal velocity

$$\dot{\mathbf{x}}^{t+\Delta t} = \dot{\mathbf{x}}^t + \Delta t[(1 - \gamma)\ddot{\mathbf{x}}^t + \gamma\ddot{\mathbf{x}}^{t+\Delta t}] \quad (2)$$

at time step $t + \Delta t$, nodal acceleration $\ddot{\mathbf{x}}$ at $t + \Delta t$ is required. This acceleration is solved from equation of the nodal displacement

$$\mathbf{x}^{t+\Delta t} = \mathbf{x}^t + \Delta t\dot{\mathbf{x}}^t + \Delta t^2[(1/2 - \beta)\ddot{\mathbf{x}}^t + \beta\ddot{\mathbf{x}}^{t+\Delta t}] \quad (3)$$

as

$$\ddot{\mathbf{x}}^{t+\Delta t} = \frac{1}{\beta\Delta t^2}\mathbf{x}^{t+\Delta t} - \frac{1}{\beta\Delta t^2}\mathbf{x}^t - \frac{1}{\beta\Delta t}\dot{\mathbf{x}}^t - \left(\frac{1}{2\beta} - 1\right)\ddot{\mathbf{x}}^t \quad (4)$$

in which γ and β are *Newmark parameters*. Equation (4) is then substituted back to equation (1) from which displacement $\mathbf{x}^{t+\Delta t}$ is obtained. Velocity $\dot{\mathbf{x}}^{t+\Delta t}$ and acceleration $\ddot{\mathbf{x}}^{t+\Delta t}$ can now be solved from Equations (2) and (4), respectively. Since the above variables cannot be solved directly from Equations (2) and (3) in terms of known quantities (i.e. equations are coupled), the method is called *implicit*. [5, 35]

Since the solving method is implicit, convergence problems may arise on highly nonlinear problems. The equations of implicit formulation are coupled, and therefore need to be solved using global matrices. As the nonlinear dynamic effective stiffness matrix is a function of displacement, the matrix factorization has to be done in each time step^A. This is computationally expensive, but to compensate this, relatively large time steps can be used. [5]

2.4.2 Explicit method

The solution process for the explicit method can be illustrated by using a flowchart shown in Figure 2.1.

^A In case of *modified Newton Raphson method*. For *full Newton-Raphson method* factorization has to be done in each iteration.

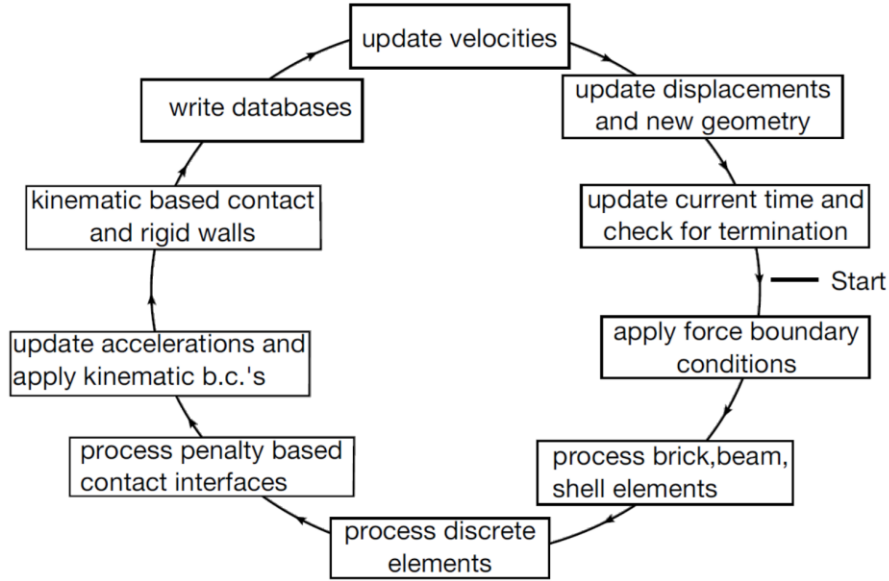


Figure 2.1. Calculation process of a single cycle (time step) in explicit analysis [46 p. 620]. The starting point for the algorithm does not necessarily have to be in the position shown by this figure; it can be changed based on type of initial conditions used [58 p. 21].

Initial conditions $\ddot{\mathbf{x}}^0$, $\dot{\mathbf{x}}^0$ and \mathbf{x}^0 are assumed to be known. Accelerations can be solved from Equation (1) as

$$\ddot{\mathbf{x}}^t = [M]^{-1} \mathbf{F}(t). \quad (5)$$

Now that accelerations at time t are known, the velocities at time $t + \Delta t/2$ can be calculated as

$$\dot{\mathbf{x}}^{t+\Delta t/2} = \dot{\mathbf{x}}^{t-\Delta t/2} + \ddot{\mathbf{x}}^t \Delta t^{t+\Delta t/2}. \quad (6)$$

And furthermore the nodal displacements \mathbf{x} at time $t + \Delta t$ can be calculated using the central difference method employed in explicit time integration as

$$\mathbf{x}^{t+\Delta t} = \mathbf{x}^t + \dot{\mathbf{x}}^{t+\Delta t/2} \Delta t^{t+\Delta t/2}. \quad (7)$$

This process is repeated until the desired time t is reached. Equations (5)-(7) can be solved directly without iteration, hence the term *explicit*.

The above equations are uncoupled (due to the use of lumped mass matrix) as opposed to the equations of implicit dynamics, and therefore the solution time for a single time step is smaller in explicit dynamics than it is in implicit^B. The inversion of a lumped (diagonal) matrix reduces to a simple division by a scalar in Equation (5), which is cheap to compute compared to the factorization of a consistent matrix [58 p. 24; 69 p.

^B Explicit method parallelizes to multiple processors better than the implicit method due to uncoupled equations.

648]. However, due to the conditional stability of the explicit method (considered in the next section), the time step to be used is usually much smaller compared to the time step used in the implicit method (see Section 2.4.3).

[5, 32, 35, 46, 58]

2.4.3 Time step controls

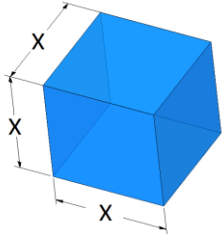
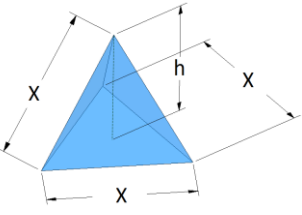
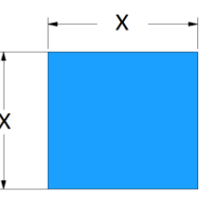
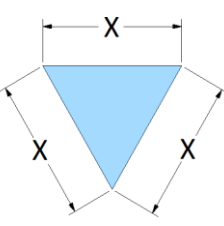
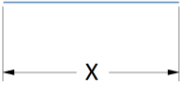
As was stated in the previous section, the equations of the explicit time integration method are uncoupled, meaning that the results for each element are calculated separately. Therefore during one time step, the information from one side of the element can only travel to the other side of the element to keep the solution stable. The physical interpretation for this is the wave propagation in the structure (or highest natural frequency of the structure). The maximum time step Δt that can be used in the analysis to ensure a stable solution is limited by *Courant-Friedrichs-Lewy (CFL)* condition as

$$\Delta t \leq f \left[\frac{h}{c} \right]_{min}, \quad (8)$$

where c is the speed of sound in the material, f is the time step safety factor used in the analysis to increase stability (defaults to 0.9) and h is the characteristic element dimension. The CFL condition restricts the wave from traveling more than the dimension h in one time step. [5, 17, 32] The element that minimizes condition (8) dictates the time step to be used. Characteristic dimensions for different element types are calculated using equations shown in Table 2.1.

Speed of sound also depends on stress state and damping properties of the material, but crude evaluation of the time step can be made even by neglecting their effect.

Table 2.1. Calculation of characteristic dimensions for low order elements with equal edge lengths [5; 46 pp. 599-601].

Element type	Geometry	Characteristic dimension h
Hexahedral solid		The volume of the element divided by the area of the largest face.
		$h = x$
Tetrahedral solid		Minimum distance from node to opposing surface.
		$h = \sqrt{\frac{2}{3}}x$
Quad shell		Square root of the area of the element.
		$h = x$
Tri shell		Two times the area of the element divided by the length of the longest side.
		$h = \frac{\sqrt{3}}{2}x$
Beam		Length of the element
		$h = x$

Hexahedral/quad mesh is preferred over tetrahedral/triangular mesh to prevent the time step from getting too small while retaining solution accuracy. Smallest geometry details are de-featured and simplified to achieve reasonable computation times.

If the mesh contains only few small elements, automatic mass scaling can be used to prevent the time step from becoming too small. The speed of sound (elastic speed wave) in material is calculated as ^c (for beam element) [46 p. 600]

^c Speed of sound also depends on stress state and damping properties of the material, but crude evaluation of the time step (and hence the element size) can be made even by neglecting their effect.

$$c = \sqrt{\frac{E}{\rho}} = \sqrt{\frac{EV}{m}}. \quad (9)$$

By substituting (9) to (8), Δt results as

$$\Delta t \leq f * \left[\sqrt{\frac{m}{EV}} h \right]_{min}. \quad (10)$$

As can be seen, the minimum time step is directly proportional to the square root of the mass of the element. By scaling the mass of a single element the error in the total mass of the structure is small but the benefits from a greater time step might be significant. Mass scaling is used in this analysis. Increased mass due to scaling is reported in Section 5.4.3.

2.5 Contact algorithms

In many dynamic simulation cases studying the interactions between impacting or sliding bodies is important [46 p. 633]. Contact algorithms are developed in order to address these problems.

Penalty based contact methods are commonly used in FEM. They all are based on the idea of adding a spring between the slave node (red nodes in Figure 2.2) and the master surface (blue surface in Figure 2.2). Stiffness k_n of this spring is denoted as contact stiffness and displacement x_p as penetration caused by contact force

$$F_n = k_n x_p. \quad (11)$$

In addition to normal stiffness, contacts with friction also exhibit tangential stiffness and tangential forces. [4] Tangential frictional forces F_f are calculated based on friction coefficient μ and normal force F_n as

$$F_f = \mu F_n. \quad (12)$$

The friction coefficient is a function of relative speed between the contact surfaces as

$$\mu = \mu_d + (\mu_s - \mu_d) e^{-d|\mathbf{u}_f|}, \quad (13)$$

where μ_s and μ_d are the static and dynamic coefficients of friction, respectively, d is a decay constant defining the rate of transformation from static to dynamic friction coefficient and \mathbf{u}_f is the relative velocity between contacting surfaces. [46 p. 652] As it can be seen from Equation (13), $\mu = \mu_s$ when there is no sliding ($\mathbf{u}_f = 0$) between surfaces and $\lim_{\mathbf{u}_f \rightarrow \infty} \mu = \mu_d$.

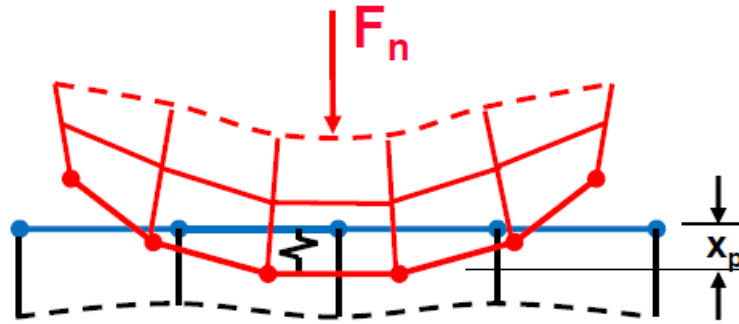


Figure 2.2. Principle of penalty based contact formulation [4].

Suitable value for contact stiffness depends on the allowed penetration which in turn depends on the required accuracy of contact pressure. Increasing contact stiffness to infinity would result as zero penetration but this would result as numerical problems. Too low contact stiffness results in excessive penetration and too high stiffness in oscillatory contact behavior (latter is likely to cause divergence in implicit analyses). [4; 58 pp. 289-304]

Penalty stiffness affects the contact time step. Stiffness is automatically calculated based on nodal masses at contact and global time step [44 p. 591].

2.6 Dynamic relaxation

Tires (and other flexible parts) deform due to gravitational loads and other applied loads (such as tire pressure). If all of these effects are stepped on at the beginning of transient simulation, they will result as oscillatory behavior. To allow for the oscillatory behavior to diminish, the simulation must be run for several times longer than the duration of lowest natural frequency of the oscillation. This damping phase would be computationally very expensive due to its long duration compared to the time required to capture the dynamic behavior of interest.

Dynamic relaxation is a method of obtaining a solution for the quasi-static phase of the simulation. The quasi-static phase includes the effects of gravity and tire pressurization. During this phase, system damping is kept artificially high until kinetic energy drops to zero (or below a predefined tolerance). In other words, transient oscillations diminish and the solution approaches static equilibrium. [2; 46 p. 719] The effect of low, or realistic, and high damping (used in the relaxation phase) for tire vertical displacement under stepped compression load is shown in Chart 2.1. After reaching static equilibrium with high damping, system damping is decreased to a realistic level and the transient phase of the simulation is started.

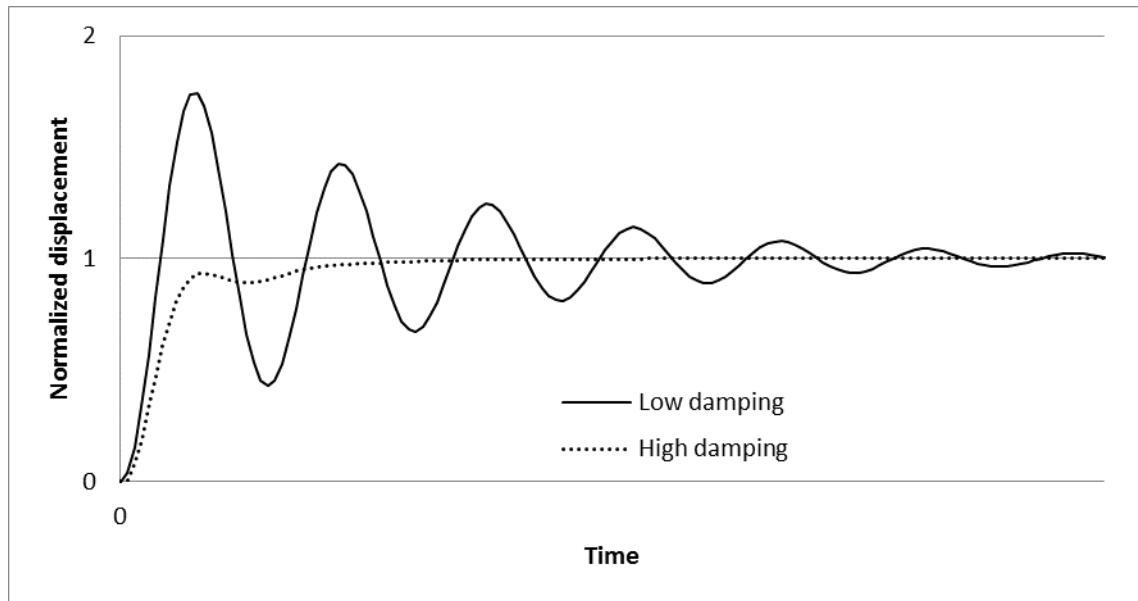


Chart 2.1. Using a high damping value the static equilibrium is found significantly faster compared to a low damping value.

2.7 Elements

Displacements \mathbf{u} within the *volume* (or *area* for 2D elements and *length* for 1D elements) of the element are interpolated from nodal degrees of freedom \mathbf{x} as

$$\mathbf{u} = [\mathbf{N}]\mathbf{x}. \quad (14)$$

The *shape function matrix* (or *interpolation function matrix*) $[\mathbf{N}]$ is defined separately for each element type (see Sections 2.7.1 and 2.7.2). It links the nodal values to spatial values within the element.

Strain is the rate of deformation in space, i.e. it is a spatial derivative of displacement as

$$\varepsilon_{ii} = \frac{\partial u_i}{\partial x_i} \quad (15)$$

and

$$\gamma_{ij} = \frac{\partial u_i}{\partial x_j} + \frac{\partial u_j}{\partial x_i}. \quad (16)$$

The *strain-displacement matrix* $[\mathbf{B}]$, that is a spatial derivative of the shape function matrix $[\mathbf{N}]$, is used for calculating strains based on the nodal displacements as

$$\boldsymbol{\varepsilon} = [\mathbf{B}]\mathbf{x}. \quad (17)$$

The strain-displacement matrix is also element-type dependent and a corresponding matrix for each element type is presented in the following sections.

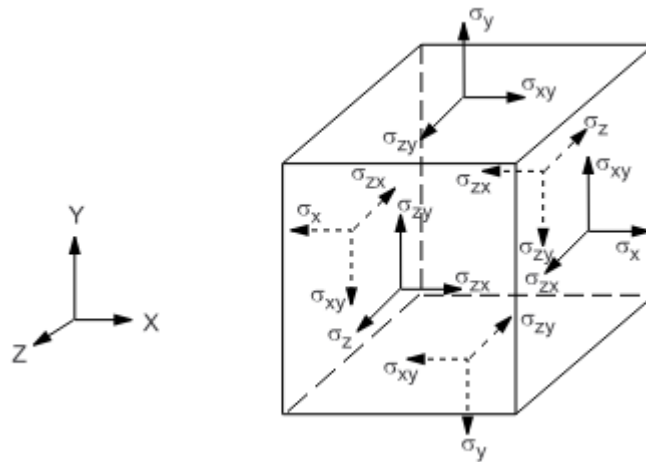


Figure 2.3. Stress components in 3D case [3].

Furthermore the stresses (components shown in Figure 2.3) within the element are calculated from strains by using an *elasticity matrix* (or *material stiffness matrix*) $[D]$ as

$$\boldsymbol{\sigma} = [D](\boldsymbol{\varepsilon} - \boldsymbol{\varepsilon}_0) + \boldsymbol{\sigma}_0, \quad (18)$$

where $\boldsymbol{\varepsilon}_0$ and $\boldsymbol{\sigma}_0$ are the possible initial strains and stresses (caused by shrinkage, temperature change etc.). The compiling of matrix $[D]$ depends on the implemented material model and element type. The simplest case is an isotropic linear elastic material that obeys *Hooke's law* for which (in 3D case) [49 pp. 15-16]

$$[D] = \begin{bmatrix} \lambda + 2\mu & \lambda & \lambda & 0 & 0 & 0 \\ \lambda & \lambda + 2\mu & \lambda & 0 & 0 & 0 \\ \lambda & \lambda & \lambda + 2\mu & 0 & 0 & 0 \\ 0 & 0 & 0 & \mu & 0 & 0 \\ 0 & 0 & 0 & 0 & \mu & 0 \\ 0 & 0 & 0 & 0 & 0 & \mu \end{bmatrix}, \quad (19)$$

where λ and μ are the *Lamé constants*, which are expressed via elasticity modulus E and Poisson's ratio ν as

$$\lambda = \frac{\nu E}{(1 + \nu)(1 - 2\nu)} \quad (20)$$

and

$$\mu = \frac{E}{2(1 + \nu)}. \quad (21)$$

Finally, the nodal force vector \mathbf{F} is calculated using external, body, internal, contact, hourglass and damping forces ($\mathbf{f}, \mathbf{b}, \mathbf{F}_{cont}, \mathbf{F}_{hg}, \mathbf{F}_{damp}$, respectively) as given by

$$\mathbf{F} = \mathbf{f} - \mathbf{b} - \mathbf{F}_{int} - \mathbf{F}_{cont} - \mathbf{F}_{hg} - \mathbf{F}_{damp}. \quad (22)$$

The internal force vector is, as is elasticity matrix, reliant on the material model and element type being used. Internal force vector represents the correlation between nodal forces and displacements.

Equations (14)-(22) represent the calculation of all necessary results within the element (i.e. in *local coordinates* ξ, η, ζ). To transform results to *global coordinates* (x, y, z), the chain rule of partial differentiation is utilized as

$$\frac{\partial}{\partial \xi} = \frac{\partial}{\partial x} \frac{\partial x}{\partial \xi} + \frac{\partial}{\partial y} \frac{\partial y}{\partial \xi} + \frac{\partial}{\partial z} \frac{\partial z}{\partial \xi}, \quad (23)$$

$$\frac{\partial}{\partial \eta} = \frac{\partial}{\partial x} \frac{\partial x}{\partial \eta} + \frac{\partial}{\partial y} \frac{\partial y}{\partial \eta} + \frac{\partial}{\partial z} \frac{\partial z}{\partial \eta} \quad (24)$$

and

$$\frac{\partial}{\partial \zeta} = \frac{\partial}{\partial x} \frac{\partial x}{\partial \zeta} + \frac{\partial}{\partial y} \frac{\partial y}{\partial \zeta} + \frac{\partial}{\partial z} \frac{\partial z}{\partial \zeta}. \quad (25)$$

Equations (23)-(25) can be rewritten in matrix form as

$$\begin{bmatrix} \frac{\partial}{\partial \xi} \\ \frac{\partial}{\partial \eta} \\ \frac{\partial}{\partial \zeta} \end{bmatrix} = \begin{bmatrix} \frac{\partial x}{\partial \xi} & \frac{\partial y}{\partial \xi} & \frac{\partial z}{\partial \xi} \\ \frac{\partial x}{\partial \eta} & \frac{\partial y}{\partial \eta} & \frac{\partial z}{\partial \eta} \\ \frac{\partial x}{\partial \zeta} & \frac{\partial y}{\partial \zeta} & \frac{\partial z}{\partial \zeta} \end{bmatrix} \begin{bmatrix} \frac{\partial}{\partial x} \\ \frac{\partial}{\partial y} \\ \frac{\partial}{\partial z} \end{bmatrix} = [J] \begin{bmatrix} \frac{\partial}{\partial x} \\ \frac{\partial}{\partial y} \\ \frac{\partial}{\partial z} \end{bmatrix}, \quad (26)$$

where the matrix $[J]$ is called the *Jacobian matrix*. By inverting it, transforming the desired terms from local to global coordinates can be calculated

$$\begin{bmatrix} \frac{\partial}{\partial x} \\ \frac{\partial}{\partial y} \\ \frac{\partial}{\partial z} \end{bmatrix} = [J]^{-1} \begin{bmatrix} \frac{\partial}{\partial \xi} \\ \frac{\partial}{\partial \eta} \\ \frac{\partial}{\partial \zeta} \end{bmatrix}. \quad (27)$$

The most important features and formulation of elemental matrices for element types used in the analysis are presented in the following sections.

[46 pp. 45-53; 69 pp. 18-24]

2.7.1 Solid

Solid elements are used in this simulation only for logs (see Section 4.6). The logs are meshed with pure hexahedral structured grid. The element used in meshing is shown in Figure 2.4.

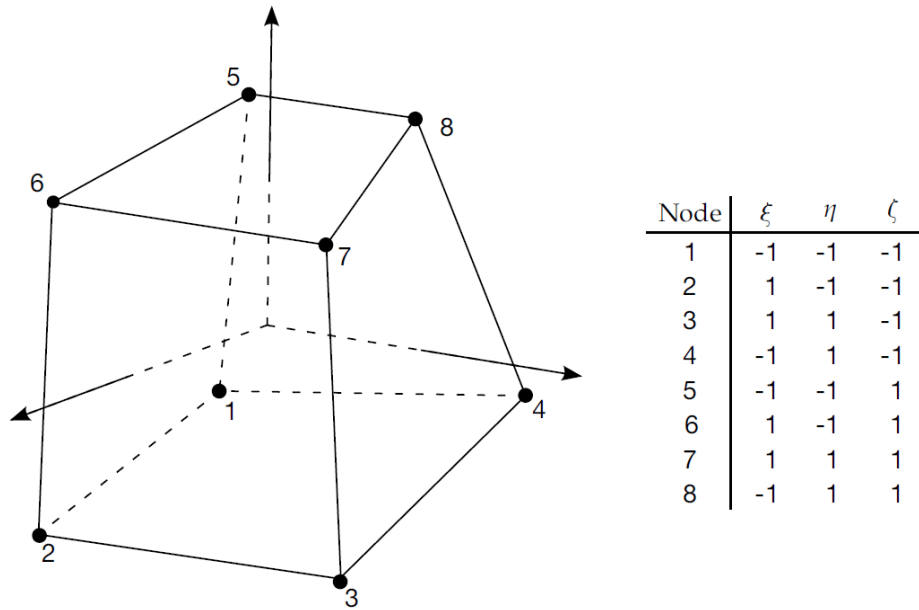


Figure 2.4. Local coordinate parameters (ξ , η and ζ) and geometry of eight node solid hexahedral DYNA3D element [46 p. 52]. Each node has three translational degrees of freedom (DOFs) which results as a total of 24 DOFs for a single element.

Tri-linear shape functions for the element are in the form

$$N_j = \frac{1}{8}(1 + \xi\xi_j)(1 + \eta\eta_j)(1 + \zeta\zeta_j), \quad (28)$$

where j is the corresponding node number (1...8) and ξ_j, η_j, ζ_j take on the value at node j as listed in Figure 2.4. The shape function matrix is assembled from the shape functions of each node as

$$[N] = \begin{bmatrix} N_1 & 0 & 0 & N_2 & 0 & \dots & 0 & 0 \\ 0 & N_1 & 0 & 0 & N_2 & \dots & N_8 & 0 \\ 0 & 0 & N_1 & 0 & 0 & \dots & 0 & N_8 \end{bmatrix}. \quad (29)$$

As was stated in page 13, $[B]$ is a spatial derivative of the shape function matrix

$$[B] = \begin{bmatrix} \frac{\partial}{\partial x} & 0 & 0 \\ 0 & \frac{\partial}{\partial y} & 0 \\ 0 & 0 & \frac{\partial}{\partial z} \\ \frac{\partial}{\partial y} & \frac{\partial}{\partial x} & 0 \\ 0 & \frac{\partial}{\partial z} & \frac{\partial}{\partial y} \\ \frac{\partial}{\partial z} & 0 & \frac{\partial}{\partial x} \end{bmatrix} [N]. \quad (30)$$

Stiffness matrix $[K]^e$ for the isoparametric element in a non-linear case is integrated over the volume V of the element as (Updated Lagrangian Formulation)

$$\begin{aligned} [K]^e &= \int_V ([B]^T [D] [B] + [G]^T [S] [G]) dV \\ &= \iiint_V ([B]^T [D] [B] + [G]^T [S] [G]) dx dy dz \\ &= \iiint_V ([B]^T [D] [B] + [G]^T [S] [G]) |J| d\xi d\eta d\zeta, \end{aligned} \quad (31)$$

where $[S]$ is the 2^{nd} Piola-Kirchhoff Stress Tensor and $[G]$ the Non-Linear Strain-Displacement Transformation Matrix^D. The integral is transformed from local to global coordinates by using the determinant of the Jacobian matrix $|J|$ in conjunction with local coordinates. As the integral cannot be solved in a closed form, numerical integration must be used instead. By using numerical integration (*Gaussian quadrature rule*) the integral (31) can be expressed as

$$[K]^e = \sum_{i=1}^n \sum_{j=1}^n \sum_{k=1}^n ([B]^T [D] [B] + [G]^T [S] [G]) |J(\xi_i, \eta_j, \zeta_k)| w_i w_j w_k, \quad (32)$$

where weight factors $w_i = w_j = w_k = 2$ and number of integration points $n = 1$ for one-point (reduced integration) Gaussian quadrature used by this element [46 pp. 45-53]. The determinant of the Jacobian matrix $|J(\xi_i, \eta_j, \zeta_k)|$ is calculated at the integration point located in the middle of the element (at $\xi = \eta = \zeta = 0$). Therefore Equation (32) simplifies to

$$[K]^e = 8([B]^T [D] [B] + [G]^T [S] [G]) |J(0,0,0)|, \quad (33)$$

^D See [12; 18 pp. 139-151] for more information on these two matrices and the derivation of the stiffness matrix.

where $8|J(0,0,0)|$ approximates the volume of the element. The mass and damping matrices are constructed in a similar fashion as the stiffness matrix as

$$[M]^e = 8[N]^T \rho [N] |J(0,0,0)| \quad (34)$$

and

$$[C]^e = 8[N]^T \varphi [N] |J(0,0,0)|, \quad (35)$$

where ρ and φ are the elemental density and damping, respectively.

When compared to elements having higher order shape functions and integration, the advantages of DYNA3D are significant reductions in necessary mathematical operations and the absence of the volumetric locking phenomenon^E. On the other hand, elements with quadrilateral geometry and one point integration suffer from hourglass modes which are discussed in Section 2.8. This phenomenon is not found in higher order hexahedral elements or in tetrahedral elements regardless of the number of integration points.

[12; 18 pp. 139-151; 46 pp. 45-53; 49 pp. 28-31; 55; 69 pp. 18-24]

2.7.2 Shell

Shell elements are suitable for modeling structures that have one dimension (thickness t) small compared to the other two (L), i.e. $t/L \ll 1$. Shells (plates) are classified as very thin if $L/t > 100$, moderately thin if $20 < L/t < 100$, thick if $3 < L/t < 20$ and very thick if $L/t < 3$. Shell elements based on the classical *Kirchhoff-Love* plate theory, which can be thought to be a two dimensional extension of the *Euler-Bernoulli* beam theory, are applicable for the thin and moderately thin regions whereas the enhanced *Mindlin-Reissner* theory (extension of *Timoshenko* beam theory) expands the applicability range to thick shells. Very thick shells should be modeled using solid elements [15, 62, 68]. Solid elements are not suitable for modeling thin structures, especially in explicit analyses, due to the fact that using one linear solid element in the thickness direction leads to erroneous bending behavior^F whereas using multiple solids through the thickness leads to small time step through the CFL condition and increased number of DOFs in the model [46].

^E Found in higher order integration elements with incompressible material.

^F Erroneous stiffness

- Excessive stiffness in case full integration
 - shear locking; linear shape functions cannot reproduce the required parabolic shear distribution through the thickness
 - volumetric locking; even higher order elements with full integration lock if Poisson's ratio approaches 0.5
- Too low stiffness in case of reduced integration
 - zero energy hourglass modes.

The derivation of general equations for shell theory starts by recognizing the displacements from Figure 2.5 in x -direction as [62 p. 12]

$$u(x, y, z) = u_m(x, y) + z \frac{\partial w_m}{\partial x}(x, y) = u_m(x, y) + z \phi_y(x, y), \quad (36)$$

where subscript m denotes the deformations at mid-surface ($z = 0$) of the plate. Similarly in y -direction as (See [37 pp. 205-207] for details for the different sign of mid-plane rotation)

$$v(x, y, z) = v_m(x, y) - z \phi_x(x, y) \quad (37)$$

and in z -direction as

$$w(x, y, z) = w_m(x, y). \quad (38)$$

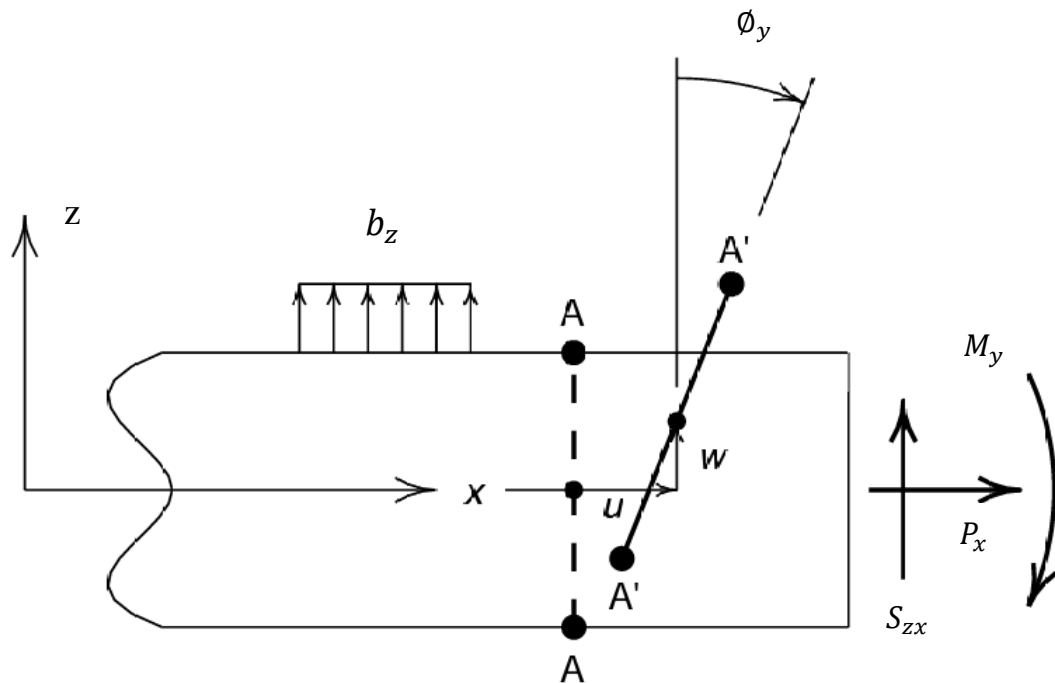


Figure 2.5. Displacements and force resultants in a shell with supports and loads independent of y -coordinate, adapted from [68 p. 326].

Next, the in-plane membrane force P_x , shear force S_{zx} and bending moment M_y resultants are obtained by integrating the stresses of 3D element faces (see Figure 2.3) in the thickness direction (the membrane is located at the mid-plane of the body, at $t = 0$, hence the integration limits in the following equations). The stresses to be integrated are acquired by substituting for displacements in strain Equations (15) and (16) using Equations (36) and (38) and by employing a constitutive relation of elastic and isotropic material. Thus the resultants (for XZ-plane in Figure 2.5) are for membrane forces [62 p. 13; 66 p. 34]

$$P_x = \int_{-t/2}^{t/2} \sigma_x dz = \frac{Et}{1-\nu^2} \left(\frac{\partial u_m}{\partial x} + \nu \frac{\partial v_m}{\partial y} \right), \quad (39)$$

for shear force

$$S_{zx} = \int_{-t/2}^{t/2} \tau_{zx} dz = \kappa \frac{Et}{2(1+\nu)} \left(\frac{\partial w_m}{\partial x} + \phi_y \right), \quad (40)$$

for bending moment

$$M_y = \int_{-t/2}^{t/2} \sigma_x z dz = \frac{Et^3}{12(1-\nu^2)} \left(\frac{\partial \phi_y}{\partial x} + \nu \frac{\partial \phi_x}{\partial y} \right) \quad (41)$$

and for twisting moment

$$M_{xy} = \int_{-t/2}^{t/2} \tau_{xy} z dz = \frac{Et^3}{24(1+\nu)} \left(\frac{\partial \phi_y}{\partial y} - \frac{\partial \phi_x}{\partial x} \right). \quad (42)$$

For rectangular and homogeneous section the correction factor $\kappa = 5/6$ ^G. [62 pp. 14-15]

Finally the equilibrium equations for a differential element are for forces in x -direction

$$\frac{\partial P_x}{\partial x} + \frac{\partial S_{yx}}{\partial y} + b_x = 0, \quad (43)$$

in z -direction

$$\frac{\partial S_{zx}}{\partial x} + \frac{\partial S_{zy}}{\partial y} + b_z = 0 \quad (44)$$

and for moments

$$\frac{\partial M_y}{\partial x} + \frac{\partial M_{yx}}{\partial y} - S_{zx} + m_x = 0, \quad (45)$$

where m_x is the inertial force. All of the equations above are expanded to y -direction in a similar fashion to obtain equations for a general 3D case.

[68 pp. 325-327]

^G κ is added for the theory to correctly predict the amount of internal energy [62 p. 14].

Kirchhoff-Love theory poses the following restrictions and assumptions [31 p. 87; 56 pp. 125-136; 62 pp. 14-15]:

1. Plate mid-surface is planar prior to loading
2. Stresses in z-direction are insignificant compared to stresses in x- and y-directions
3. Shear distortion is equal to zero
 - a. This property limits the applicability range to thin plates; displacements resulting from shear distortion become increasingly dominant when compared to deformations resulting from bending as L/t decreases [15, p. 15].

Further restrictions for the used shell elements are:

4. Displacements are small
 - a. Displacement in z-direction equaling to half of the plate thickness is the upper limit for “small”
 - b. Errors in displacements larger than this limit become significant
5. Normal displacement w is constant through the thickness
 - a. i.e. no compression or tension in thickness direction is considered
6. Displacements u and v vary linearly through the thickness
 - a. i.e. normals remain straight
7. Membrane and bending effects are uncoupled.

Shell elements based on Mindlin-Reissner theory remove restriction number 3 from the above list and are therefore applicable for thicker plates. Higher order theories that remove restrictions 5 and 6 also exist but they will not be covered here. [62]

Shell elements are not suitable for large rotations in *implicit static analyses* due to the fact that they do not possess any stiffness at in-plane (*drilling*) rotational degree of freedom ϕ_z as can be seen from Equations (39)-(42). By expanding these equations to y -direction, a total of three translational and two rotational degrees of freedom (u, v, w, ϕ_x, ϕ_y) can be connected to the bending, twisting, shear and membrane modes for each node. However, when transforming to global coordinates, there are three translational and three rotational DOFs ($u, v, w, \phi_x, \phi_y, \phi_z$). This results as singular global stiffness matrix if all shell elements in the mesh are coplanar (flat topology). Singular matrices cannot be inverted and therefore an implicit solution cannot be found in case there are large rotations in shell elements *and* the solution is static. This problem is usually addressed by adding a torsional spring to obtain *drill stiffness* larger than zero. However the additive stiffness is artificial and therefore causes unrealistic strains if rotations are large. In transient solution the singularity of the stiffness matrix is not as problematic; the inclusion of mass matrix leads to non-singular matrix to be inverted and

thus no need for torsional springs exists. Some issues regarding accuracy and robustness might still arise from this phenomenon even in transient analyses. [25]

All of the shell elements used in this simulation are based on the *Belytschko-Lin-Tsay* formulation (with the exception of tires, see Section 4.9) which is the default choice for LS-DYNA® (element type 2). The element is based on the Mindlin-Reissner plate theory. The Belytschko-Lin-Tsay shell is based on the combined formulation of a corotational (CR) coordinate system and a velocity-strain formulation. By using the combined representation some numerical and efficiency issues can be avoided [68 p. 480]. CR coordinate system rotates with the element and can be therefore be used in separating rigid body motion from deformation which in turn improves accuracy of stress calculation because shell element restriction number 4, small displacements (see page 21), does not restrict the magnitude of rigid body rotations [46 pp. 144-145]. The construction of the CR coordinate system shown in Figure 2.6 starts by calculating a unit vector normal to the main diagonal of the element as

$$\hat{\mathbf{e}}_3 = \frac{\mathbf{s}_3}{\|\mathbf{s}_3\|}, \quad (46)$$

where \mathbf{s}_3 is the vector cross product of vectors \mathbf{r}_{31} and \mathbf{r}_{42} which in turn are defined by the locations of nodes and $\|\mathbf{s}_3\|$ is the length of vector \mathbf{s}_3 . The superscript $\hat{\cdot}$ is used to denote local (element) coordinate system. The two remaining unit vectors in defining the coordinate system are expressed as

$$\hat{\mathbf{e}}_1 = \frac{\mathbf{r}_{21} - (\mathbf{r}_{31} \cdot \hat{\mathbf{e}}_3)\hat{\mathbf{e}}_3}{\|\mathbf{s}_1\|} = \frac{\mathbf{s}_1}{\|\mathbf{s}_1\|} \quad (47)$$

and

$$\hat{\mathbf{e}}_2 = \hat{\mathbf{e}}_3 \times \hat{\mathbf{e}}_1. \quad (48)$$

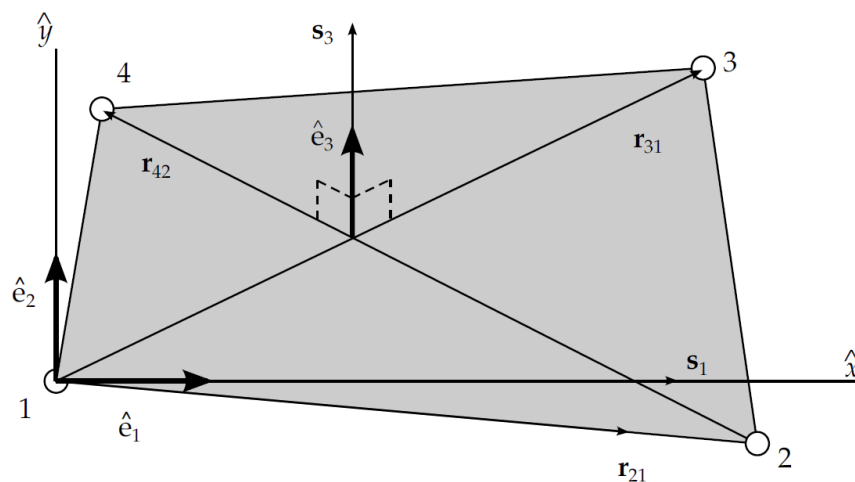


Figure 2.6. Construction of the embedded element coordinate system [46 p. 144].

The transformation from the local CR to global coordinates is defined by transformation matrix $[T]$ as

$$\mathbf{A} = [\mathbf{e}_1 \quad \mathbf{e}_2 \quad \mathbf{e}_3] \hat{\mathbf{A}} = [T] \hat{\mathbf{A}}, \quad (49)$$

where $\mathbf{e}_1, \mathbf{e}_2, \mathbf{e}_3$ are the CR coordinate system unit vectors expressed in *global coordinates* and $\mathbf{A}, \hat{\mathbf{A}}$ are vectors defined in global and local CR coordinates, respectively.

The velocity-strain relation formulations of the element are similar to the general plate theory Equations (36)-(41) with the exception of using first time derivatives of displacements, strains and stresses. These relations are evaluated at the quadrature points within the element (at the center of the element, $\xi = \eta = 0$, for the Belytschko-Lin-Tsay element with one point Gaussian quadrature). Velocity $\dot{\mathbf{x}}$, angular velocity $\dot{\boldsymbol{\phi}}$ and coordinates \mathbf{x} are needed for the aforementioned relations and they are evaluated at the mid-surface ($z = 0$, superscript m) using the isoparametric representation as

$$\dot{\mathbf{x}}^m = N_I \dot{\mathbf{x}}_I, \quad (50)$$

$$\dot{\boldsymbol{\phi}}^m = N_I \dot{\boldsymbol{\phi}}_I \quad (51)$$

and

$$\mathbf{x}^m = N_I \mathbf{x}_I, \quad (52)$$

where subscript I is summed over all nodes (1...4). The bi-linear shape functions N for the isoparametric formulations of the element are

$$N_j = \frac{1}{4} (1 + \xi \xi_j) (1 + \eta \eta_j), \quad (53)$$

where j is the corresponding node number (1...4) and ξ_j, η_j take on the value at node j as listed in Figure 2.7.

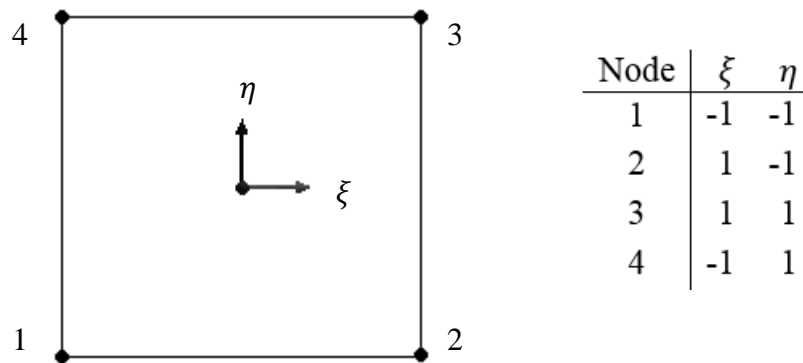


Figure 2.7. Local coordinate system node numbering for 4-noded shell element.

The isoparametric representations of the velocity-strains at the center of the element are obtained by substituting the above equations (calculated at mid-surface) to the velocity-strain relations as [46 pp. 146-147]

$$\hat{\boldsymbol{\varepsilon}} = \begin{bmatrix} \hat{\varepsilon}_x \\ \hat{\varepsilon}_y \\ \hat{\gamma}_{xy} \\ \hat{\gamma}_{xz} \\ \hat{\gamma}_{yz} \end{bmatrix} = \begin{bmatrix} \hat{x}_{xl} + \hat{z}\hat{\phi}_{yl} & 0 & 0 \\ 0 & \hat{x}_{yl} - \hat{z}\hat{\phi}_{xl} & 0 \\ \hat{x}_{yl} - \hat{z}\hat{\phi}_{xl} & \hat{x}_{xl} + \hat{z}\hat{\phi}_{yl} & 0 \\ \frac{\hat{x}_{zl}}{2} & 0 & \frac{\hat{\phi}_{yl}}{2} \\ 0 & \frac{\hat{x}_{zl}}{2} & -\frac{\hat{\phi}_{xl}}{2} \end{bmatrix} \begin{bmatrix} \frac{\partial N_I}{\partial \hat{x}} \\ \frac{\partial N_I}{\partial \hat{y}} \\ N_I \end{bmatrix}. \quad (54)$$

Finally, after stresses are obtained from strains using a suitable constitutive law, the nodal “forces” are calculated based on resultants (39)- (42) as [46 p. 147]

$$\hat{\mathbf{f}} = \begin{bmatrix} \hat{f}_{xl} \\ \hat{f}_{yl} \\ \hat{f}_{zl} \\ \hat{m}_{xl} \\ \hat{m}_{yl} \\ \hat{m}_{zl} \end{bmatrix} = A \begin{bmatrix} P_x & S_{yx} & 0 \\ S_{xy} & P_y & 0 \\ \kappa S_{zx} & \kappa S_{zy} & 0 \\ M_{xy} & M_y & -S_{zy} \\ -M_x & -M_{xy} & S_{zx} \\ 0 & 0 & 0 \end{bmatrix} \begin{bmatrix} \frac{\partial N_I}{\partial \hat{x}} \\ \frac{\partial N_I}{\partial \hat{y}} \\ \frac{\kappa}{4} \end{bmatrix}, \quad (55)$$

where A is the area of the element. As it can be noted from the above “force” vector, \hat{m}_{zl} corresponding to the ϕ_z DOF is equal to zero as there is no drill stiffness in the element.

In conclusion, the downsides of the Belytschko-Lin-Tsay shell are hourglass modes due to under-integration, invalid results in patch test and collapsing stiffness under warping. The positive aspect favoring the use of this element type in shell-like structures of explicit analysis is the extreme computational efficiency due to the combined CR and isoparametric formulations and under-integration.

[1; 13; 25; 46 pp. 143-153; 58 pp. 24, 60-70; 68 pp. 431-446, 480-491]

2.8 Energy conservation

The realization of the conservation laws is observed in explicit solution (Section 2.4.2) as opposed to the residuals monitored in an implicit solve (Section 2.4.1). The conservation of mass [5; 67 pp. 34-39]

$$\rho V = \rho_0 V_0 \quad (56)$$

is automatically enforced in an analysis using Lagrangian mesh and therefore it is not necessary to track it in the post-processing phase. Rate of strain energy

$$\dot{E}_{int} = \frac{1}{\rho} \left(\sigma_{ii} \dot{\gamma}_{ii} + \sigma_{jj} \dot{\gamma}_{jj} + \sigma_{kk} \dot{\gamma}_{kk} + 2(\sigma_{ij} \dot{\epsilon}_{ij} + \sigma_{jk} \dot{\epsilon}_{jk} + \sigma_{ik} \dot{\epsilon}_{ik}) \right) \quad (57)$$

is calculated for each element based on the input values of the previous time step. The total energy of the system consists of strain (integrated results of Equation (57)), kinetic, hourglass and dissipated energies, which must be equal to work introduced to the domain (and initial configuration energies) as

$$E_{int} + E_{kin} + E_{cont} + E_{damp} + E_{hg} = E_{kin}^0 + E_{int}^0 + E_w. \quad (58)$$

This must hold true for every time step for the solution to be accurate. [23] In addition to tracking the solution accuracy, conservation laws are used for modeling materials that use *Equations of State (EOS)*, such as *ideal gas law*. In general, EOS links material quantities that cannot be calculated using constitutive laws introduced earlier in Sections 2.7.1-2.7.2. [5, 46]

The hourglass mode is a non-physical zero-energy mode caused by reduced integration of the element as shown in Figure 2.8. As low order elements are used, hourglass modes are possible in the model (tetrahedral elements do not experience hourglass modes). The forces generated to restrict this mode can be seen as an error in the energy conservation of the model. The results are considered acceptable if the hourglass energy is lower than 5 % of the internal energy of the model (acceptable value is 10 % based on the ANSYS® manual [2] and 5 % based on the ABAQUS manual [19]).

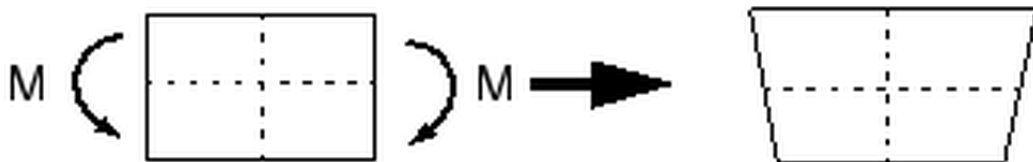


Figure 2.8. *The hourglass effect of a reduced integration element subjected to pure bending [19]. The length of both dotted lines (lines drawn from integration point) remain unchanged, thus resulting as zero stresses.*

To control the hourglass modes, *Flanagan-Belytschko viscous hourglass control* (LS-DYNA® type 2) is used with a coefficient of 0.05 (tires use different formulation, see page 53 on Section 4.9.5). Hourglass control operates as an energy dissipation mechanism, similar to damping, and therefore most of the parts do not require the use of separate damping models.

3. FIELD TEST

In addition to the test track, the field test was performed in real working conditions in a forest. Forest conditions are hard to reproduce in the simulation model (or in consecutive physical tests), however, and therefore the test track presented in Section 3.2 is simulated instead.

The experiments took place in June 2015. Ambient temperature was recorded to be +15...+20 °C. Therefore the material properties at room temperature can be used (see Chapter 4).

3.1 Test machine

John Deere 1010E forwarder is used as the test machine. The rear frame and components attached to it are the regions of interest in this test.

1010E places in the mid-range of John Deere forwarder family in terms of physical size and load bearing capacity [33].

3.2 Test track

The test track is located at the John Deere Forestry Tampere facility. The simulated part of the test track consists of semicircular bumps that are arranged as shown in Figures 3.1-3.3. Bumps are constructed of steel plates with a thickness of 12 mm.



Figure 3.1. Bump track general view. Driving direction shown by red arrow. Bumps are numbered to be referenced later in the results.



Figure 3.2. Detailed view of the bump.

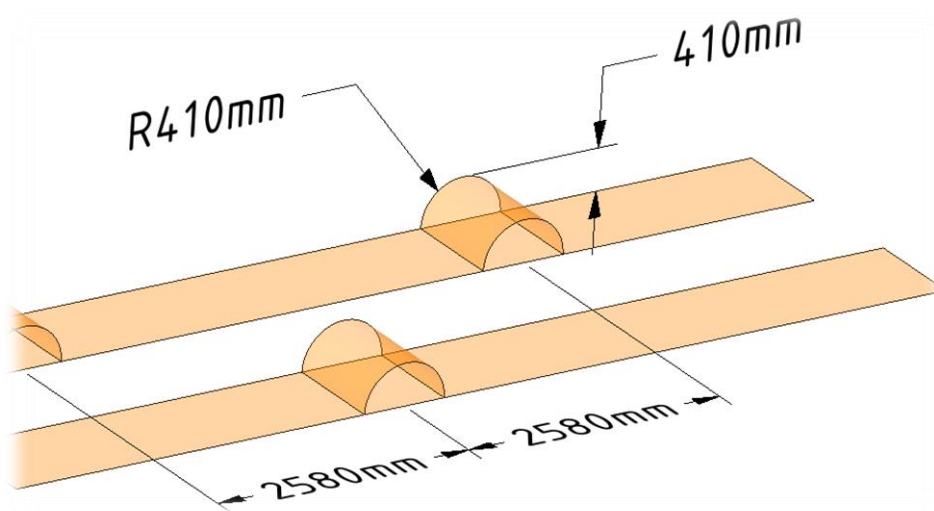


Figure 3.3. Bump track dimensions.

3.3 Test loads

The test track is driven with different amounts of logs in the load space. As a reference case, the track is driven with an empty load space. Other studied loads were 6, 9 and 12 tons.

3.4 Measured quantities

The machine rear frame is fitted with several strain gauges and force transducers. The most interesting quantities to be compared to the simulation results are the forces measured from the rear frame wheel hubs since the forces straining the frame are transmitted through the tires. The sample rate for all measured quantities is 204.8 Hz.

Strain gauge measurements cannot be directly compared to the simulation model results since the rear frame is modeled using shell elements with a relatively coarse mesh size (see Section 4.8). The model is therefore incapable of capturing local, non-linear, stress peaks (i.e. locations in which the strain gauges are fitted). However, there is a work-around for this and it is discussed in Section 6.3.

3.5 Test results

The machine is fitted with customized wheel hubs that include force transducers. The radial force reactions measured in each rear frame tire during the drive around the test track with a 12 ton load are shown in Chart 3.1. The machine crosses the studied portion of the test during the first 35 seconds (Chart 3.2 shows the same results as Chart 3.1, but

with horizontal axis limited). Another bump track with a different bump arrangement is crossed at a time period ranging from approximately 45 to 75 seconds.

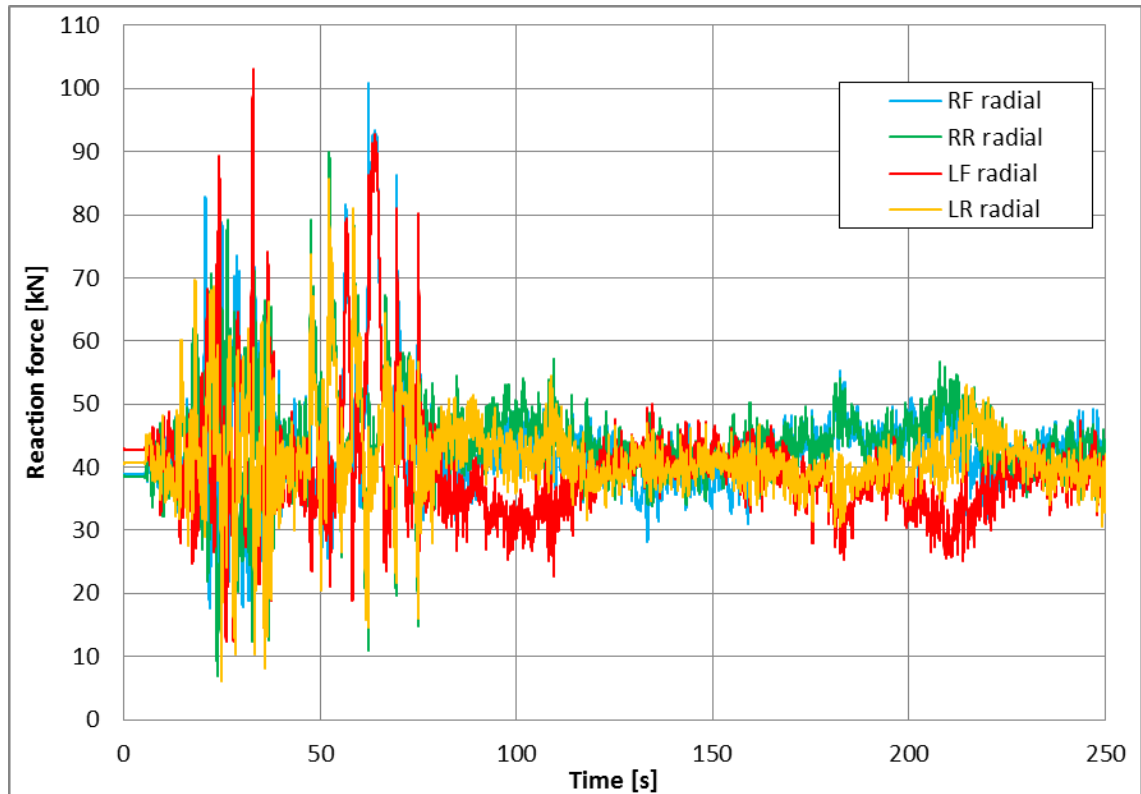


Chart 3.1. Rear frame wheel radial reaction forces measured at the test track with 12 ton load.

The right front (RF, see Figure 3.4) tire of the rear frame is the first one to hit the bump (no. 1 in Figure 3.1). This is shown as a peak in the reaction force (approximately 83 kN). The second high peak is the result of left front tire (LF) hitting bump no. 2 (approximately 89 kN). It can be seen that the forces acting on the rear tires (RR and LR) are lower than those acting on the front tires.

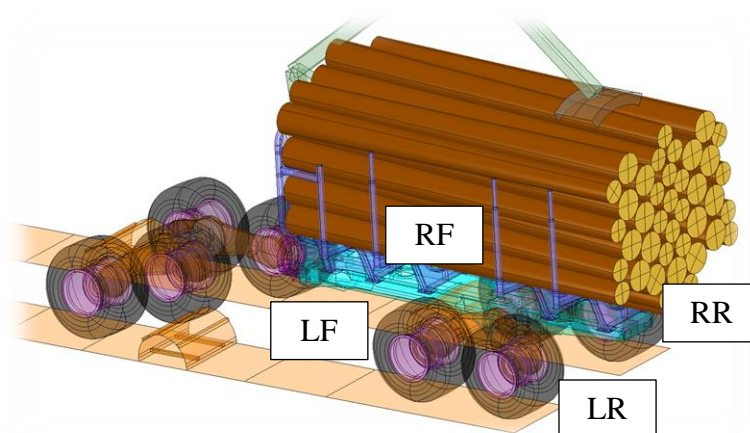


Figure 3.4. Notation of tires.

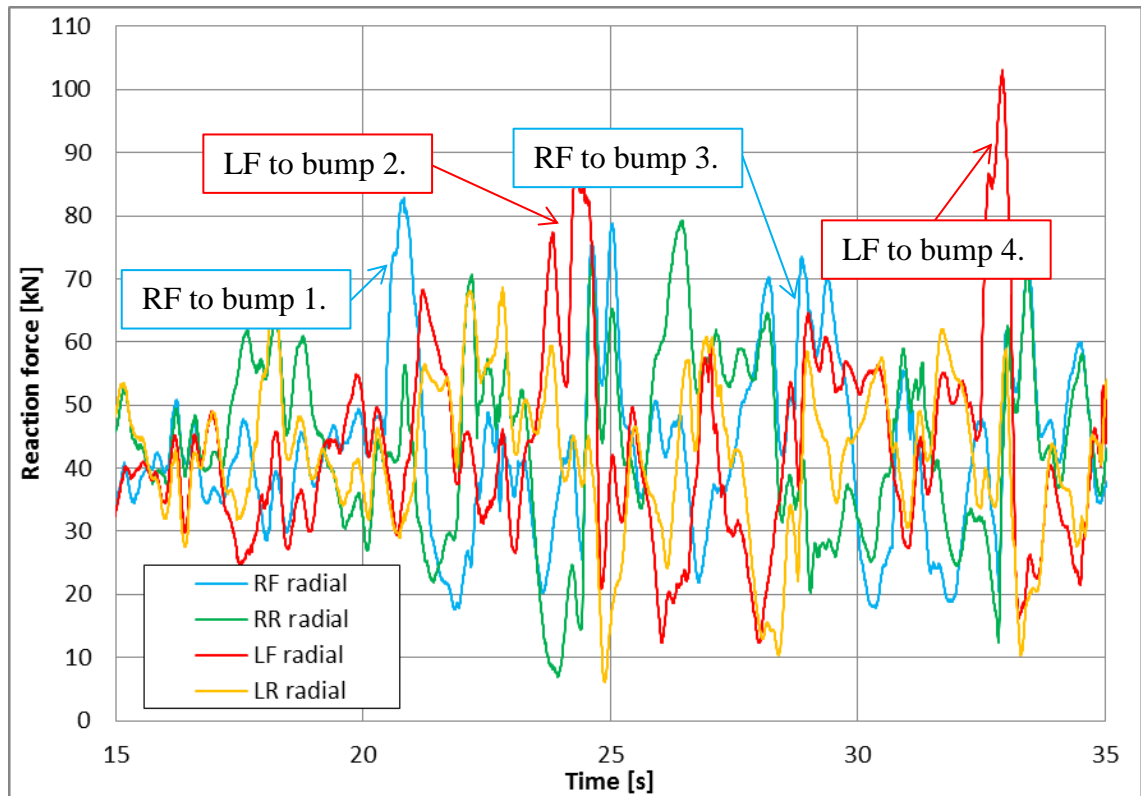


Chart 3.2. Results zoomed to crossing of the first bump track.

Results for other load cases are shown in Chapter 5, alongside with simulated results.

4. MODEL

The details of modeling for all components in the calculation model are presented in the following sections. The justifications for the chosen element types, simplifications compared to the physical real life machine and for the material models are also given. Since this is a dynamic analysis, it is important that the mass in each component is close to the mass of the real life component it represents in order to achieve correct inertial behavior. The densities of the simulation model components are modified to match weights to measured values shown in Table 4.1. Mesh and component positions at initial configuration are shown in Figure 4.1.

Table 4.1. *Measured weights of test machine components [65].*

Part	Bogie	Boom	Front frame	Load space	Rear frame	Tire assembly
Weight [kg]	1880	2573	8810	1224	1276	356

The time step is set to 2 microseconds. The minimum allowed element dimension x (see Table 2.1) for each element type using this time step size is calculated based on the material properties using Equation (9). Some elements in the vicinity of complex geometry details are smaller than the allowed minimum sizes^H presented in Table 4.2. Mass scaling will be used in these elements^I.

Table 4.2. *Minimum allowed element dimensions to reach a time step of 2 μ s, based on Table 2.1 and Equation (9).*

	E	ν	ρ	c	Hexahedral solid	Tetrahedral solid	Quad shell	Tri shell
	[GPa]	-	[kg/m ³]	[m/s]	Minimum allowable element size [mm]			
Steel	200	0.3	7850	5856	13	16	13	15
Rubber	0.03	0.49	1000	717	2	2	2	2
Wood	1.08	0.4	596	1971	4	5	4	5

The input files for the solver can be found from appendices. The inputs only include general controls and manually generated inputs since the full input file has over half a million rows and therefore would require too much space to be viewed in this report.

^H Based on defined CFL time step.

^I These elements are mostly triangular “filler” shell elements in areas where the mesher has failed to produce a fully hexahedral mesh.

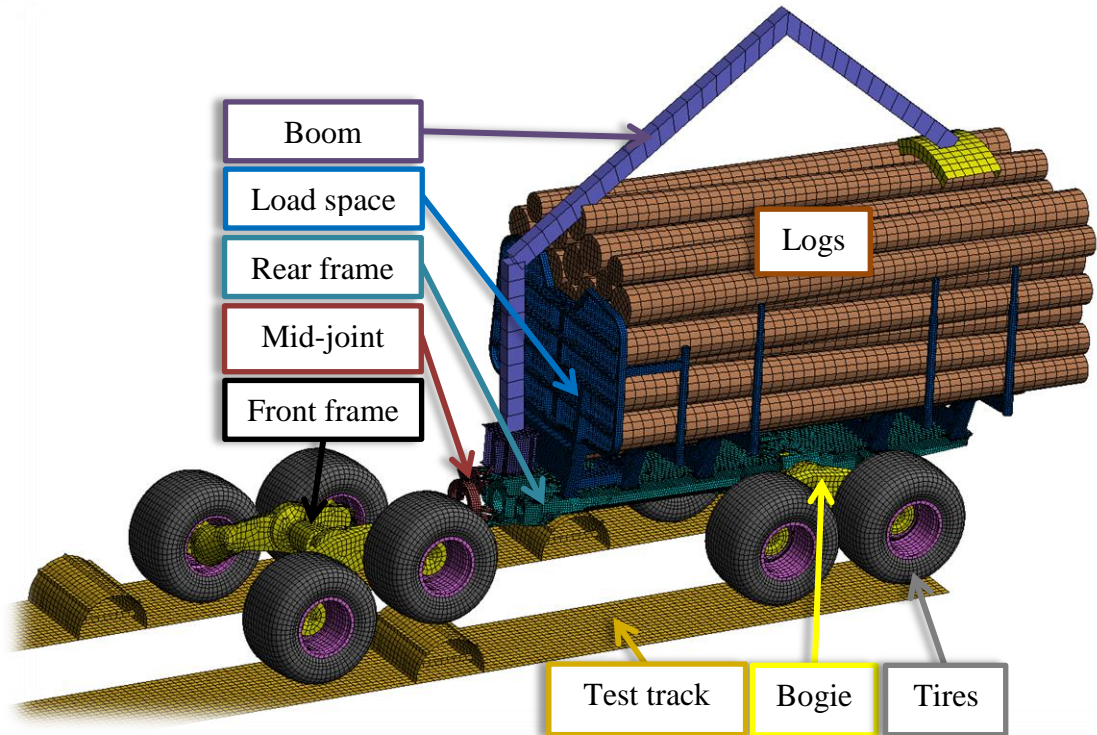


Figure 4.1. Mesh for the entire simulation model has approximately 151 thousand elements. The initial position of the machine is shown.

4.1 Bogie

The bogie is a complex cast part. It would require a fine solid mesh to capture all of its geometrical details. This would greatly affect the time step size or alternatively result as excessive mass scaling (see Section 2.4.3). Therefore the geometry is simplified to obtain smooth surfaces of uniform thickness to be meshed using shell elements. No inner structures (gears, shafts, oil) are considered in the mesh. Material density is increased to match the mass of the model and the real part. It is estimated that the bogie is significantly stiffer than the tires, thus a rigid representation is used (rigid parts are required for modeling joints). Validity of this assumption cannot be studied, however. A coarse mesh generated for bogie is shown in Figure 4.2.

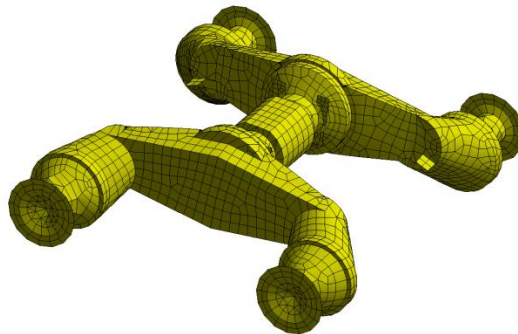


Figure 4.2. Mesh for bogie.

A constant rotational velocity is applied to revolute joints between bogie hubs and wheels. This is a simplified method that leads to some errors in accuracy of the results. See Section 6.5 for more information on this subject.

4.2 Boom

The results of the boom are not interesting in this case. During testing the grapple was resting on top of the logs. Forces and moments at the base of the boom were measured and some significant reaction moments due to boom inertia were recorded during the drive over the bump track (Section 4.3). Based on these facts, the boom model can be very simplified as long as inertial properties are included. The boom and the grapple will be constructed using rigid shell elements. The grapple is modeled only to produce a contact surface for interaction with logs. Positions for the boom at different loads are shown in Figure 4.3 and the simplified representation in Figure 4.4.

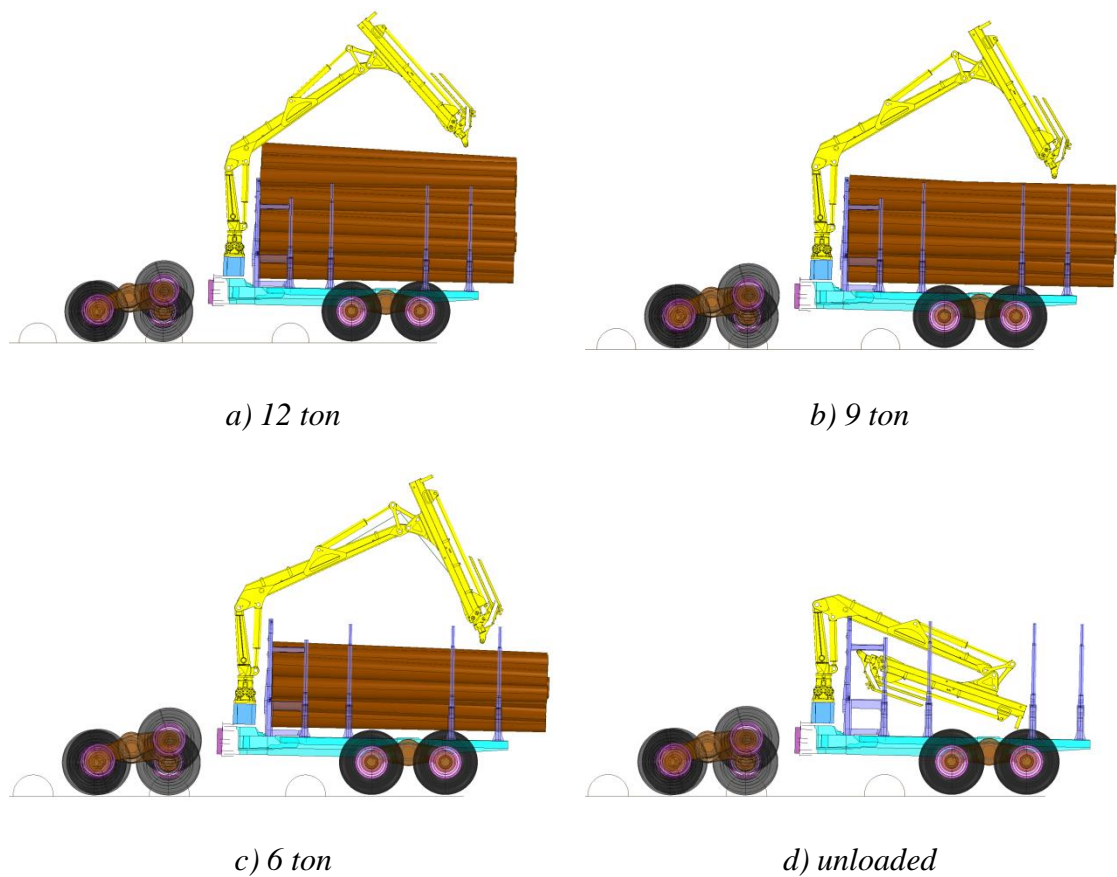


Figure 4.3. Approximate boom positions with different loads.

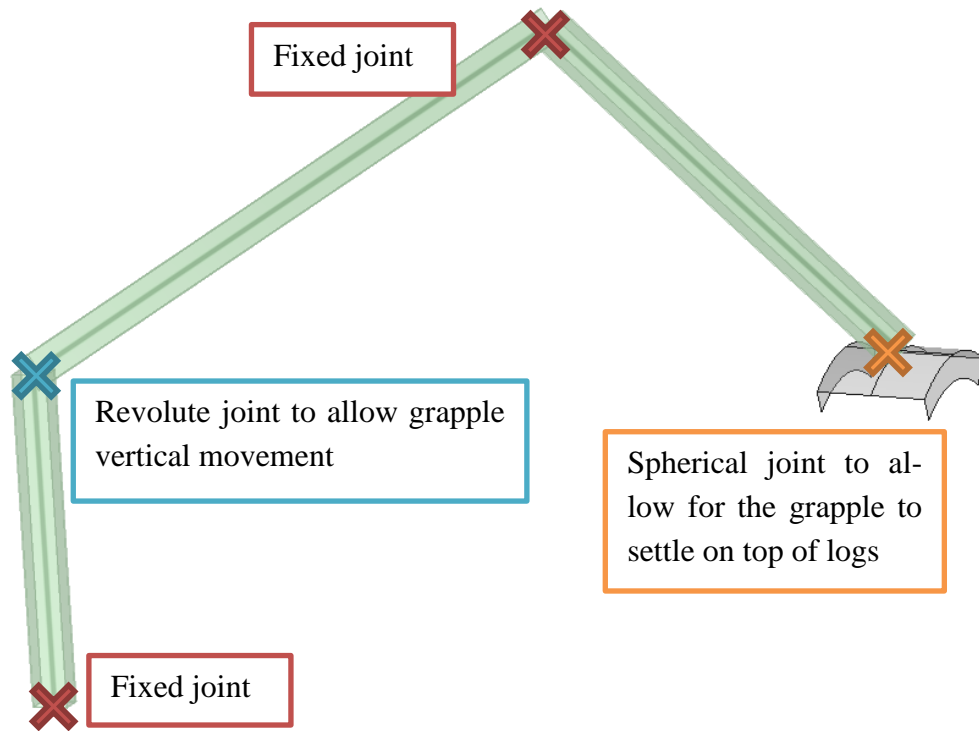


Figure 4.4. Simplified boom model (position according to 12 ton configuration shown in Figure 4.3 a)) and joint types used in it.

4.3 Bump track

Belytschko-Lin-Tsay shell elements are used for modeling the bump track. The constructed mesh is shown in Figure 4.5 and boundary conditions in Figure 4.6. Boundary conditions are rigid which might lead to overly stiff ground response, but studying the stiffness of the ground was beyond the scope of this work.

Mass damping (LS-DYNA® keyword *DAMPING_PART_MASS [44]) with a magnitude resulting as 3 %^J of the critical damping of the lowest natural frequency of the bump track is used in the analysis (see Appendix C).

^J The value is based on author's estimate.

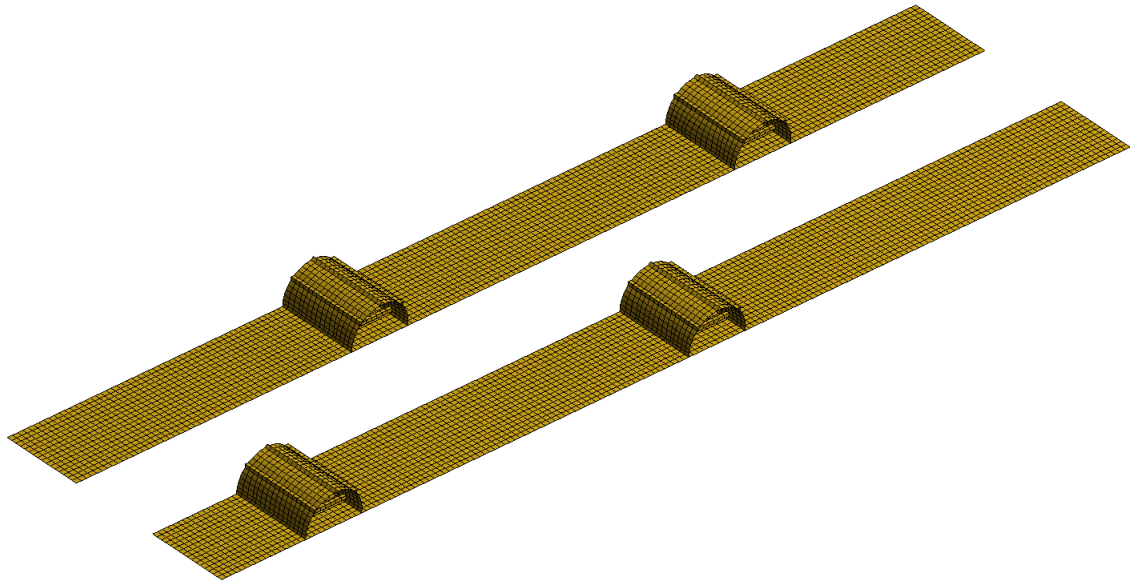


Figure 4.5. Mesh for bump track.

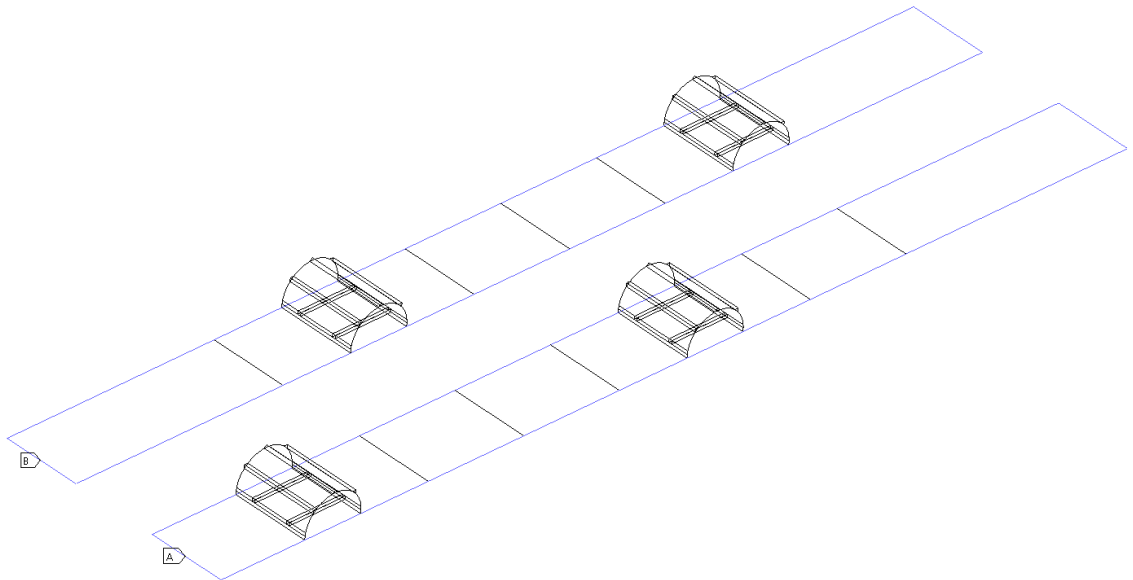


Figure 4.6. All DOFs are fixed at the highlighted edges (blue) of bump track. The structure has RHS tubes as reinforcement at these edges even though they are not visible in Figure 3.1.

4.4 Front frame

The front frame is only included in the model to obtain correct boundary conditions transmitting from the front axle to the rear frame through the middle joint (see Section 4.7). The front bogie is the same as the one used in the rear. A rigid joint is defined between front bogie mounting points and middle joint bearing (LS-DYNA® keyword *CONSTRAINED_JOINT_REVOLUTE [44]). All DOFs except for the rotation of this bearing are fixed. The mass and moments of inertia for the front frame are modeled as

point mass (LS-DYNA® keyword *ELEMENT_INERTIA) acting on Center of Gravity (CoG).

4.5 Load space

The load space is modeled using Belytschko-Lin-Tsay shell elements. The mesh is shown in Figure 4.7. The load space is connected to the frame using bonded contacts.

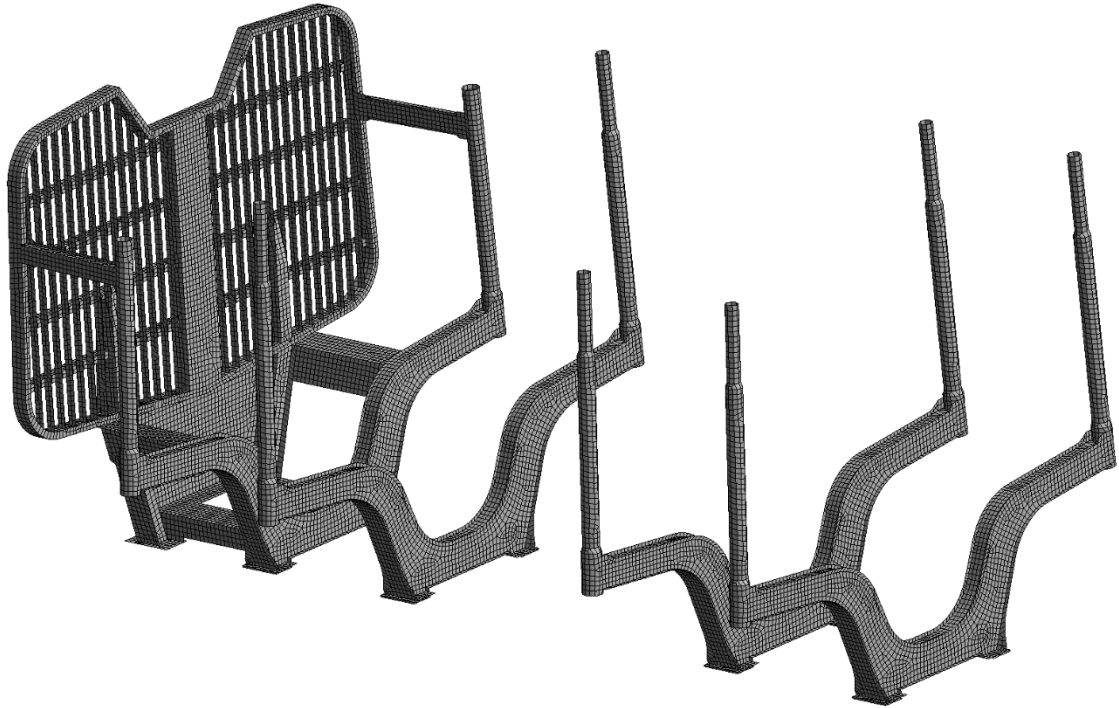


Figure 4.7. Mesh for load space.

4.6 Logs

The mechanical properties of wood vary with respect to fiber orientation, i.e. the material behavior is *orthotropic* (or *orthogonally anisotropic*). The material model used for wood is simplified to isotropic behavior since the only expected load acting on logs is radial compression. Axial (parallel to fiber direction) modulus of elasticity for pine (*Pinus Sylvestris*) is approximately 10.8 GPa and it is a function of density (and therefore a function of moisture level). Radial modulus of elasticity is in the order of one tenth of the value in axial direction. [28] Therefore a value of 1.08 GPa for elastic modulus will be used. The density of wood used in the simulation is 595 kg/m^3 to obtain a mass of 300 kg for each log (this mass helps in loading the desired test loads introduced in Section 3.3).

Logs used in the test runs are shown in Figure 4.8. An average log is estimated to have a diameter ranging from 400 mm to 300 mm as shown in Figure 4.9. A structured mesh

shown in Figure 4.10 is constructed using hexahedral solid elements (Section 2.7.1). Beam elements could also have been used in meshing the logs but the contact conditions were assumed to be more realistic by using solid elements.



Figure 4.8. Pine logs used in test runs have diameters ranging from 200 mm at top to 500 mm at base. Length for all logs is approximately 5200 mm.

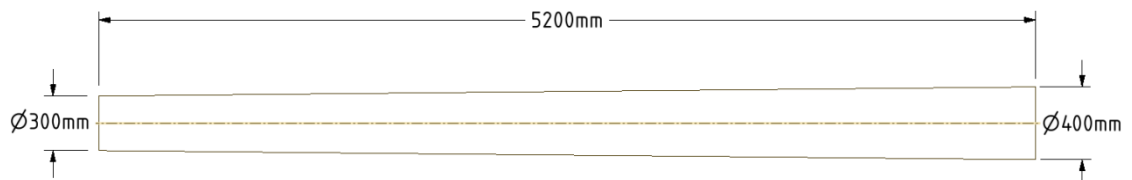


Figure 4.9. Log dimensions in simulation.

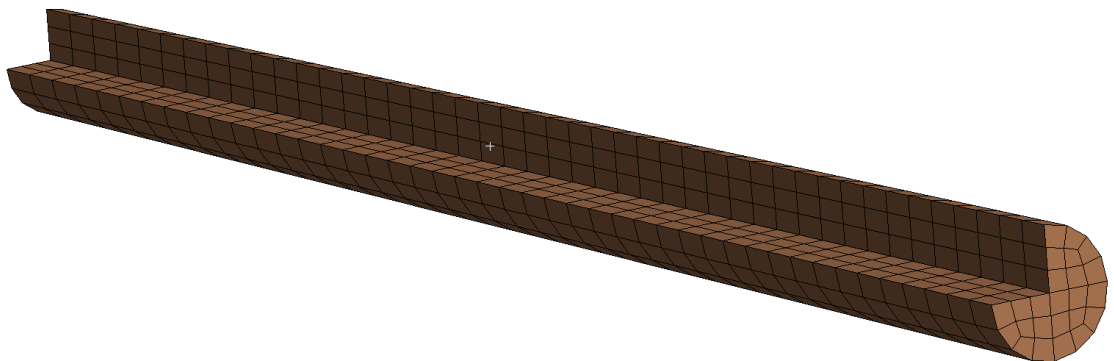


Figure 4.10. Mesh used in modeling logs. One section is removed to view mesh inside the log.

The frictional forces in the contact (LS-DYNA® keyword *CONTACT_AUTOMATIC_SINGLE_SURFACE [44]) between the load space, grapple and logs (and for log to log contact) are calculated using Equation (13) as

$$\mu = 0.2 + (0.5 - 0.2)e^{-0.5|u_f|}. \quad (59)$$

4.7 Middle joint

The middle joint is, as is the bogie, a cast iron part with complex geometric details. It is simplified to be modeled using shell elements and a rigid material model. The main function of the middle joint is to operate as a hinge for articulated steering and to allow for front frame to rotate with respect to the rear frame longitudinal axis. In this simulation the steering cylinders (see Figure 4.12) are at a fixed length to keep the machine moving straight. The mesh for middle joint is shown in Figure 4.11.

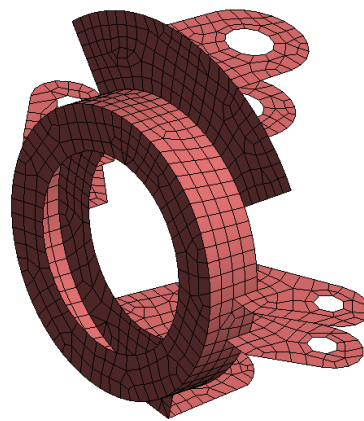


Figure 4.11. Mesh for middle joint.

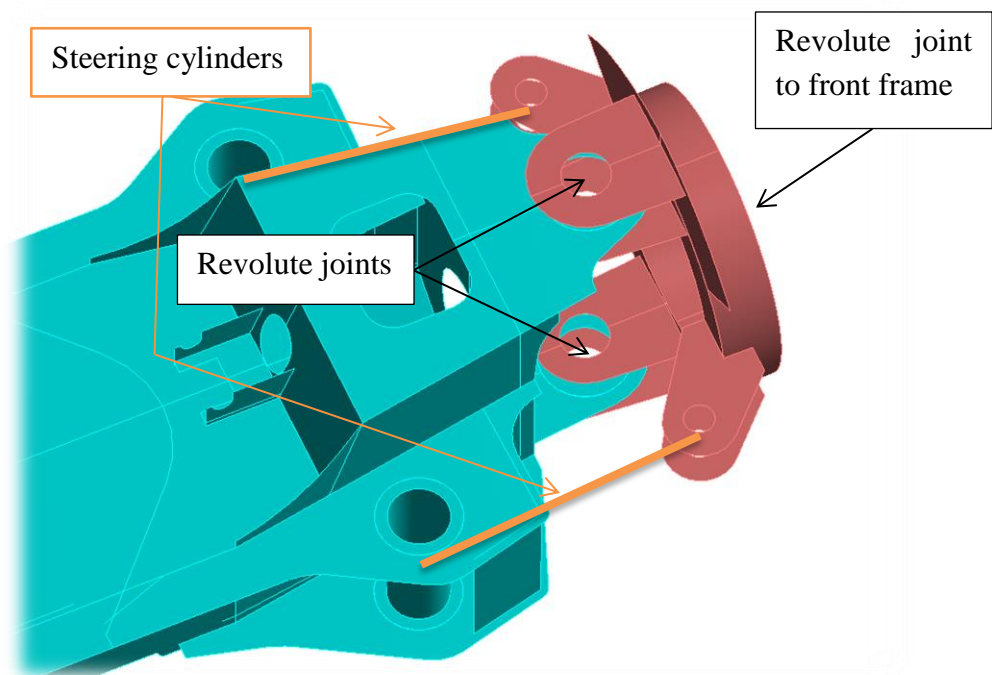


Figure 4.12. Joints in middle joint. Steering cylinders are modeled using spherical joints (rotational DOFs free, translational DOFs fixed).

4.8 Rear frame

As the rear frame consists of moderately thin (definition introduced in Section 2.7.2) sheet metal plates assembled by welding it is suitable to be modeled using shell elements. Some thick plates in the vicinity of the rear axle violate the applicability range of the Mindlin-Reissner plate theory, which might lead to errors in the results for these parts although no excessive deformation is expected in them. By using shell elements in all parts they can be directly joined together in the nodal level. If solid and shell parts are joined in the nodal level, shell rotations are left undetermined since a node of solid element has only translational degrees of freedom. To “weld” (to constrain all necessary DOFs) shell and solid parts together requires the use of some other constraint method than nodal connections (e.g. contacts). Consequently, to keep the model as simple as possible while still retaining an acceptable level of accuracy, all parts of the rear frame are meshed using the Belytschko-Lin-Tsay shell elements. Since all connecting parts are joined via shared nodes, possible reduced stiffness caused by welds with cross-sectional area smaller than of the plate’s is ignored, i.e. the welds are assumed to have a stiffness equal to the base material.

It is assumed that the heat from welding does not cause warpage to the plates or any residual stresses. No misalignment of the plates during assembly is considered. That is, the geometry is assumed to be ideal; as designed. This is expected to have a very small influence to the dynamic behavior of the structure. Residuals or imperfections are not usually accounted for in these types of analyses [41, 63]. Initial imperfections (wave-like deformations in plate fields and plate misalignments) affect the buckling resistance of the structure, but the loads used in this simulation are assumed to be much lower than those resulting as buckling (global loss of load bearing capacity).

The size of the mesh elements is a compromise between accuracy, required CFL time step, and computation time. As it was stated in Section 2.2, results should approach the continuum solution, and therefore *mesh independency*, as the element size approaches zero. However by decreasing element size, the CFL time step also decreases and the total number of DOFs for the model increases, both of which increase the total computation time. Sufficient element size was studied using *undamped modal analysis* (using explicit analysis to study mesh dependency is evaluated to be computationally too expensive).

Modal analysis solves eigenvalues for linearized form of Equation (1) when damping and external force terms equal to zero. These eigenvalues represent the modal frequencies (or eigenfrequencies, natural frequencies) of the structure. Modal shape vectors can be calculated based on modal frequencies [56]. Modal shape vectors describe the shape in which the structure sinusoidally oscillates around its equilibrium position. The solver used in calculating the modal solution is ANSYS® Mechanical *PCG (Preconditioned Conjugate Gradient) Lanczos Eigensolver* for which the Belytschko-Lin-Tsay shell el-

ement is not supported. The *SHELL181* element with reduced integration is used instead since it is closest to Belytschko-Lin-Tsay within elements supported by PCG Lanczos Eigensolver [1]. Modal analysis is conducted with different element sizes to obtain eigenfrequencies as a function of element density. The results shown in Chart 4.1 are considered to be mesh independent if eigenfrequencies do not change (within a tolerance) with further mesh refinement. If this tolerance is chosen to be 3 %, sufficient global element size is 25 mm, resulting as 21 710 elements in the model of the rear frame when studying first three non-rigid eigenmodes shown in Figure 4.14. The chosen element size is highlighted with red in Charts 4.1 and 4.2. The extremes of mesh densities used in the convergence study are shown in Figure 4.13.

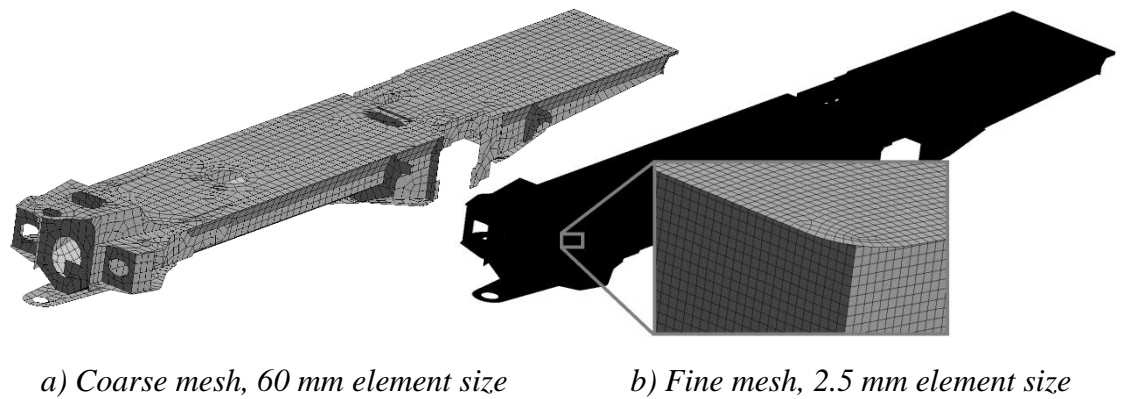


Figure 4.13. Coarse and fine meshes.

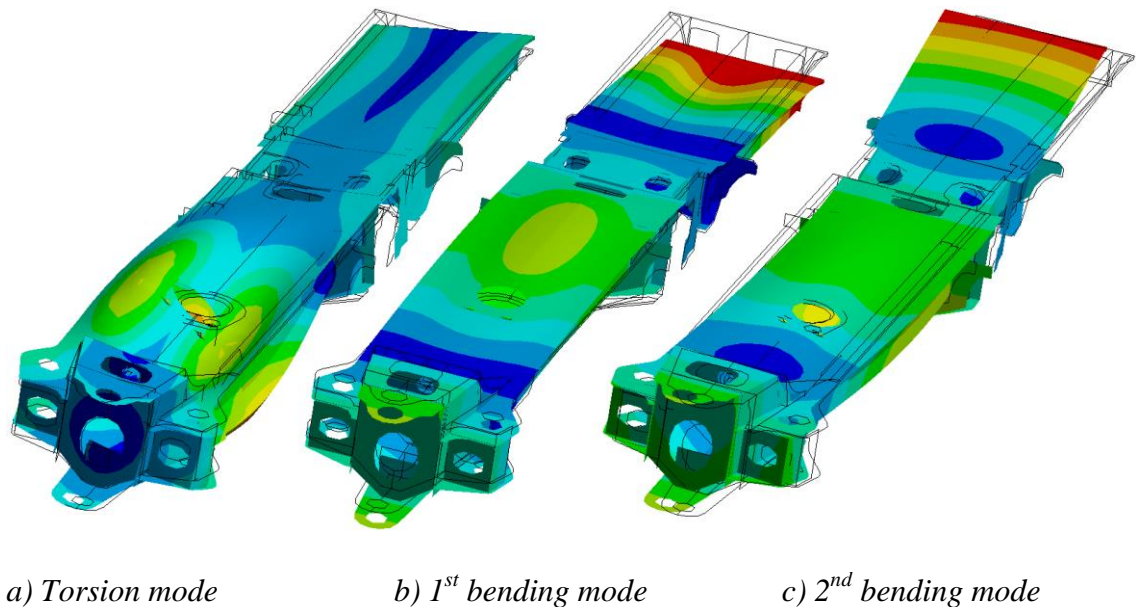


Figure 4.14. First three non-rigid eigenmodes of rear frame.

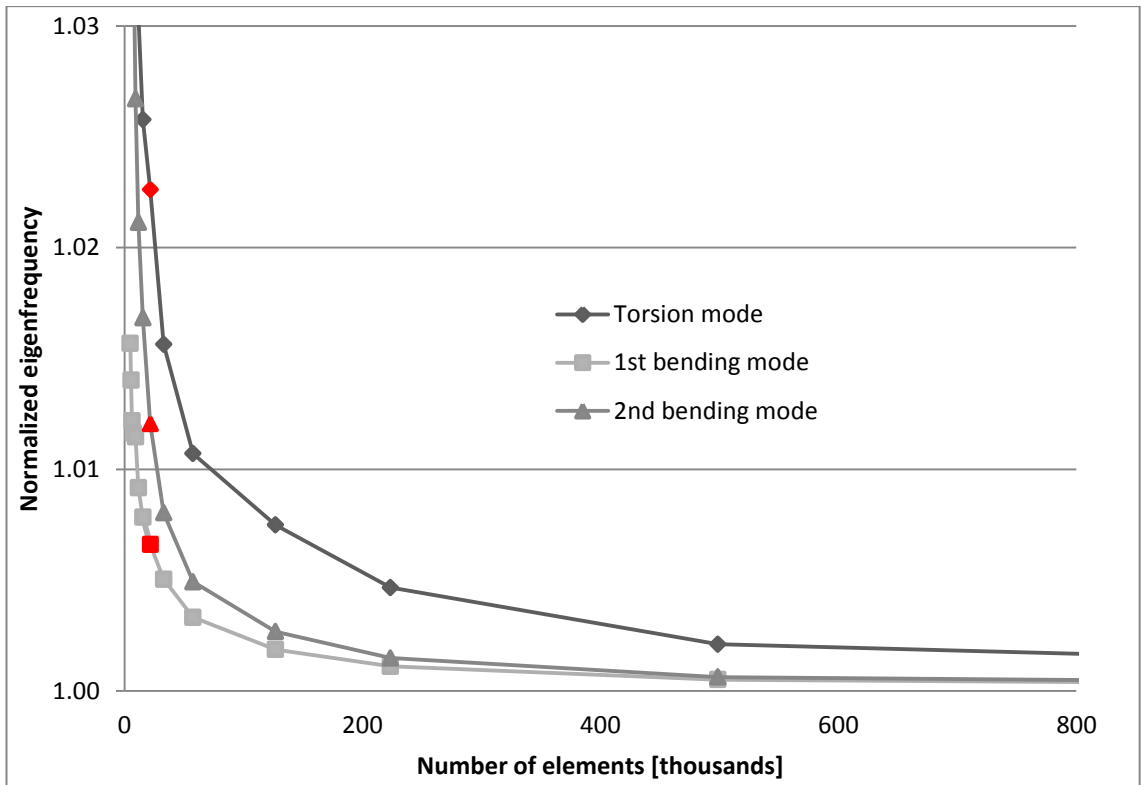


Chart 4.1. Converging behavior of natural modes shown in Figure 4.14.

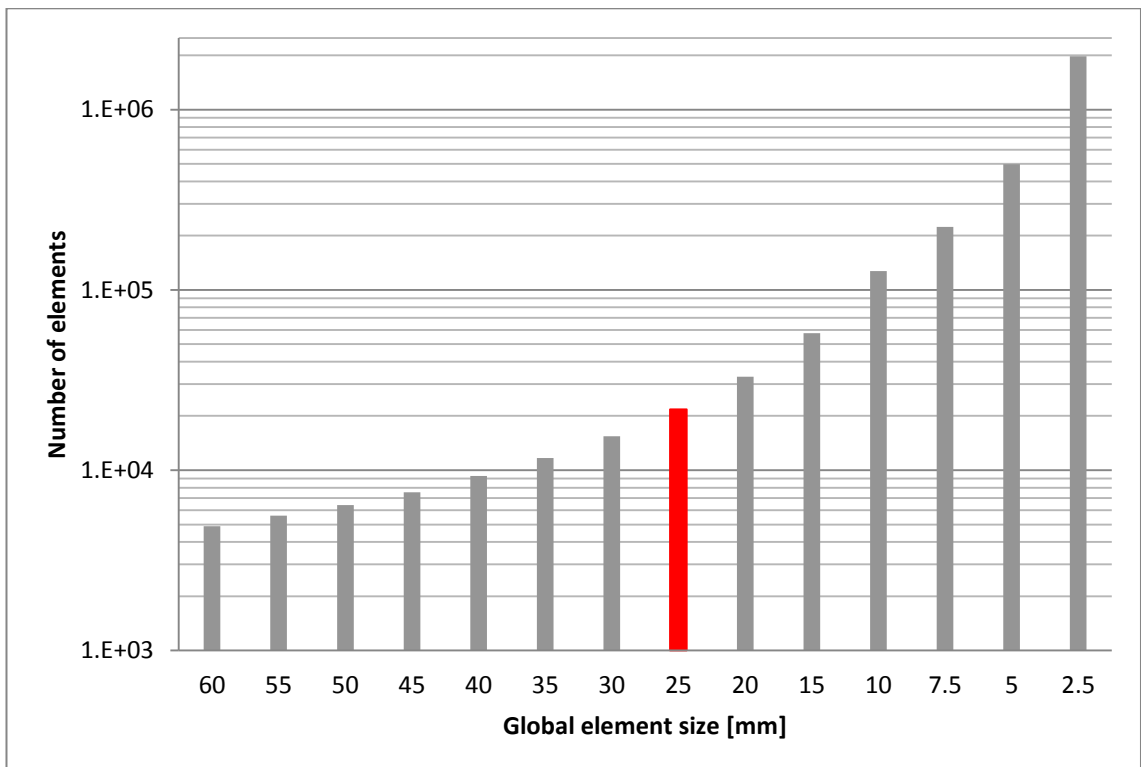


Chart 4.2. Resulting number of elements for each studied global element size.

4.9 Tires

The correct modeling of tire stiffness behavior is critical in this analysis since the forwarder does not have a separate suspension system. Tires are therefore a major contributor in the total dynamic behavior of the machine. Tire models used in some heavy machine simulations [41, 63] have been coarse since the stiffness behavior of the machine has been dominated by the suspension system (springs and shock absorbers).

Before the adoption of FEM for modeling tires, different types of empirical (such as *Magic Formula*, *Fiala*) and analytical (*FTire*, *Sharp*) models were used in studying phenomena related to tires. All of these models are designed for specific purposes and therefore are not suitable for a general case. The accuracy and level of detail in the modeling of tires using FEM has increased dramatically in the 21st century due to the growth of computational power. [14]

Accurate modeling of a tire poses several challenges:

1. Unknown material properties
 - Tire properties are altered by the manufacturers by using different types of rubber compounds
 - Tire manufacturers are not willing to hand out tire mechanical properties since they are wanted to keep as a trade secret
 - Properties of single ply (rubber matrix, belts or beads) are hard to test separately from a complete tire
 - Non-linear and hysteretic behavior of rubber
 - See Sections 4.9.2 and 4.9.3
2. Internal pressure increases as tire is compressed
 - See Section 4.9.4
3. Layered (composite) cross-section structure comprising of rubber matrix material with isotropic properties and of reinforcement belts and beads with orthotropic behavior
 - See Section 4.9.5



Figure 4.15. Studied tire, 710/40-24.5/20 Nokian Forest King F2 SF TT [50].

The tire model used in the simulation of the entire machine is the one that is evaluated to have the best accuracy to computational efficiency ratio. This ratio is evaluated by simulating a single tire and varying critical parameters. Sections 4.9.1-4.9.5 show the results of these model verification steps. The model is then validated in Section 4.9.6 by comparing the results of the optimum model to the results of static testing.

4.9.1 Mesh density

The mesh dependency of the results was studied by compressing the tire against a rigid wall using different element densities in the model. The extremities of element densities used are shown in Figure 4.16. The results in Table 4.3 show that the deflection is mesh dependent even when using the finest studied mesh (even though a converging trend can be observed). The computation time for the fine mesh model is more than ten times longer due to the higher number of elements and smaller CFL time step compared to coarse mesh model. Therefore the use of high mesh density is not practical. Since the tire cross-section layup details (Section 4.9.5) are unknown, they have to be modified to iteratively find the correct stiffness for the tire compared to experimental results (Section 4.9.6). This allows the use of relative coarse mesh since the artificial stiffness introduced by it can be compensated through altering cross-section properties.

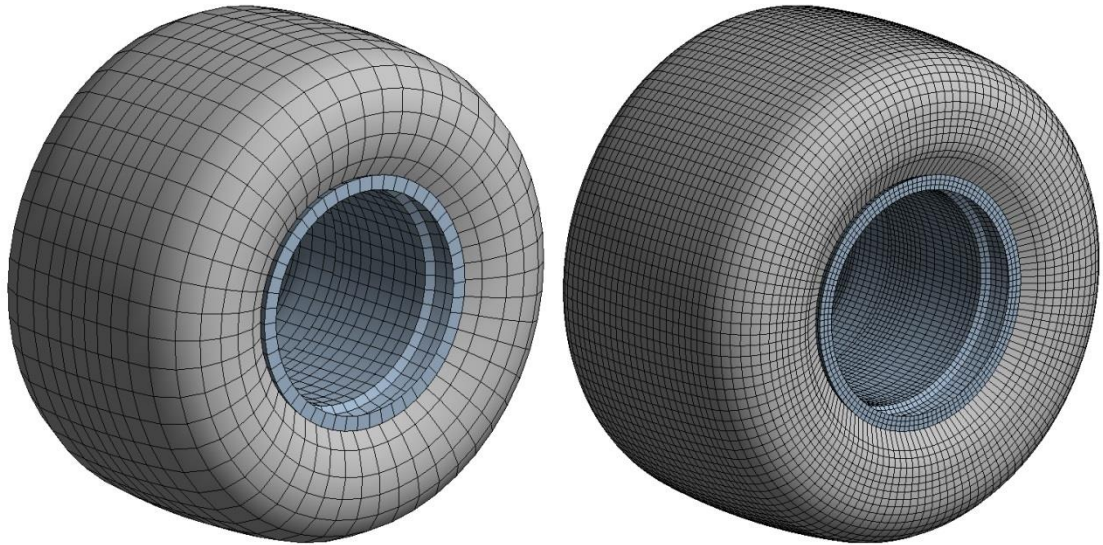


Figure 4.16. Coarse mesh on left, fine mesh on right.

Table 4.3. Results of mesh convergence study.

Elements in the tire	Normalized deflection	Change in deflection
2150	1.00	-
3780	1.26	26.4 %
6210	1.42	12.3 %
8910	1.54	8.5 %

4.9.2 Material properties

Rubber is used as a matrix material in the composite layup (Figure 4.23) and in solid treads (Figure 4.19). It is assumed to possess isotropic material properties. Since the material behaves in a non-linear manner (in the elastic region), simple constitutive relations (e.g. Hooke's Law) cannot represent the stress-strain relation correctly. In addition to this, Hooke's law is numerically incapable of modeling incompressible ($\nu = 0.5$) materials like rubber (Lamé constant $\lim_{\nu \rightarrow 0.5} \lambda = \infty$ in Equation (20)). Rubber stiffness properties also exhibit strong relation to temperature and strain rate which further complicate the implementation of universally correctly behaving material model [9, 29]. Despite these non-linearities, studies by Li *et al.* [41] and Szurgott *et al.* [63] have used a linear material model for rubber due to the fact that hyperelasticity is not supported for shell elements with layered composite properties (material properties for linear rubber are shown in Table 4.2). In this study the tire cross sections are modeled using shell elements and therefore hyperelastic relations can only be used for treads modeled with solid elements (see Figure 4.19). The stiffness behavior of the composite layup is dominated by the reinforcements and therefore the error caused by the use of linear model for rubber should not be excessive.

Constitutive relations of hyperelastic materials are commonly presented via strain energy function W which is obtained by integrating stresses with respect to strain [29, 58]. In LS-DYNA® this integral for the *Mooney-Rivlin* [48, 54] constitutive relation, which is used in some of the previous studies [30, 47, 60], is expressed as

$$W = C_{10}(J_1 - 3) + C_{01}(J_2 - 3) + (0.5C_{10} + C_{01})(J_2^{-2} - 1) + \frac{C_{10}(5\nu - 2) + C_{01}(11\nu - 5)}{2(1 - 2\nu)}(J_3 - 1)^2, \quad (60)$$

where C_{10} and C_{01} are material parameters that need to be defined based on material tests. J_1 , J_2 and J_3 are the first, second and third strain invariants, respectively (see [30 p. 12; 43 pp. 233-235; 58 pp. 200-202; 67 pp. 514-516] for further information). For incompressible materials the last term

$$\frac{C_{10}(5\nu - 2) + C_{01}(11\nu - 5)}{2(1 - 2\nu)}(J_3 - 1)^2 \quad (61)$$

is left out of the equation (otherwise would lead to division by zero). In addition, $2(C_{10} + C_{01})$ equals to shear modulus of linear elasticity. [43 pp. 233-235, 46 pp. 374-380] For some reason the Mooney-Rivlin material model (LS-DYNA® material *MAT_027 [43]) has shown excessive shear distortion compared to hyperviscoelastic model (LS-DYNA® material *MAT_077 [43]) in treads modeled with solid elements [30 pp. 13, 39]. Equation (60) is incapable of modeling the hysteretic behavior of rubber which would operate as an important energy dissipation (i.e. damping) mechanism. Despite these shortcomings the Mooney-Rivlin material model is used in this simulation for solid treads since material constants C_{10} and C_{01} for a similar tire are available [47 pp. 1126-1127].

Due to material symmetry, only two material constants are needed for isotropic materials (see Equations (20) and (21)). For orthotropic material, however, there exist fewer symmetry planes, and a total of nine independent material constants need to be defined [36 p. 85]. The reinforcement layer in the tire is modeled using an orthotropic linear material model. The stiffness of the reinforcement layer (see Section 4.9.5) in fiber direction is assumed to be dominated by steel wires, and therefore the elastic modulus is chosen as (see Table 4.2)

$$E_1 = 200 \text{ GPa}. \quad (62)$$

In direction perpendicular to the fiber, the stiffness is dominated by rubber matrix as (the stiffness is set two magnitudes larger in comparison to rubber properties in Table 4.2 to avoid tire stability issues encountered using lower stiffness)

$$E_2 = 300 \text{ MPa}. \quad (63)$$

As this is a 3D analysis, stiffness in direction normal to the laminate surface must also be defined. It is assumed to have a negligible influence to results and is chosen as

$$E_3 = E_1. \quad (64)$$

In addition to the elastic moduli, shear moduli must also be defined for three main directions as there is no similar connection as for isotropic material (see Equation (21)). The shear moduli for both directions orthogonal to the fiber are assumed to be dominated by steel properties and therefore the values to be used are adopted from isotropic steel (solved from Equation (21)) as

$$G_{23} = G_{31} \approx 77 \text{ GPa}. \quad (65)$$

The shear modulus in the fiber direction is estimated to be dominated by isotropic rubber properties. It was observed, however, that setting the modulus equal to the shear modulus calculated for linear rubber resulted as excessive shear deformations and tire instability. Therefore, instead of choosing the value for rubber, a value of steel was also set for the fiber direction as

$$G_{12} = G_{23} = G_{31}. \quad (66)$$

Six Poisson's ratios for the orthotropic layer need to be defined. The major ratios in this case are ν_{12} , ν_{13} and ν_{32} and they are estimated to be

$$\nu_{12} = \nu_{13} = \nu_{32} = 0.3. \quad (67)$$

The minor ratios ν_{21} , ν_{31} and ν_{23} can be calculated based on major ratios as [36 p. 95]

$$\nu_{ji} = \frac{E_j}{E_i} \nu_{ij}. \quad (68)$$

The most dominant value of this layer is E_1 . Other values should not crucially influence the results (other than tire stability). The above material properties are summarized in Table 4.4.

Table 4.4. *Rubber orthotropic properties (E and G in GPa).*

E_1	E_2	E_3	G_{12}	G_{23}	G_{31}	ν_{12}	ν_{13}	ν_{32}
200	0.3	200	77	77	77	0.3	0.3	0.3

Based on these values the material stiffness matrix is assembled for orthotropic material as (compare to (19)) [36 p. 96]

$$[D] = \begin{bmatrix} \frac{1 - \nu_{23}\nu_{32}}{E_2 E_3 \Delta} & \frac{\nu_{21} + \nu_{23}\nu_{31}}{E_2 E_3 \Delta} & \frac{\nu_{31} + \nu_{21}\nu_{32}}{E_2 E_3 \Delta} & 0 & 0 & 0 \\ \frac{\nu_{21} + \nu_{23}\nu_{31}}{E_2 E_3 \Delta} & \frac{1 - \nu_{13}\nu_{31}}{E_1 E_3 \Delta} & \frac{\nu_{32} + \nu_{12}\nu_{31}}{E_1 E_3 \Delta} & 0 & 0 & 0 \\ \frac{\nu_{31} + \nu_{21}\nu_{32}}{E_2 E_3 \Delta} & \frac{\nu_{32} + \nu_{12}\nu_{31}}{E_1 E_3 \Delta} & \frac{1 - \nu_{12}\nu_{21}}{E_1 E_2 \Delta} & 0 & 0 & 0 \\ 0 & 0 & 0 & G_{23} & 0 & 0 \\ 0 & 0 & 0 & 0 & G_{31} & 0 \\ 0 & 0 & 0 & 0 & 0 & G_{12} \end{bmatrix}, \quad (69)$$

where

$$\Delta = \frac{1 - \nu_{12}\nu_{21} - \nu_{23}\nu_{32} - \nu_{13}\nu_{31} - 2\nu_{21}\nu_{32}\nu_{13}}{E_1 E_2 E_3}. \quad (70)$$

4.9.3 Damping

Because none of the material models discussed above are able to simulate hysteretic energy dissipation, some other form of damping must be included to prevent excessive non-physical vibrations. Relative damping (LS-DYNA® keyword *DAMPING_RELATIVE [44]) is used for this purpose due to its ability in only damping vibrations *relative* to rigid body motions (see Appendix B). By using this method the rigid motions themselves are not damped which is a necessary property in simulating a rolling tire. This method for damping is used in recent analyses by Reid *et al.* [53] and Shiraishi *et al.* [59]. The rigid body for which the damping will be relative to in each tire is the rim.

A correct damping magnitude for rubber is evaluated to be 5 % of critical damping^K. Relative damping requires two different inputs; the frequency to be damped (FREQ) and the fraction of critical damping (CDAMP). The selected frequency is recommended to be close to the lowest eigenfrequency [44 p. 1027]. If these parameters are chosen, a high frequency eigenmode shown in Figure 4.17 is excited. This leads to sidewall instabilities and eventually to element failure as shown in Figure 4.18. The reason for the failure is insufficient damping at high frequencies since the frequencies above FREQ are damped less than the value of CDAMP whereas frequencies below FREQ are damped more [44 p. 1027]. Due to these reasons, it is necessary to either choose a high value for FREQ to damp high frequency modes (this would lead to excessive damping of low frequency modes) or use an alternative method. It was found somewhat helpful to switch the relative damping to *DAMPING_FREQUENCY_RANGE_DEFORM after damping phase at the beginning of the simulation. This method provides constant damping over a specified frequency range without affecting the rigid body motions [44

^K The value is based on author's estimate.

p. 1018]. Other measures for improving the tire stability are presented in Section 4.9.5, page 53.

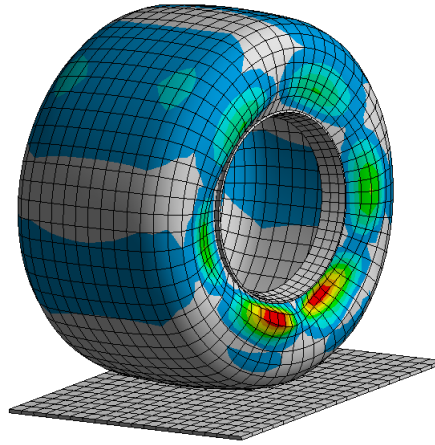


Figure 4.17. *Tire sidewall eigenmode leading to instabilities.*

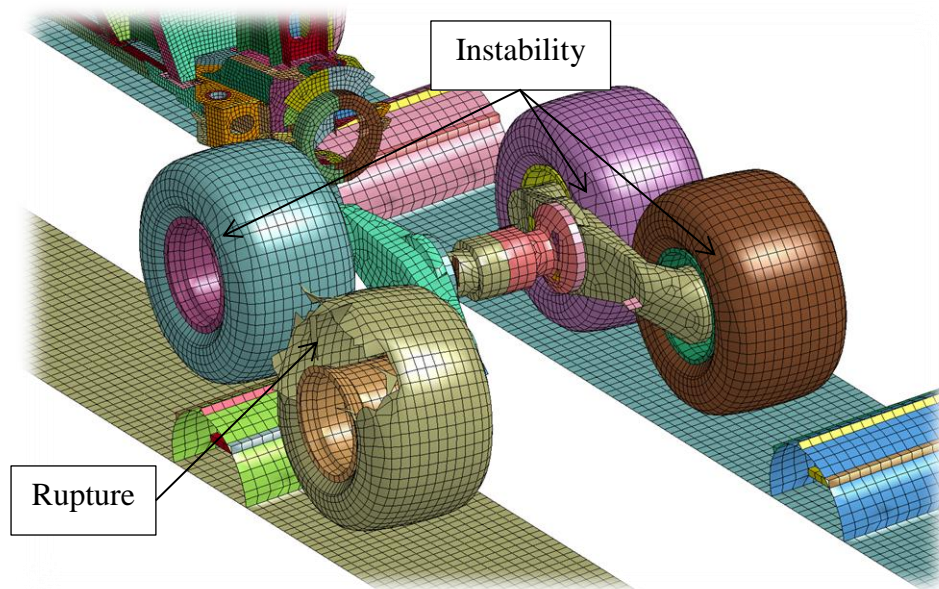


Figure 4.18. *Tire instability (all front tires) leading to rupture (RF tire) can be seen as sidewall mesh distortion.*

The instability problem was not entirely solved. Tires start to vibrate (with small amplitudes) after rigid body rotation of 180 degrees (roughly at 2.5 second after starting the simulation). These vibrations start to accumulate and eventually lead to ruptures after 4 seconds.

4.9.4 Inflation

There are different options for inflating the tire. The simplest way would be to assign a constant pressure to inner surfaces of the tire. However this method does not account for the pressure change caused by the tire compressing under loading.

To include the effect of pressure change during compression, LS-DYNA® *AIRBAG_SIMPLE_PRESSURE_VOLUME (this feature is called *airbag* for historical reasons; it was initially developed for automotive industry to model airbags) model can be used. This model computes the volume change of the enclosed “airbag” (in this case the volume of the tire) which is inversely proportional to the applied pressure [44 p. 142]. It was found that there are very little differences between results and computation times between constant pressure and airbag-model.

The third, and presumably the most accurate, option would be to model the air volume as an *ALE (Arbitrary Lagrangian Eulerian)* mesh and to use contact interactions between it and the *Lagrangian* tire. This method is computationally expensive when compared to the other two. Lagrangian reference frame is most commonly used in structural finite element calculations due to its accuracy and efficiency in representing solid structures (the entire structure in this simulation uses this frame.) [5]. ALE is a frame of reference similar to Eulerian, which is stationary in space. Unlike pure Eulerian mesh, ALE mesh can move in space (as updated Lagrangian mesh) following the material deformation. [22] Because of the small differences between results of constant pressure and simple airbag modeling techniques, ALE technique was not implemented.

Based on the above justification, the chosen pressurization technique is *AIRBAG_SIMPLE_PRESSURE_VOLUME.

4.9.5 Cross-section layup

It is not clear whether the treads should be modeled separately with solid elements or could they be ignored. This would make it possible to use shell elements (alone) to represent the tire geometry. Studies by Hall *et al.* [30] and Reid *et al.* [53] for truck tires have used a layer of solid elements in modeling the treads while studies by Barsotti [11], Li *et al.* [41] and Szurgott *et al.* [63] only use shell elements. The studied tire has relatively high tread profiles which are not axisymmetric as treads of truck tires are, but rather have cyclic symmetry as can be seen from Figure 4.15. Therefore the use of a tire model constructed purely with shell elements (and axisymmetric properties) might lead to erroneous results. However, a study by Mohsenimanesh *et al.* [47] shows that agricultural tractor tire (which also has high tread profiles with cyclic symmetry) behavior can be predicted reasonably well without explicitly modeling the treads. Due to these uncertainties the tire was modeled purely with shell elements, and, for comparison, with solid treads. Results for differences in pressure distribution, computing time and deflection are shown in Figures 4.20 and 4.21 and Table 4.5. The difference in deflection between modeling approaches is relatively small (5 %). This difference is caused by solid treads compressing at the beginning of loading. At higher loading the load-deflection curves have approximately the same slope regardless of modeling approach of treads. Since the results are consistent in both modeling approaches and solid treads increase

the computing time significantly, a tire model with pure shell mesh is chosen to be used in the simulation.



Figure 4.19. Mesh of tire model with solid treads. Nodes of solid and shell tire components are merged.

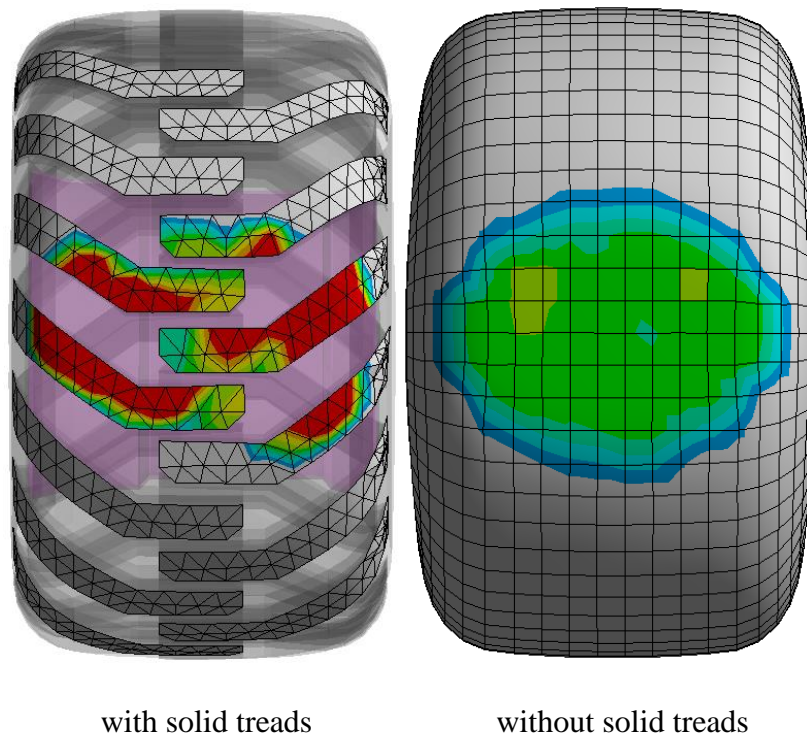


Figure 4.20. Comparison of contact pressures of different tread modeling techniques (100 kN compressing load). Pressure is higher with solid treads since the contacting area is smaller.

Table 4.5. Comparison of normalized computing times and deflections between tread modeling styles.

Tread modeling	Computing time	Maximum deflection
Shell	1.00	1.00
Solid	2.38	1.05

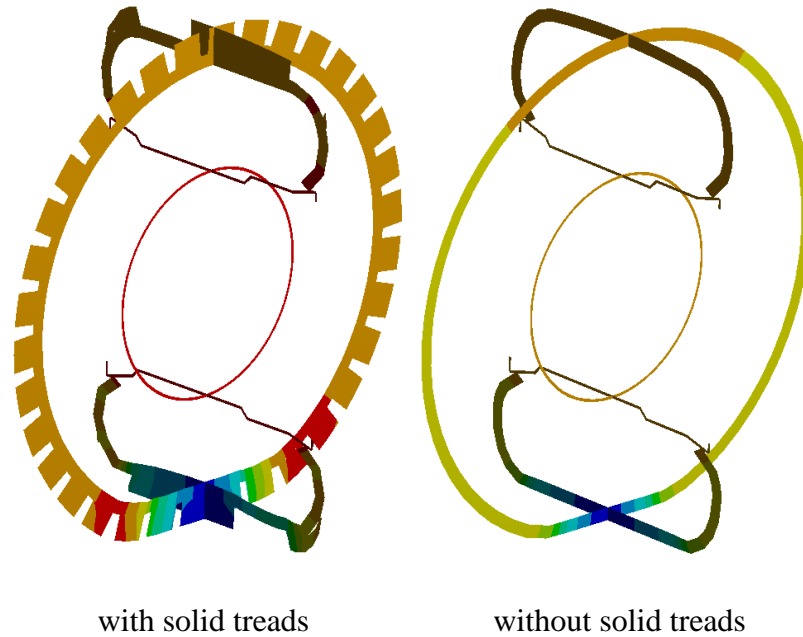


Figure 4.21. Comparison of deflected states on different tread modeling techniques (from two perpendicular cross sections).

The layup of shell elements in the tire cross section consists of a layer of isotropic linear elastic^L and homogeneous rubber with reinforcement layers (see Section 4.9.2 for material properties) in different orientations as shown in Figure 4.23 and Table 4.6. The reinforcement layers are thought to be comprised of steel wires surrounded by rubber matrix. It must be emphasized that the displayed layup is not necessarily similar to the layup of the real tire; it is rather the result of iterative process described in Section 4.9.6.

^L As was stated in Page 44, shell elements with layered properties do not support using non-linear constitutive relations.

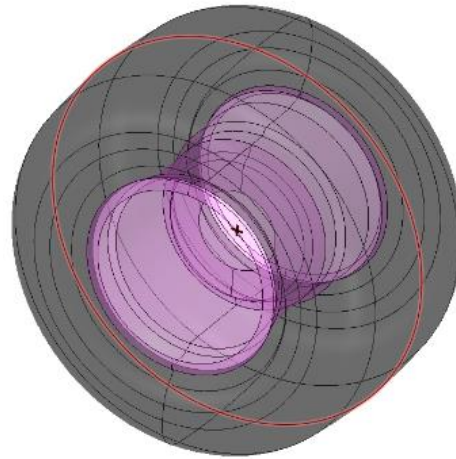


Figure 4.22. Default fiber orientation is tangential to the red line.

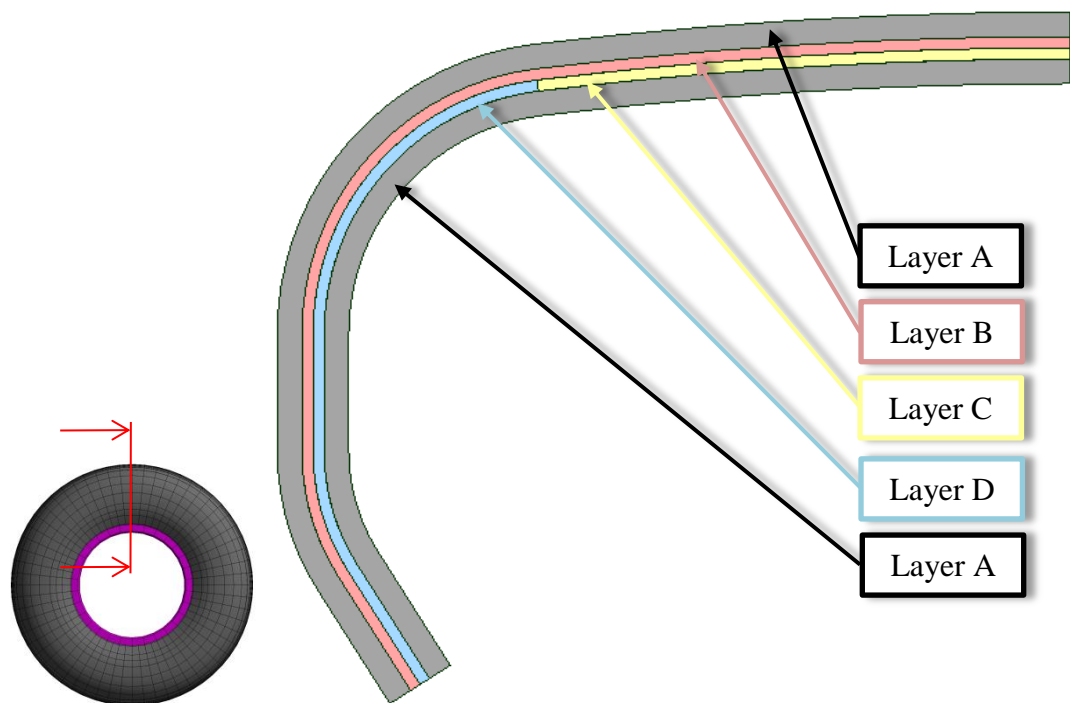


Figure 4.23. Layers of tire laminate (layer thicknesses are out of scale for better visualization).

Table 4.6. Properties of tire layers. Fiber orientations shown with respect to default orientation (Figure 4.22).

Layer	Material	Fiber orientation [°]	Layer thickness [mm]
A	Linear rubber (see page 44)	-	15
B	Orthotropic reinforcement (see page 45)	90	0.22
C	Orthotropic reinforcement	0	1.1
D	Orthotropic reinforcement	0	0.22

It was found through preliminary analyses that the under-integrated Belytschko-Lin-Tsay shell was unstable in modeling the tire, and therefore it cannot be used. A more robust fully integrated shell element (LS-DYNA® type 16 [46 pp. 169-173]) is used instead. This element is also reported to be used in studies by Barsotti [11] and Shokouhfar *et al.* [60]. Due to full integration, hourglass modes will not be present in the tire with the exception of transverse shear modes^M that will be damped using hourglass control type 8^N with a coefficient of 0.1 [24; 44 p. 1506]. This method of hourglass damping was also used by Barsotti [11]. To further improve stability of rotating components, second order objective stress update (based on Jaumann's stress rate) is activated (*CONTROL_ACCURACY keyword flag *OSU=1 (Objective Stress Updates)*) as was also done by Barsotti [11] and Reid *et al.* [53]. See Section 4.9.3 for more efforts on improving tire stability.

4.9.6 Static testing

A series of static radii results for different compressive forces and inflation pressures were obtained from Nokian Tyres [64]. The uncompressed static radius was however not provided; it was read from a *CAD (Computer Aided Design)*-model to be 615 mm. Vertical tire deflections shown in Chart 4.3 with polynomial trend lines are calculated based on these static radii.

To obtain correct cross section properties, an iterative process of comparing the simulation results to the measurements [64] and then modifying the cross-section properties was conducted. The final results (with optimized layer thicknesses shown in Table 4.6) are shown in Chart 4.4. The cross section properties are adjusted to obtain good agreement with nominal pressure (500 kPa) and moderate loads. The results show overly soft behavior with underinflated tire (400 kPa) when compared to the measured results. This might be caused by severe bending moments experienced by tire (support from internal pressure is lower) elements connected to the rim (see Section 6.7 for description of the problem).

^M Reduced integration is used in this direction, which makes the element *SRI (selective reduced integrated)*.

^N Full projection warping stiffness.

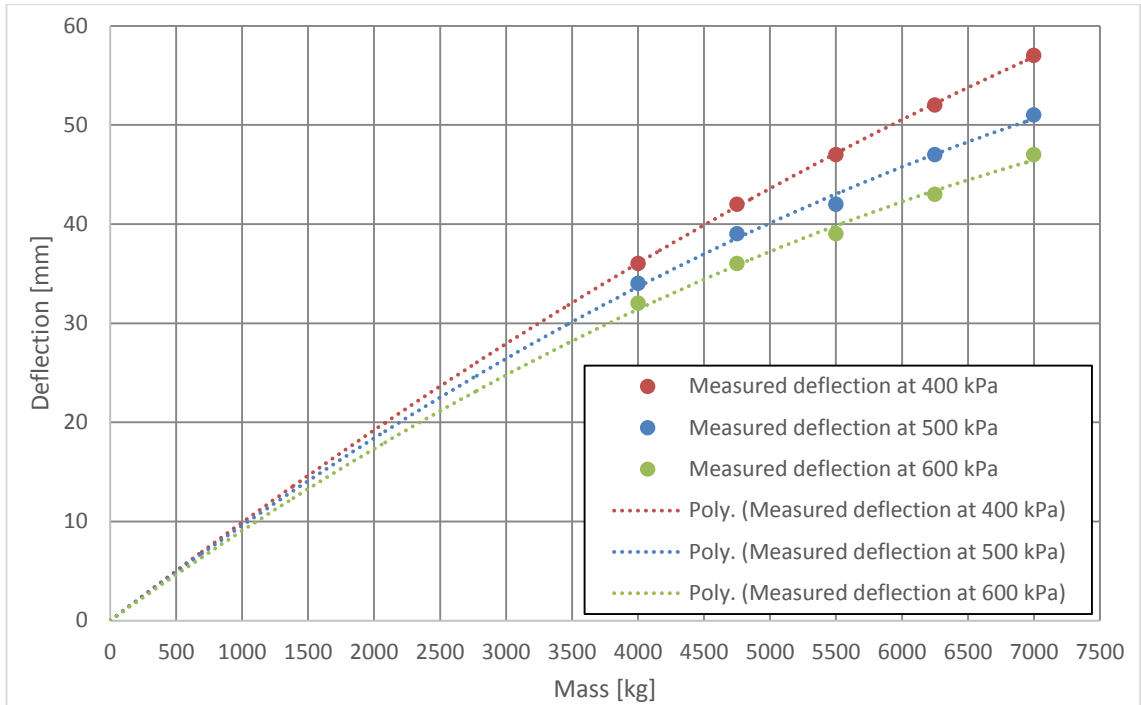


Chart 4.3. Measured static radii and trend lines crossing at origin.

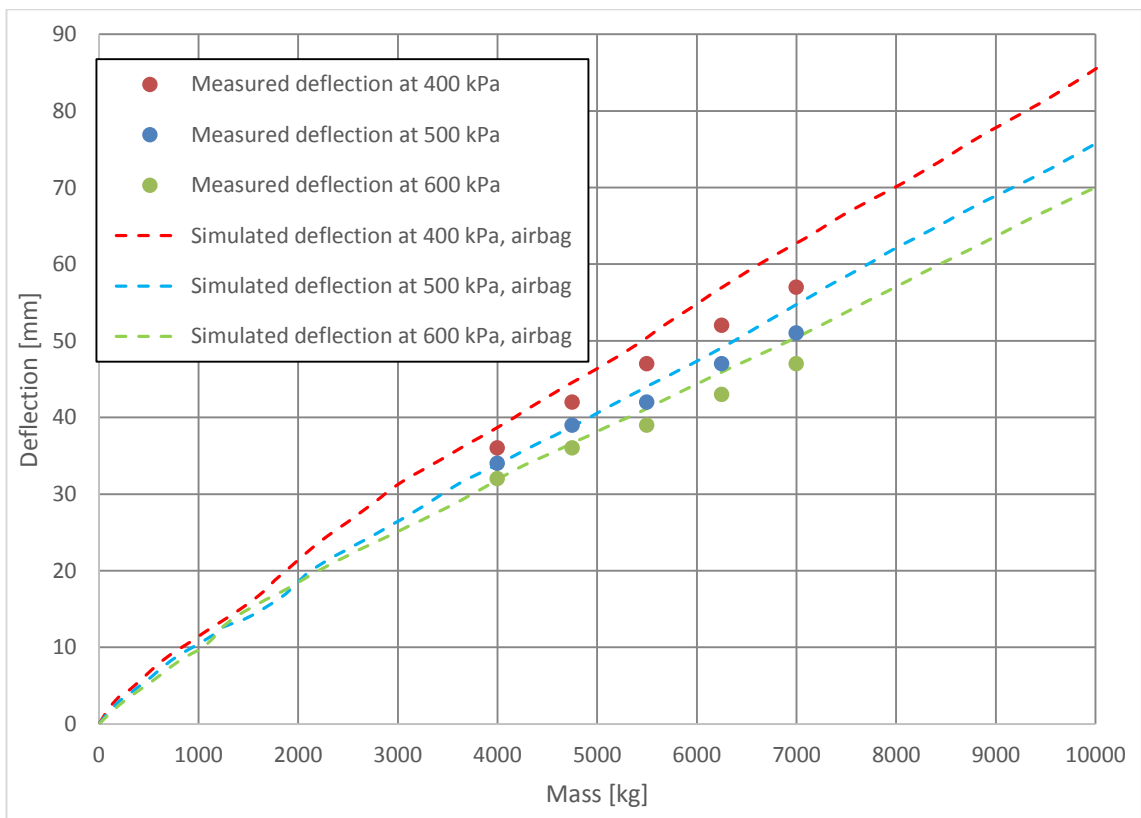


Chart 4.4. Comparison of simulation results to measured data show satisfactory agreement.

Although comparing simulation model results to a dynamic test results (such as the *cleat test*) would have also been important, no data were available for this. The damping properties of the tire would have been acquired from dynamic test results.

4.9.7 Friction

The friction coefficients in the contact between tires and the test track (LS-DYNA® keyword `*CONTACT_AUTOMATIC_SURFACE_TO_SURFACE` [44]) vary with respect to moisture level and other ambient conditions. Therefore the coefficients are only estimates. The friction is calculated for tire-track contact using Equation (13) as

$$\mu = 0.4 + (0.6 - 0.4)e^{-0.5|u_f|}. \quad (71)$$

Friction affects the results and therefore a sensitivity study regarding tire to test track friction is performed in Section 5.4.4.

4.10 Analysis sequence

At the beginning of the simulation, tire pressure (Section 4.9.4) and earth gravity are stepped on. During the first 500 milliseconds of the simulation, damping on the model (Sections 2.6 and 4.9.2) is kept artificially high, approximately at critical damping, to diminish transient oscillations caused by stepped loads (dynamic relaxation). The tires compress and logs and boom find their correct positions during this damping phase (tires need at least 100 ms to compress due to their natural frequency). After 500 milliseconds the damping is lowered to a normal level.

Translational initial velocity is applied to the machine after 300 ms of simulation. At the same time, rotational velocity is applied to all tires (Section 4.1). This rotation will be doing work to the domain and thus keep the forwarder moving. Initial kinetic energy (introduced by initial velocity) of the machine is not sufficient to keep the machine moving throughout the simulation.

The analysis sequence is visualized in Figure 4.24.

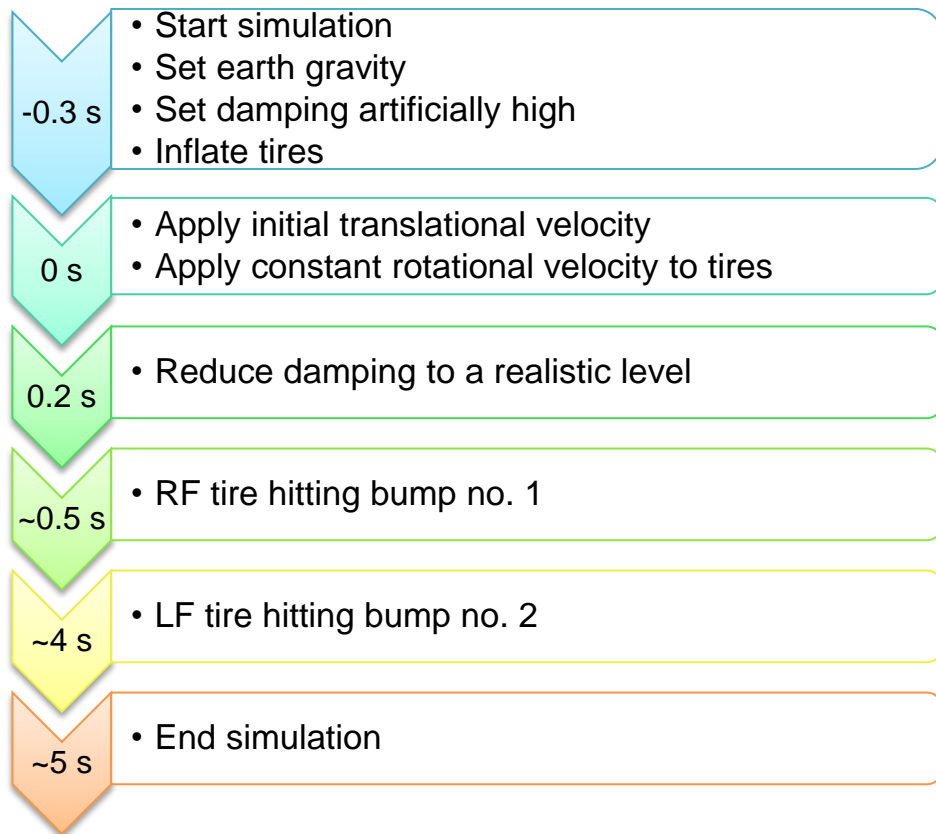


Figure 4.24. Analysis sequence. Zero time is set to the phase when velocities are applied (this is done only for convenience since the results of the damping phase prior to setting initial velocities are not interesting).

5. RESULTS

All results from the simulation are recorded at intervals matching to the sample rate of measured quantities (see Section 3.4). Therefore the phenomena that have a timescale shorter than this are not captured. The horizontal time axes of the measured results are moved to match the sequence presented in Figure 4.24.

The rear frame tire forces (Section 5.1) are displayed for all studied load cases whereas other results (Sections 5.2-5.4) are only shown for the 12 ton load since the forces acting on this load case are the largest (and therefore also deformations, stresses and amount of mass scaling are most significant).

The machine position at different stages of the simulation is shown in Appendix F.

5.1 Tire forces

The forces acting on the tires have the highest values in the 12 ton load case. Therefore the reporting of forces for this load case will be more thorough than for the others.

Each of the following sections contain radial tire force results for each rear frame tire (see Figure 3.4) as a function of time. The simulated (Chapter 4) and measured (Chapter 3) results are plotted to same graphs to be compared for validation (Section 2.2). For the 12 ton load case, the radial forces of right hand side tires are also decomposed in vertical (normal to ground) and horizontal (parallel to driving direction) components to better understand the radial results.

Measured radial tire forces for RF tire in different load cases are shown in Chart 5.1 for comparison. Force peaks in 9 and 12 ton load cases are surprisingly similar, 9 ton load case peaks are locally even higher than in 12 ton load case. The measured rear frame tire forces at unloaded load case^o are lower than anticipated based on machine weight (see “*RF Radial, Measured, 0 ton*” at $0 \leq t \leq 0.5$ s in Chart 5.1).

Similar to measured values in Chart 5.1, Chart 5.2 shows the simulated values in comparison. A 6 ton load case was also simulated, but the measured results for it were unus-

^o The mass of the rear frame should be evenly distributed to all rear frame tires when the machine is moving in planar surface. The horizontal tire forces are negligible at this phase ($0 \leq t \leq 0.5$ s) and therefore the average value of the tire force resultant should correspond to the weighed [65] static values. For unloaded load case in Chart 5.1 this measured resultant force is approximately 3 kN when the correct value would be approximately 18 kN [65].

able (the results for studied part of the test track was missing). Therefore the only results for 6 ton load case are the ones presented in Chart 5.2.

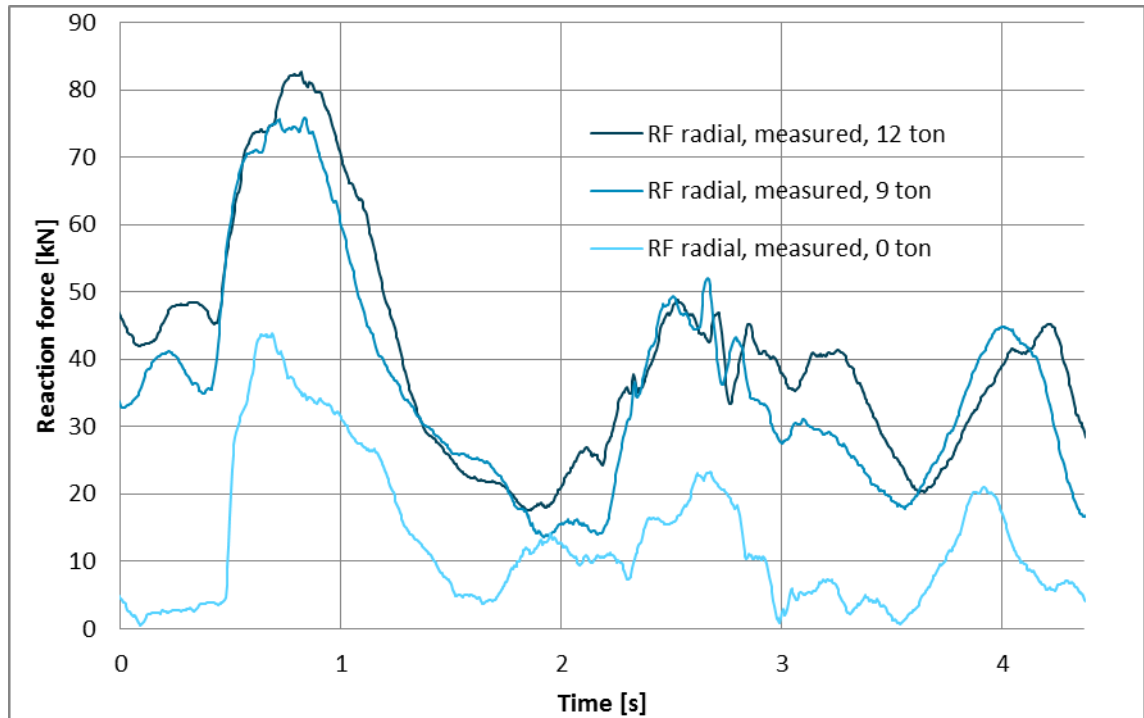


Chart 5.1. *Measured radial reaction forces of RF tire compared for different load cases.*

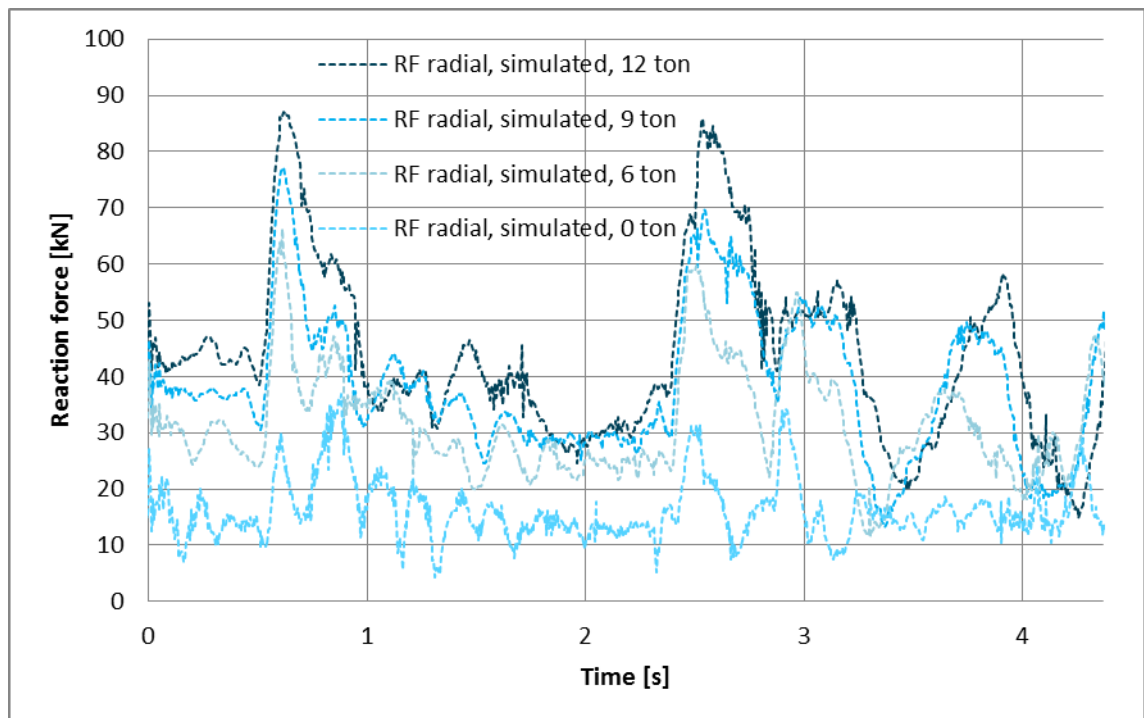


Chart 5.2. *Simulated radial reaction forces of RF tire compared for different load cases.*

5.1.1 12 ton

Immediately it can be seen that the simulated results are more “restless” on high frequencies (small short duration oscillations) compared to measured results. This suggests that the damping values used on high frequencies should be higher on the simulation model (Section 4.9.3).

As can be noted from Chart 5.3, the horizontal force peaks on right hand side tires (also holds true for left hand side tires) are opposite in sign, meaning that the resultant horizontal force of the tire pair, shown in Chart 5.4 (sum of RF and RR forces), does not have oscillations as high as individual tires do. The first horizontal peak at RF tire occurs at $t \approx 0.7$ s. This is, as was stated in Section 3.5, caused by the tire hitting bump no. 1. An opposite reaction for this peak with a smaller magnitude can be seen in RR tire.

The second force peak occurs at $t \approx 2.7$ s, when both right-side tires are at bump no. 1 (see Figure 5.1 and Appendix F). These peaks are larger in simulation model than they are in reality. It is estimated that this is caused by the constant rotational velocity applied on the rims (see Section 4.1). In the physical machine the tires are not forced to rotate at exactly same velocity at all times. The use of a differential and a torque limiter, presented in Section 6.5, might improve results in this area. The friction between the test track and tires (Sections 4.9.7 and 5.4.4) also plays an important role in the horizontal forces; differences can be explained to some level by a possibly different tire grip on field test and simulation. One more possible explanation for the second force peak is the stiffness of the fixed boundary condition used for the test track (see Figure 4.6); in reality the ground response might be softer, resulting as lower force peak.

With the exception of difference between second force peak results, the simulated horizontal forces correlate well with the measured values.

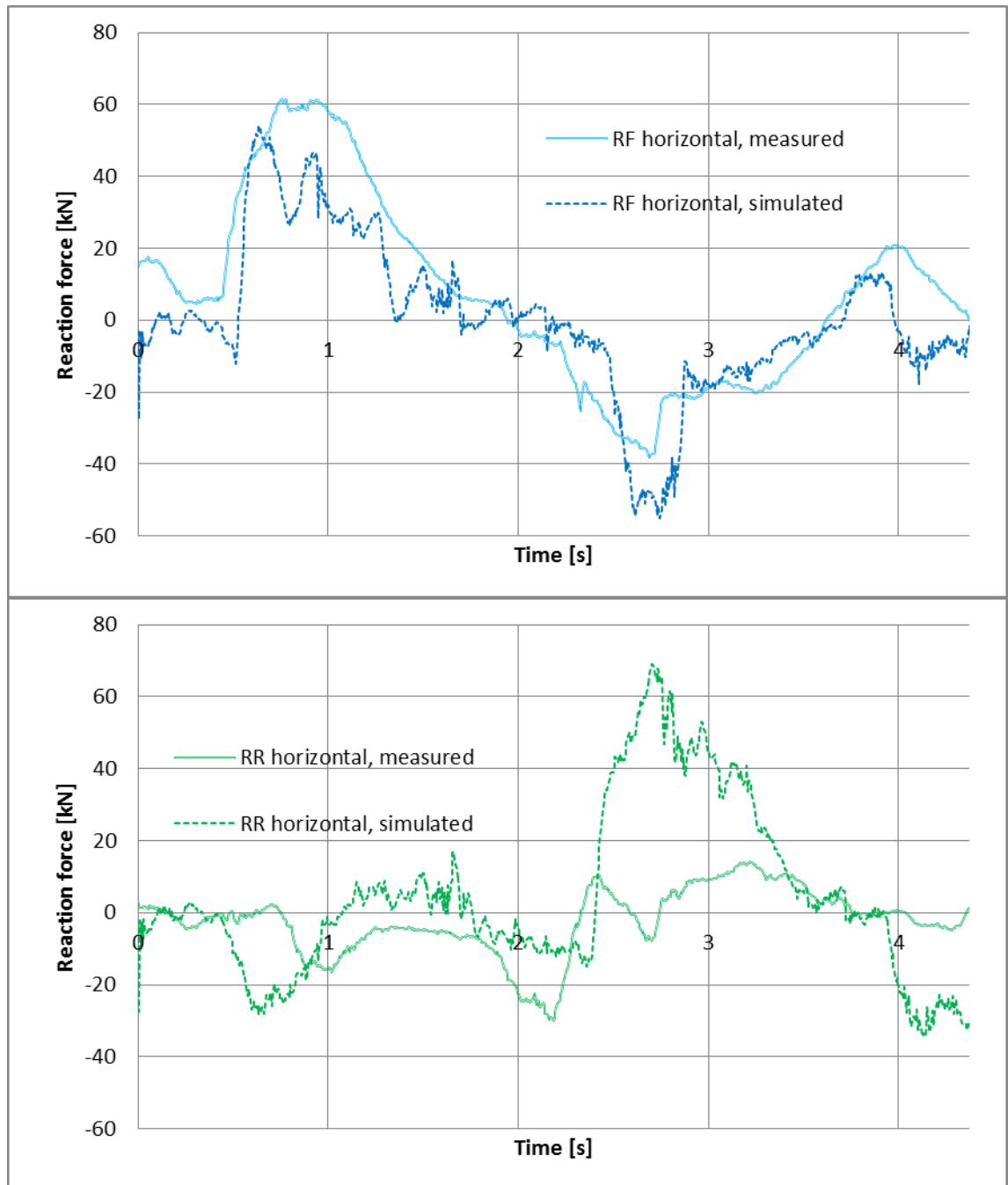


Chart 5.3. The horizontal forces of the right-side tires of the rear-frame.

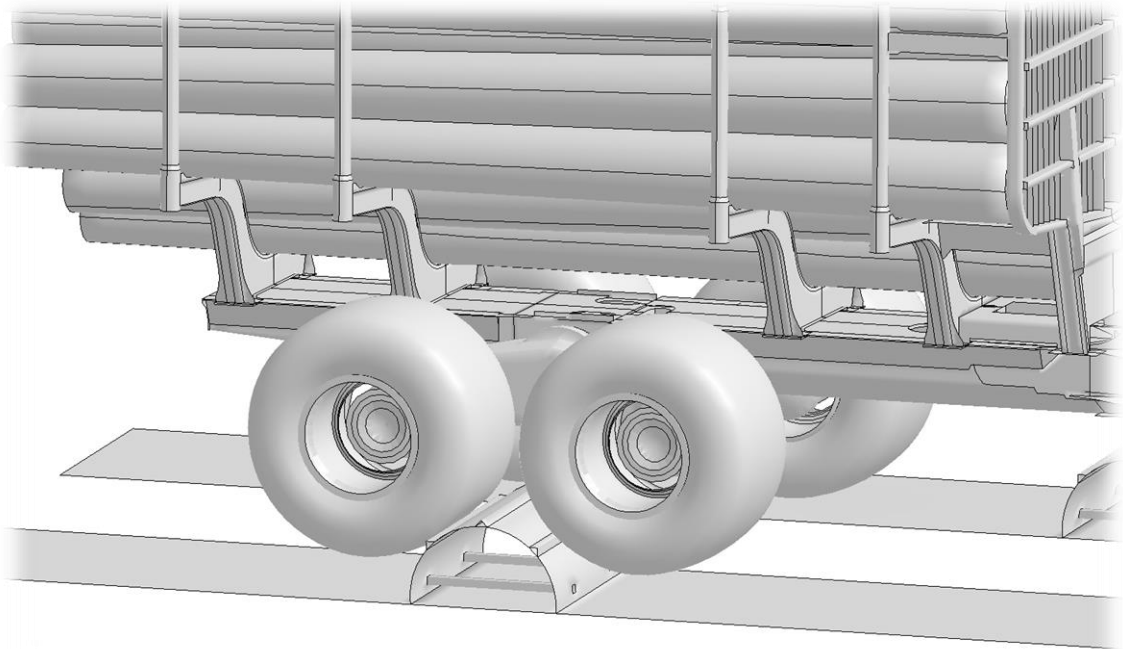


Figure 5.1. The right-side tires of the rear frame crossing bump no. 1 at $t \approx 2.7$ s.

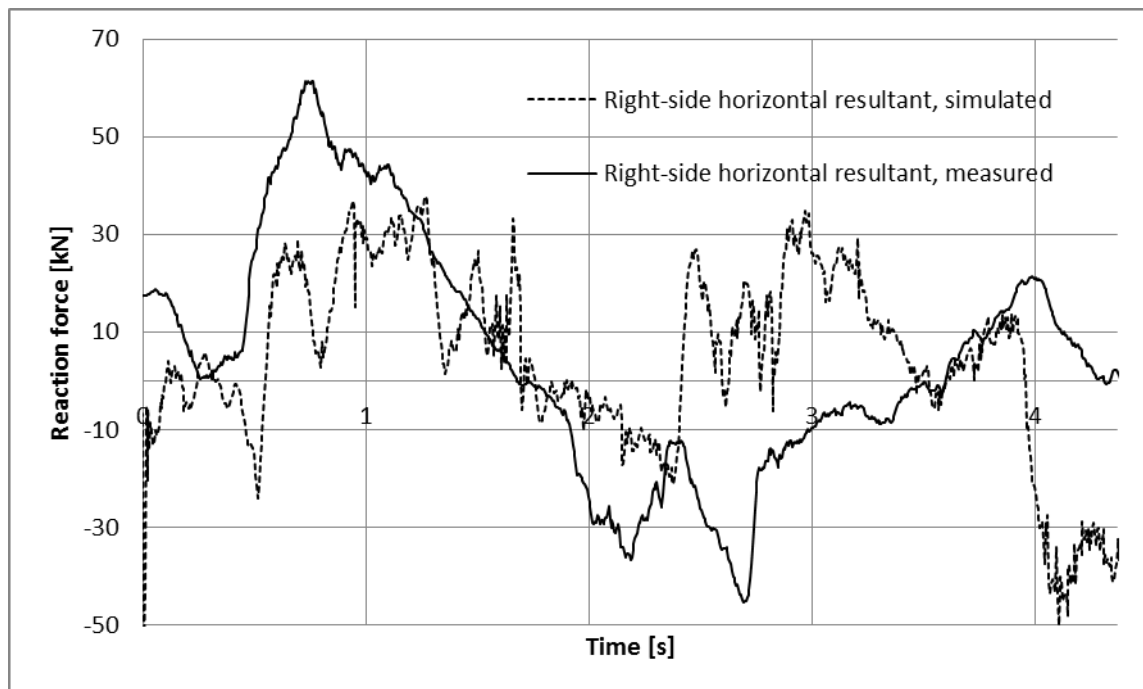


Chart 5.4. Sum of horizontal forces of right hand side tires (RF and RR in Figure 3.4).

Vertical forces shown in Chart 5.5 also experience a peak force when RF tire collides to bump no. 1. The machine rear frame tilts around its longitudinal axis as right hand side tires cross the bump ($1\text{ s} < t < 2\text{ s}$). This tilting causes the rear frame CoG to shift towards the left hand side tires. This can be seen as reduced vertical reactions on the right hand side. Similarly the reactions increase on the left hand side. A high peak is observed

at $t \approx 2.7$ s. It is estimated to be caused by same reasons as the horizontal peak (see page 59).

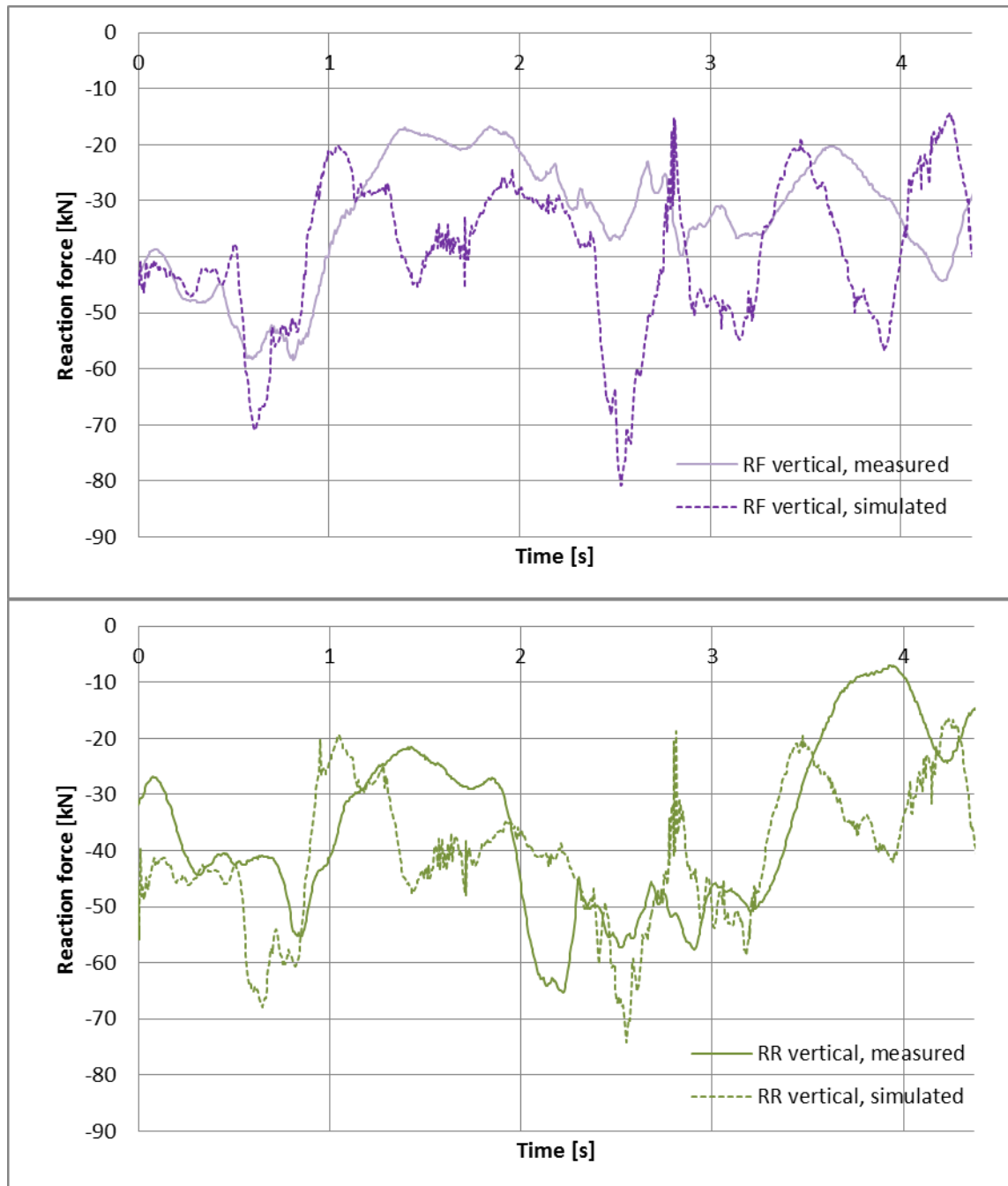


Chart 5.5. *The vertical forces of the right-side tires of the rear-frame.*

Charts 5.6-5.9 show the radial reaction forces acting on the tires. Radial force is the resultant of horizontal and vertical force vectors. The correlation is reasonable with the exception of the force peaks discussed earlier. Some temporal deviation between simulated and measured force peaks are observed at $t > 3$ s. This can be interpreted as the physical machine slowing down since the measured peaks occur later than the simulated one. The simulated peak of LF tire hitting bump no. 2 is higher than the measured value.

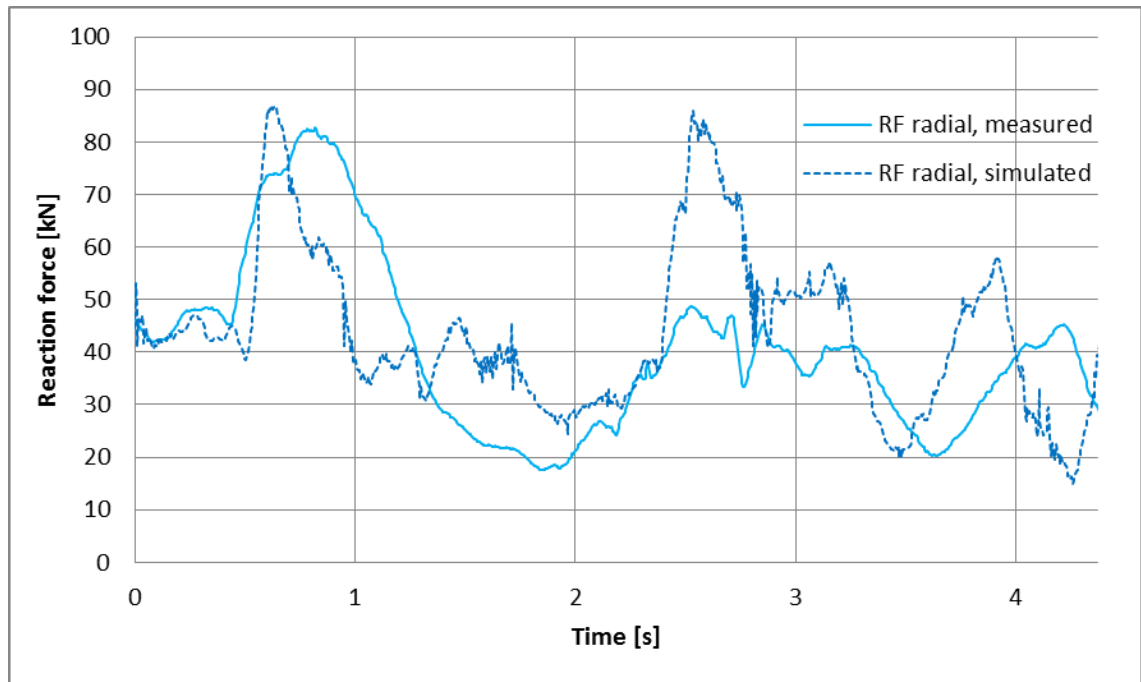


Chart 5.6. *RF tire radial reactions. Simulated radial peak force of RF tire hitting bump no. 1 is 5 % larger than the measured one.*

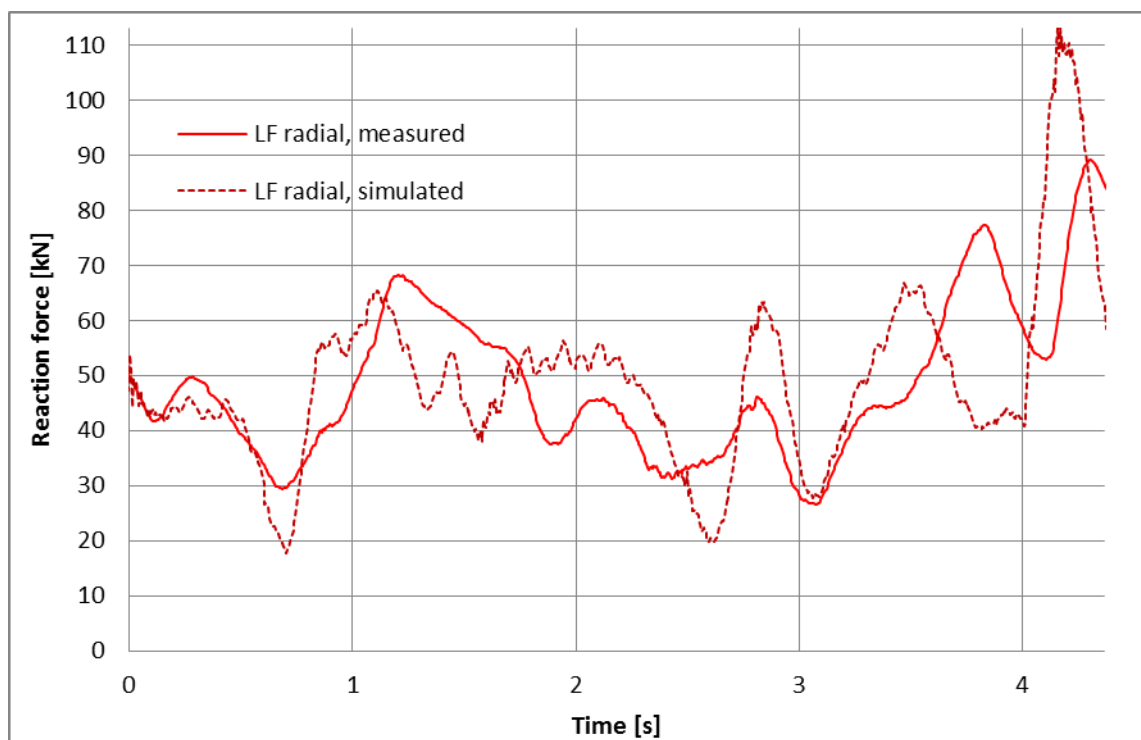


Chart 5.7. *LF tire radial reactions. Simulated radial peak force of LF tire hitting bump no. 2 is 27 % larger than the measured one.*

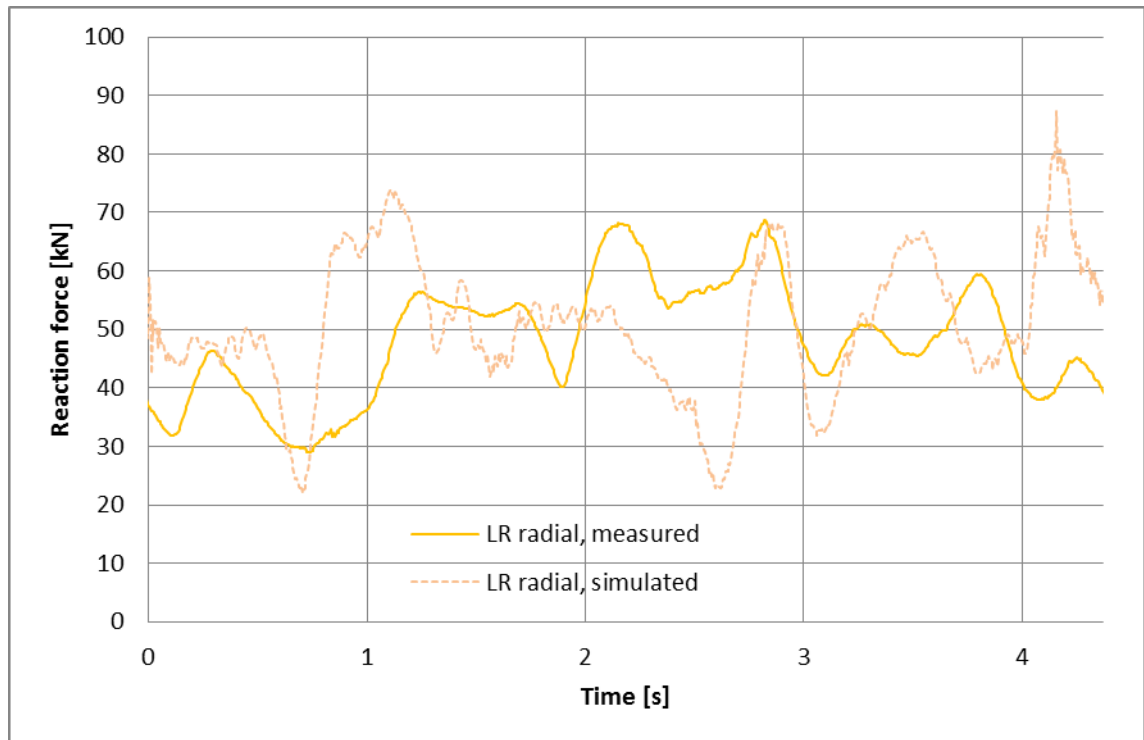


Chart 5.8. LR tire radial reactions.

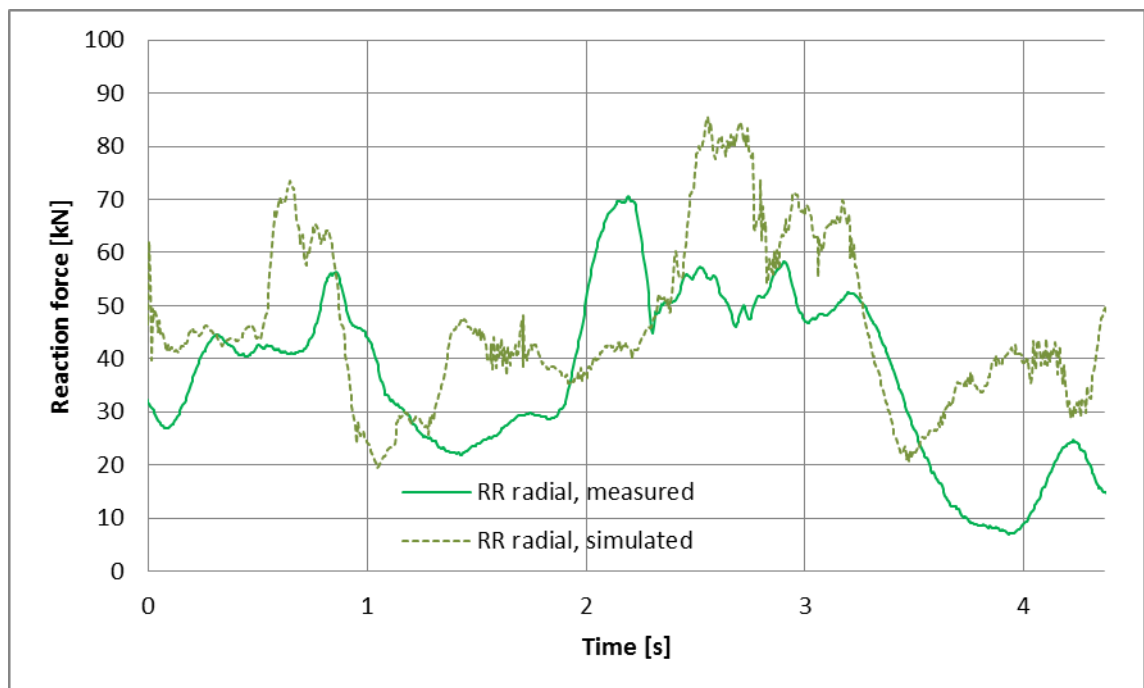


Chart 5.9. RR tire radial reactions.

5.1.2 9 ton

The observations for radial tire forces shown in Charts 5.10-5.13 are similar to the ones that are already discussed in the previous section. However, the difference between force peaks at $t \approx 2.7$ s is smaller in this load case than it was for 12 ton load case. The

magnitude of the force peak caused by LF tire hitting bump no. 2 is underestimated by the simulation model (see Chart 5.11). It is interesting to note that this peak was overestimated for 12 ton load case (Chart 5.7). This might imply that there is some deviation in the measurement process.

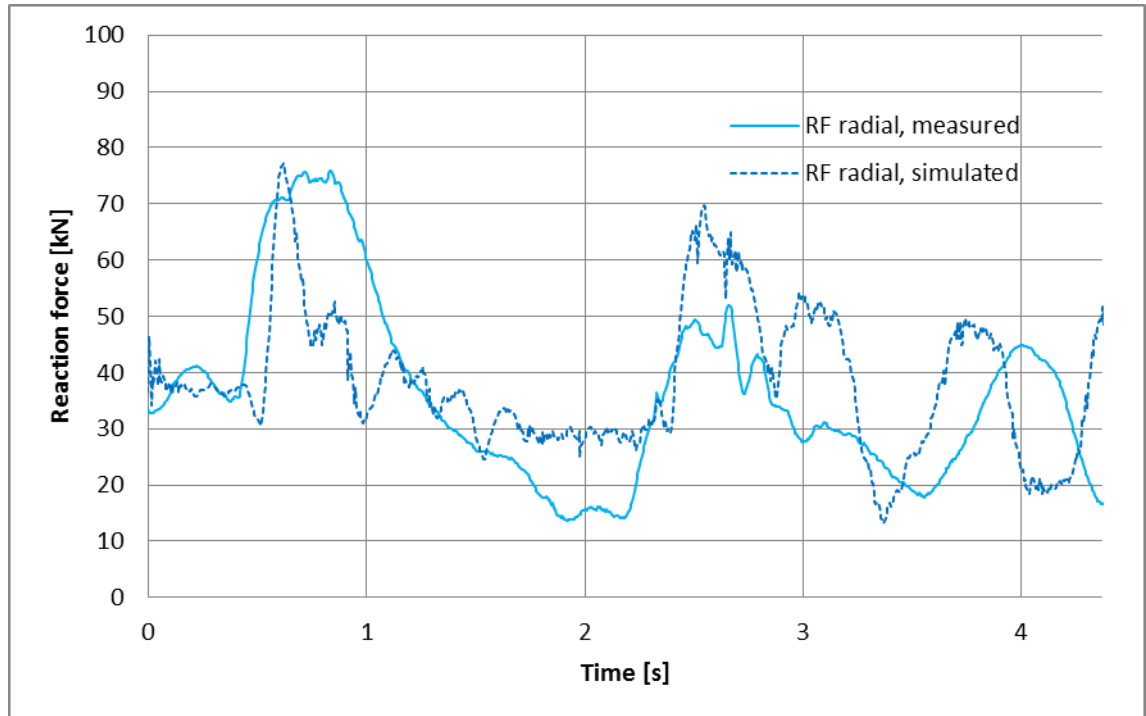


Chart 5.10. RF tire radial reactions, 9 ton load.

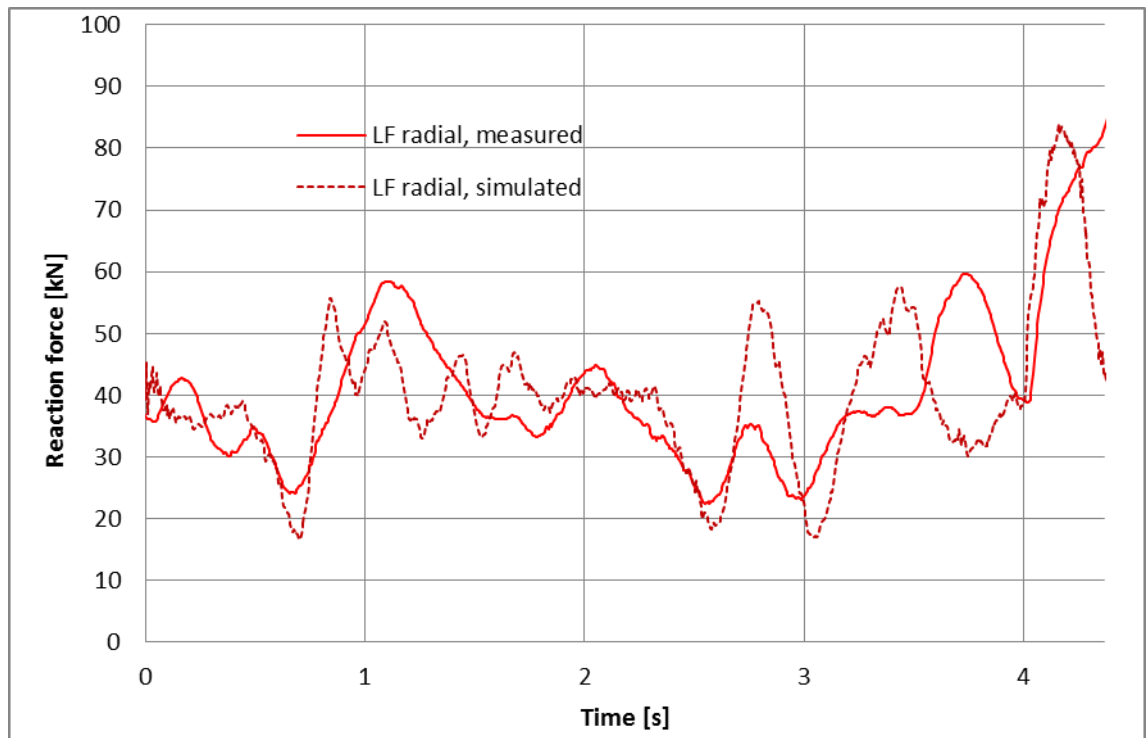


Chart 5.11. LF tire radial reactions, 9 ton load.

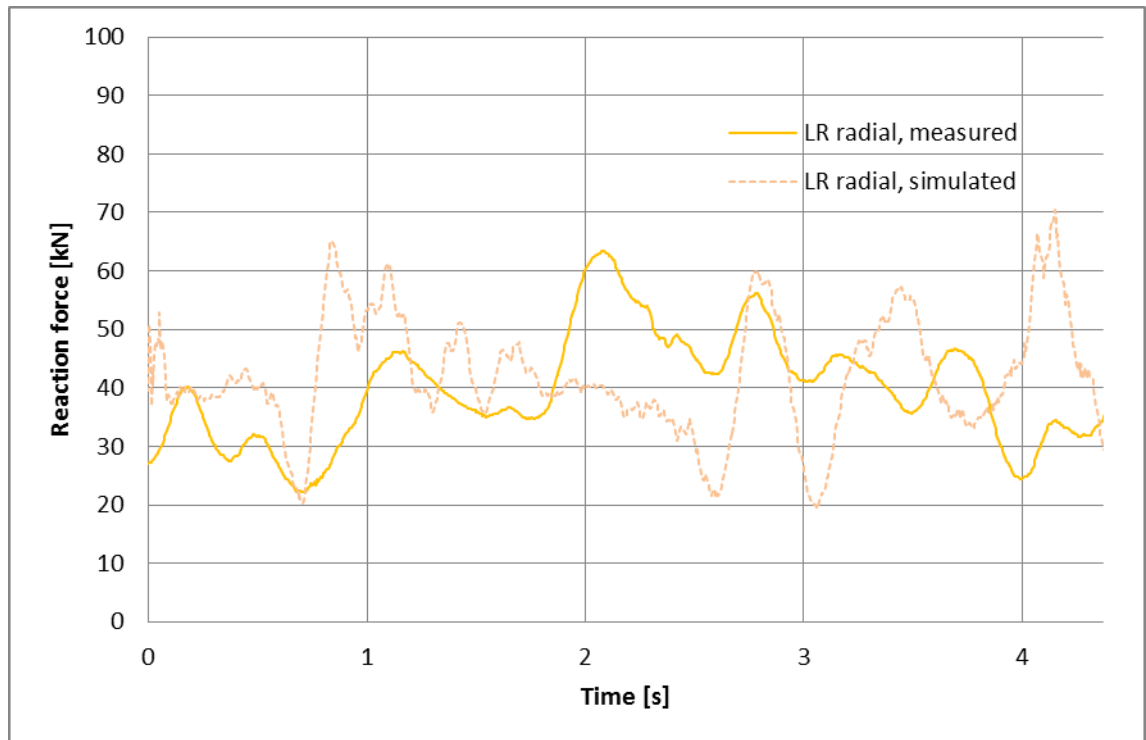


Chart 5.12. LR tire radial reactions, 9 ton load.

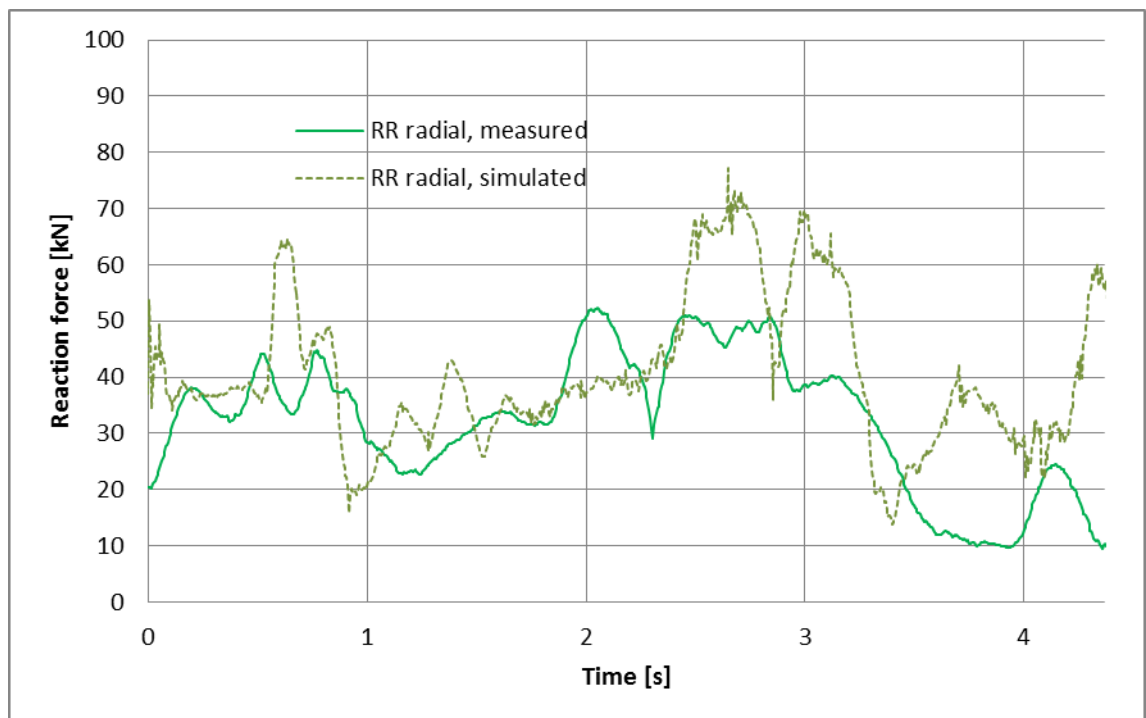


Chart 5.13. RR tire radial reactions, 9 ton load.

5.1.3 Unloaded

As was already noted in page 57 (see footnote) and Chart 5.1, the measured radial forces are smaller than expected at times before and after impacts (see Charts 5.14-5.17).

The simulation results show restless oscillatory behavior, which can be interpreted as bouncing of the rear frame because there is no cargo to damp these motions.

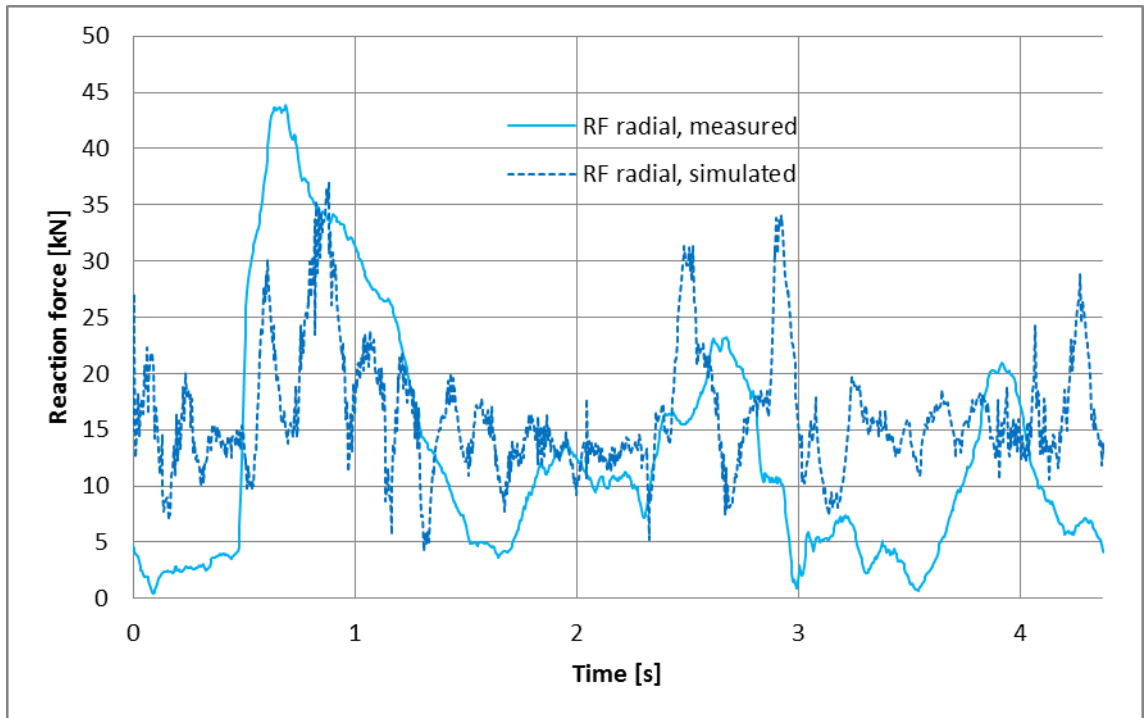


Chart 5.14. RF tire radial reactions, unloaded case.

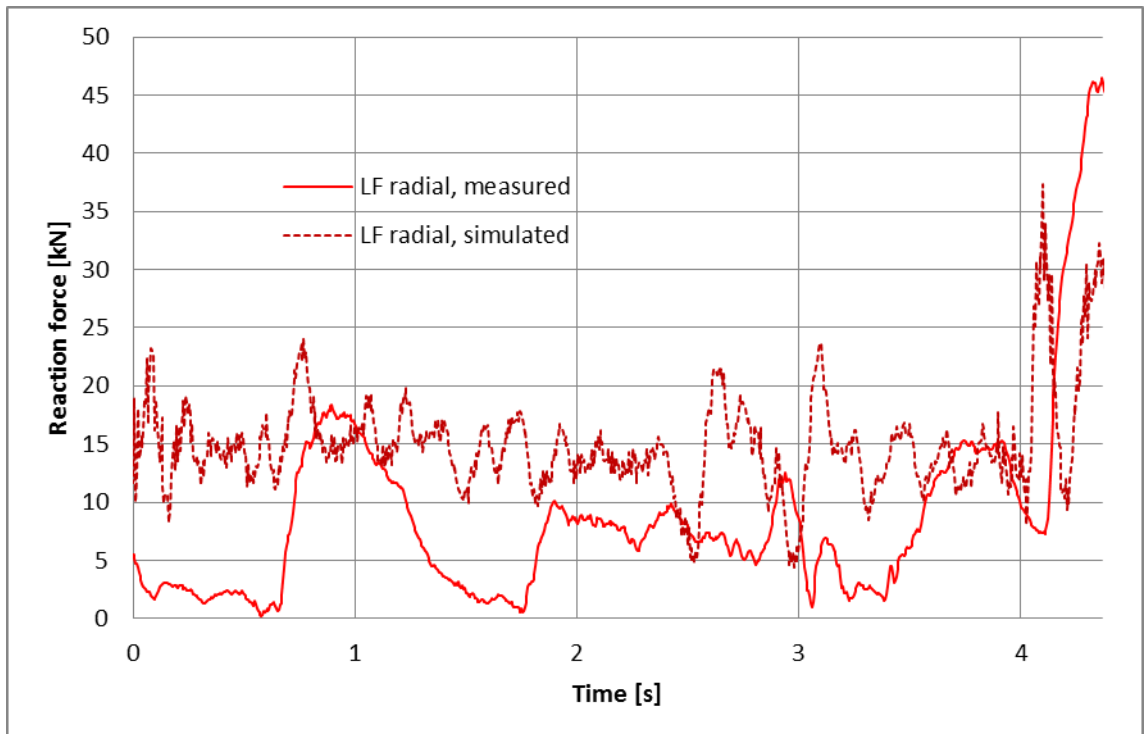


Chart 5.15. LF tire radial reactions, unloaded case.

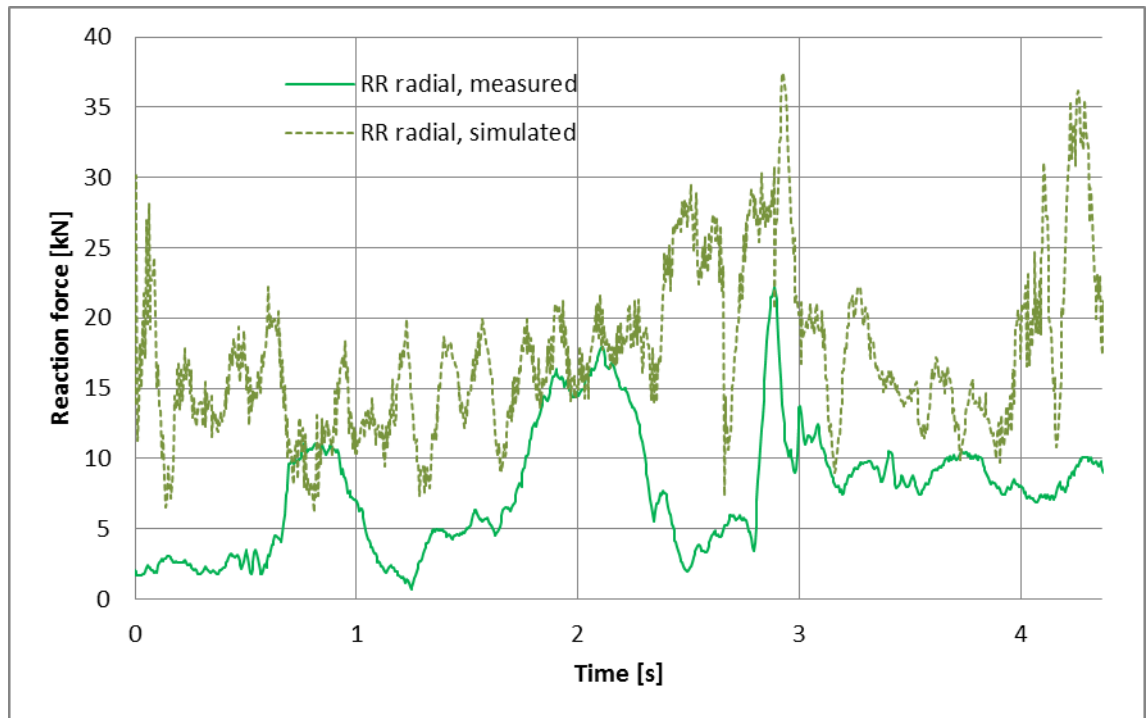


Chart 5.16. RR tire radial reactions, unloaded case.

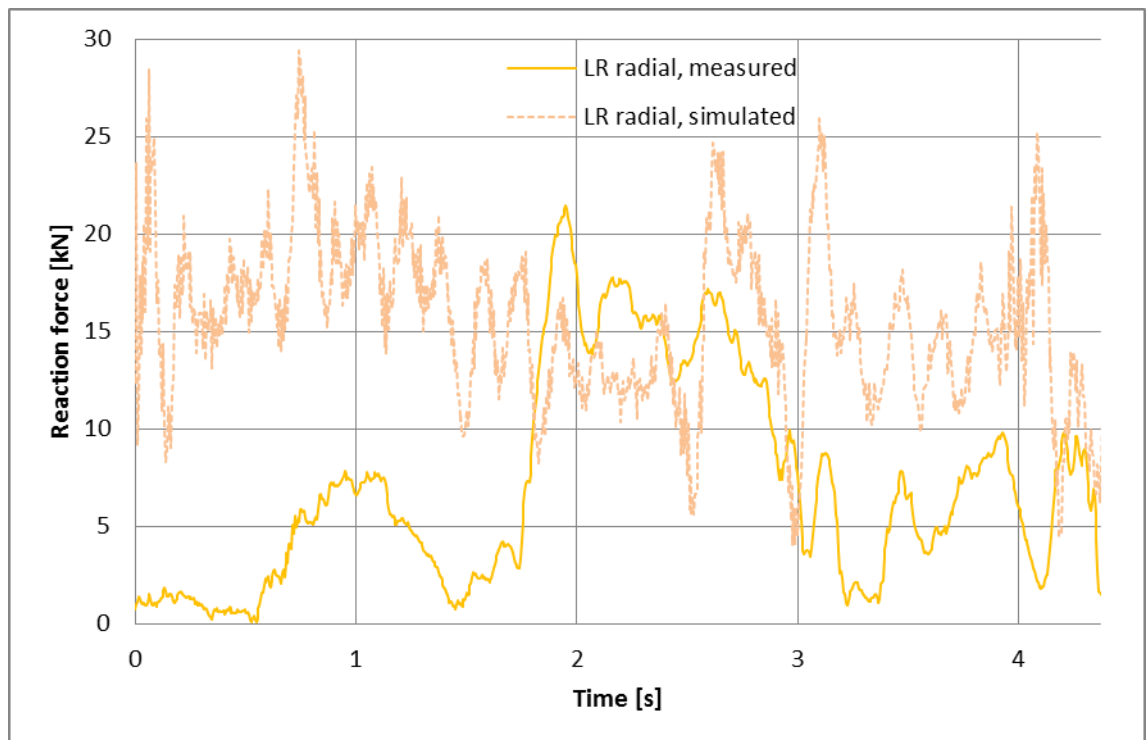


Chart 5.17. LR tire radial reactions, unloaded case.

5.2 Global stress state

Global stress levels are viewed for the load space and rear frame (12 ton load case). As both of these parts are modeled using shell elements, the resulting stresses do not account for local stress concentrations in connections of joint plates.

Chart 5.18 shows the time history of maximum von Mises stresses for the rear frame. It can be seen that most of the highest stresses are caused by forces due to weight of the cargo. Stress peak is reached just before applying initial velocity ($t \approx -0.05$ s, see Figure 4.24). The high damping at this phase however dissipates some of the energy and the maximum stress decreases to a “quasi-static” state (0.15 s $<$ t $<$ 0.45 s) as the machine rear frame is moving on a flat surface. Just before the first impact (rear frame RF tire to bump 1, see Chart 3.2 and Figure 3.1) the stress level plunges^P and rises again at impact ($t \approx 0.7$ s). The stress states of these two points (illustrated in Chart 5.18) are shown in Figure 5.2. The most critical areas are the load space mounting points and the vicinity of the rear axle.

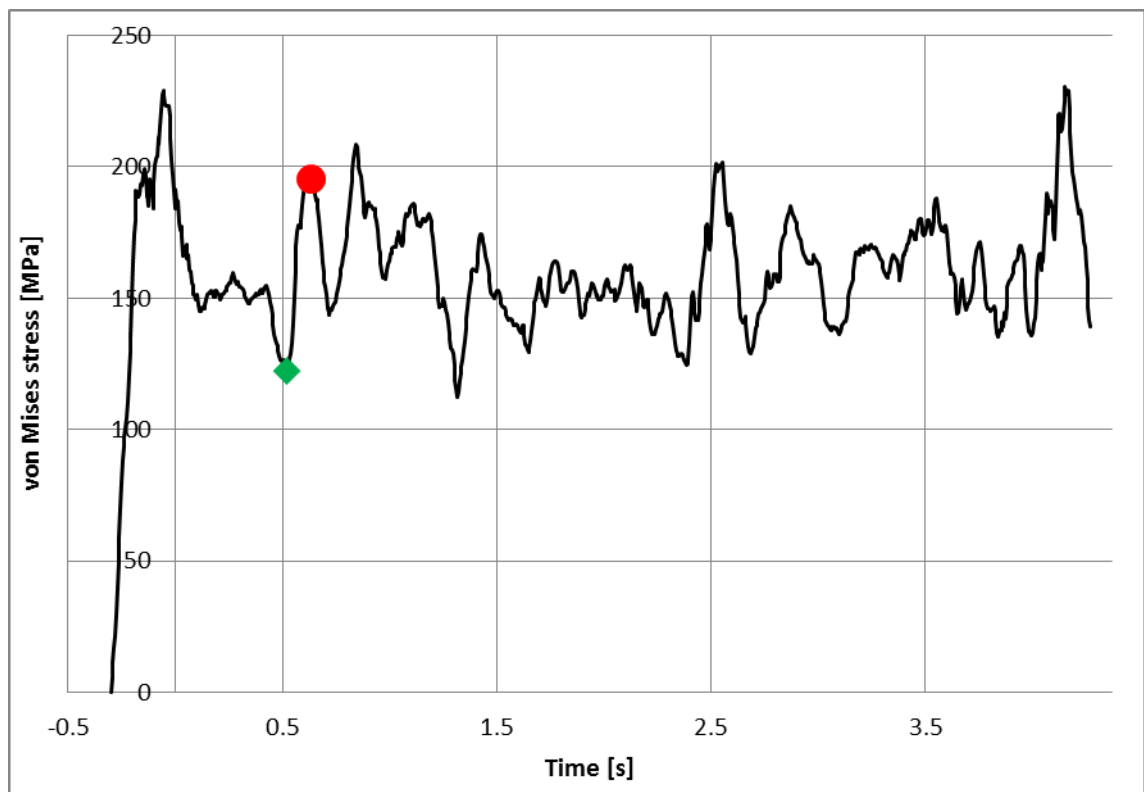


Chart 5.18. Maximum von Mises stress time history of the rear frame.

^P This might be due to forces exerted from the front frame; RF tire of front frame hits bump no. 3 at approximately $t \approx 0.5$ s

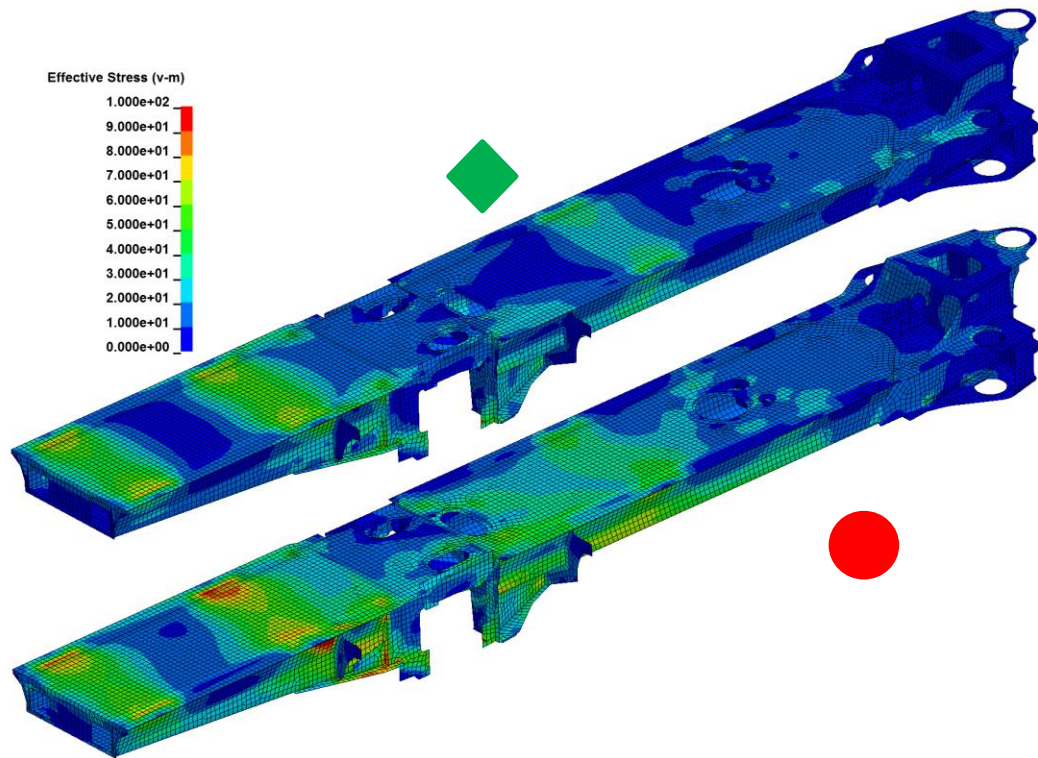


Figure 5.2. Von Mises stresses of the rear frame before first impact and at the impact (see Chart 5.18 for notation).

The load space is stressed most by the cargo as can be seen from Chart 5.19. Stress level rapidly increases after applying gravity. After peaking at $t \approx -0.1$ s (see Figure 5.3), damping forces slowly decrease the stress level. The forces exerted to the load space during the drive across the test track merely induce some minor oscillations to the stress field caused by the cargo ($t > 0.7$ s). Based on this, it can be inferred that (at least at high loads) the stresses at load space are dominated by the cargo and not much affected by the dynamic tire forces. The stresses are highest at the rearmost posts. This is likely to be caused by the location of the grapple (grapple weight is ~ 500 kg, see Figure 4.3) and more robust structure of the components located at the front section of the load space.

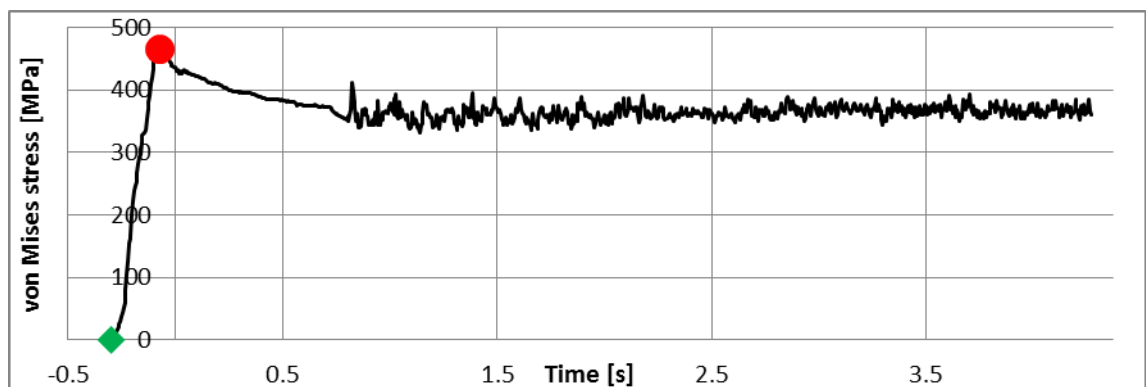


Chart 5.19. Von Mises stress time history of the load space.

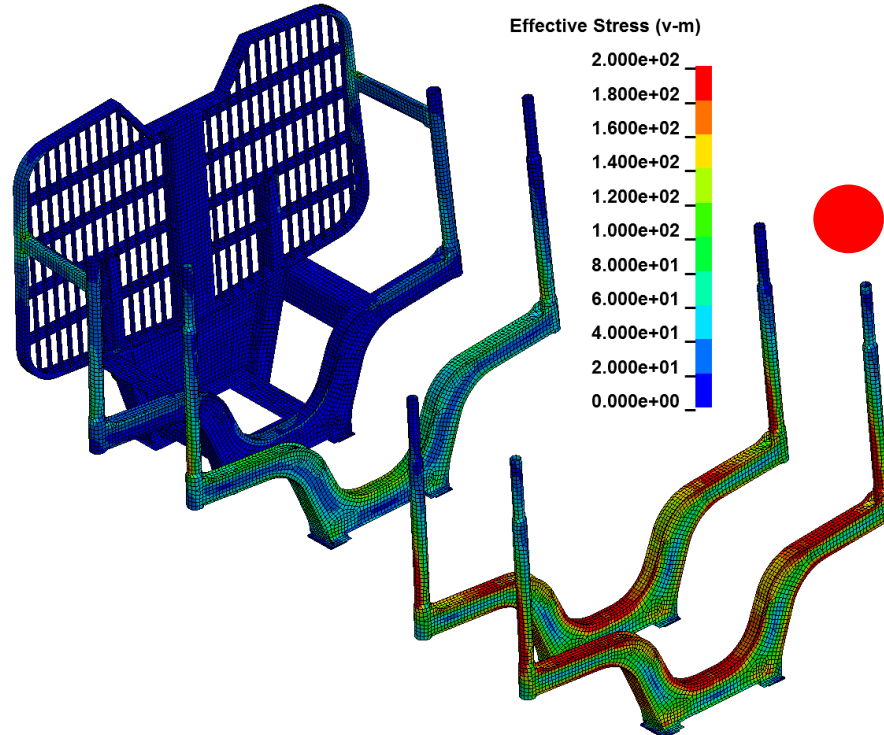


Figure 5.3. Von Mises stresses due to log-load space interactions after applying gravity. See Section 5.3 for more information on forces acting on load space.

5.3 Deformations

The deformation results are not very interesting in this simulation. The only reported results are the load space lateral (Figures 5.4 and 5.5) and vertical (Figure 5.6) deflections produced by cargo.

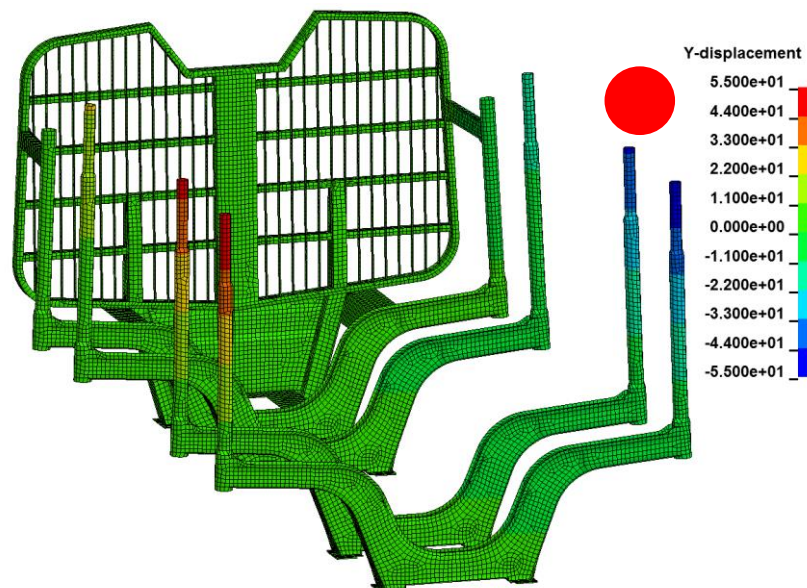


Figure 5.4. The rearmost posts bend approximately 55 mm (laterally) due to forces generated by the logs and the grapple.

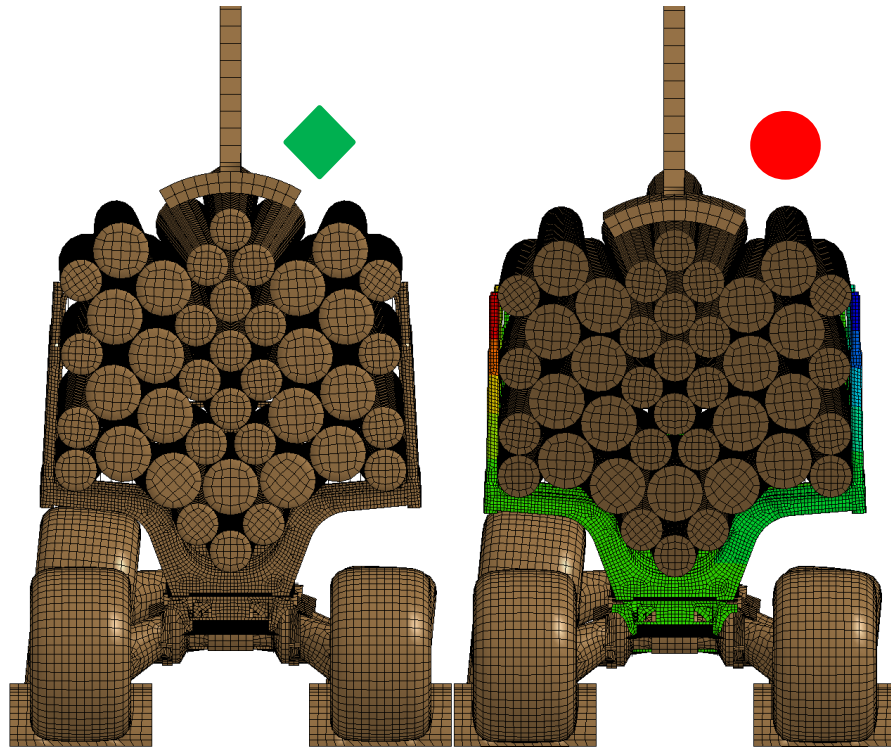


Figure 5.5. Deformations viewed from another angle. Initial state (see Chart 5.19 for notation) shown on left and deformed state, after applying gravity, shown on right.

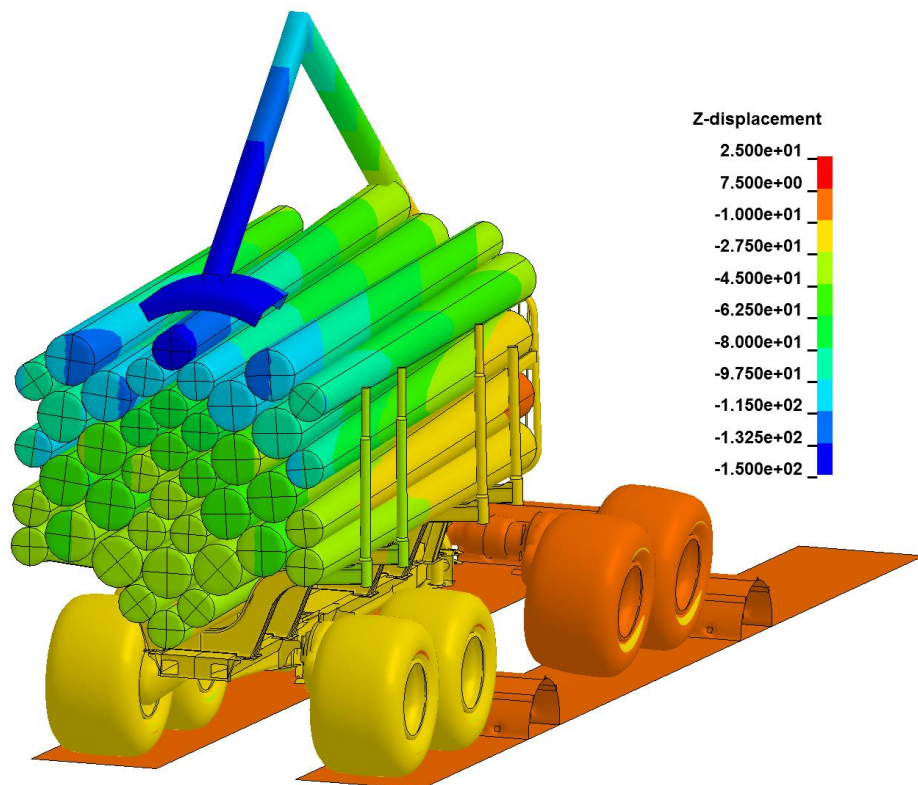


Figure 5.6. Vertical deflections at $t=0$ s. Rear frame vertical movement is higher as the mass of the rear frame is higher than that of the front frame.

5.4 Solution accuracy

Major aspects affecting the accuracy of the solution are presented in the following sections.

5.4.1 Energy conservation

The accuracy of the solution based on energy balance of Equation (58) is evaluated in this section. Chart 5.20 shows energies as a percentage of system total energy (sum of terms in the left side of the equation). When interpreting the chart, it must be noted that the total energy varies with time.

The external work at $t < 0$ s is caused by tire pressurization. After velocity initialization the torque rotating the tires becomes the main source of external work. As tire instabilities (Section 4.9.3) progress, the tire internal pressure once again starts to play a role in the magnitude of the external work. As the tires of the rear frame climb over the bumps, the rear frame CoG rises to higher gravity potential; this is shown as a rise in external work.

Some kinetic energy is present at the beginning of the simulation (damping phase, -0.3 s $< t < -0.1$ s). This is caused by vertical deflections (see Figure 5.6). Kinetic energy then increases due to applied velocities and plunges when RF tire hits bump no. 1. Kinetic energy seems to slowly decrease during the simulation, but this is not the case since the total energy of the system rises as simulation progresses (therefore the absolute value of kinetic energy remains nearly constant even though its fraction of total energy decreases).

Prior to applying initial velocities (at $t = 0$ s), the major contributor in the total energy of the system is the tire internal energy caused by pressurization. Internal energies due to strains at other parts also contribute to this. Internal energy increases as the machine hits bump no. 1. As all parts behave in an elastic manner, internal energies are released after the collision.

The hourglass energy remains at approximately 5 % of total energy throughout the simulation, which is an acceptable value as was stated in page 25, Section 2.8.

Damping energies (Sections 2.6, 4.3 and 4.9.3) are small throughout the simulation compared to system total energy.

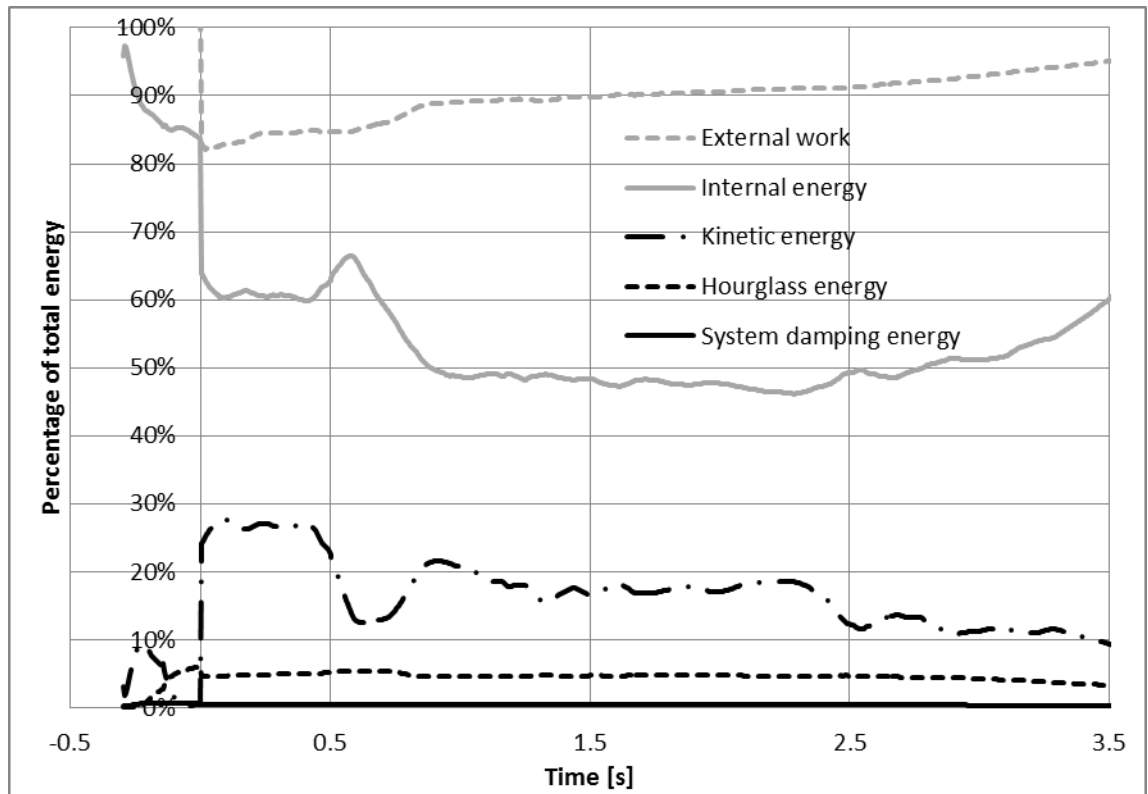


Chart 5.20. Different forms of energies as fractions of total energy throughout the simulation.

The energy ratio is obtained by dividing the left side of Equation (58) with the right side. This ratio, shown in Chart 5.21, should be close to unity ensure solution accuracy. LS-DYNA does not, by default, include hourglass energy to this ratio as it is artificial [23]. Most of the deviation from unity is explained by neglected hourglass energies in calculating the ratio. After the tire instabilities start to take control, the energy ratio starts to rise at a very fast pace.

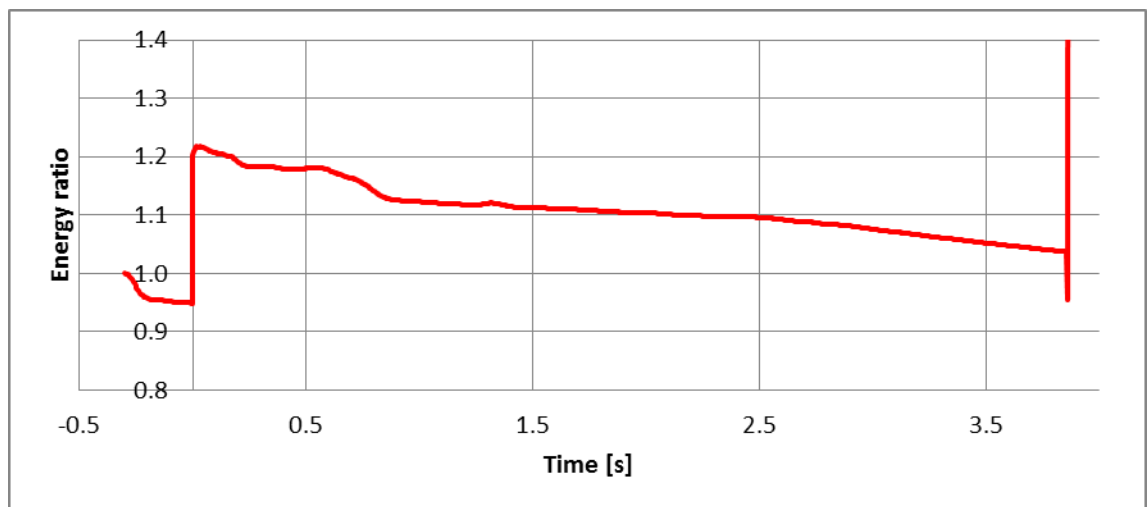


Chart 5.21. Energy ratio.

5.4.2 Floating point number accuracy

LS-DYNA® can solve the model using either single or double precision accuracy in handling floating numbers. It is not always known beforehand which precision should be used. Double precision is suggested for analyses with long duration (=large number of time steps) where single precision might lead to cumulative error [42]. It was found that the use of double precision resulted as a 25 % longer solution time compared to single precision. As the resulting difference between these methods is small (see Chart 5.22), single precision will be used.

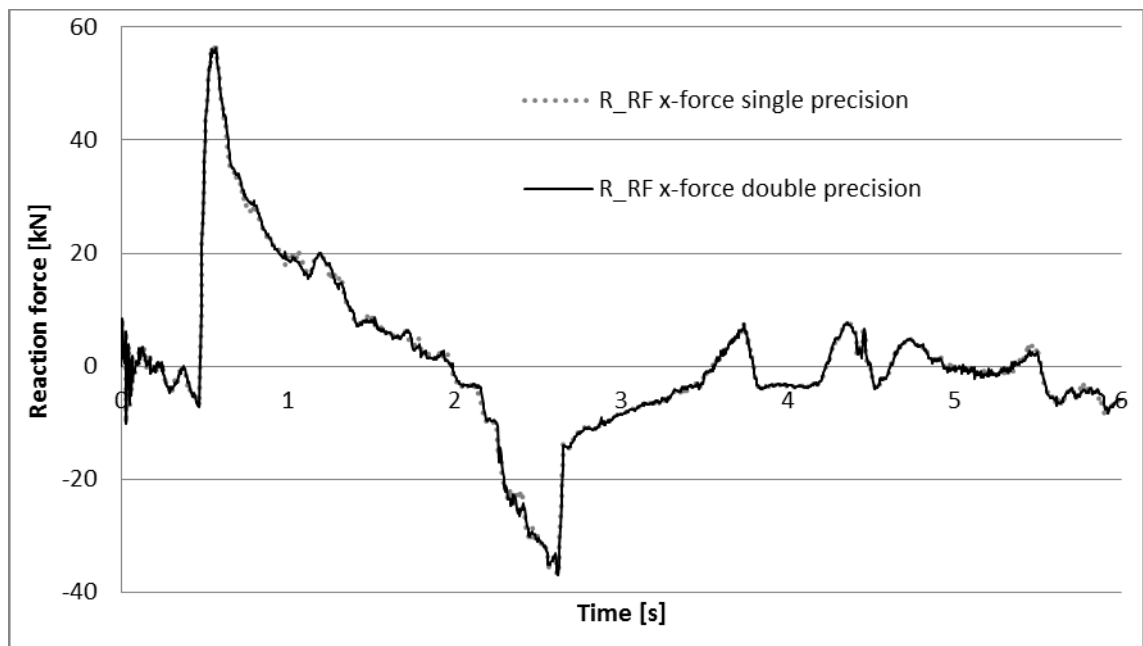


Chart 5.22. Comparative results of horizontal force on the right front tire of rear frame for single and double precision solutions. Note that these results are from a model used early in the simulation process. The results of this chart therefore differ from results presented in Section 5.1.

5.4.3 Mass scaling

The global amount of mass scaling (see Section 2.4.3) needed to satisfy the requirements of the desired CFL step (see Equation (8) and Table 4.2) is shown in Chart 5.23. Mass scaling remains low at $t < 3.5$ s, but starts to rapidly grow after this due to mass scaling required in tire sidewalls (increasing tension caused by instabilities in sidewalls decreases the CFL time step, see Section 4.9.3).

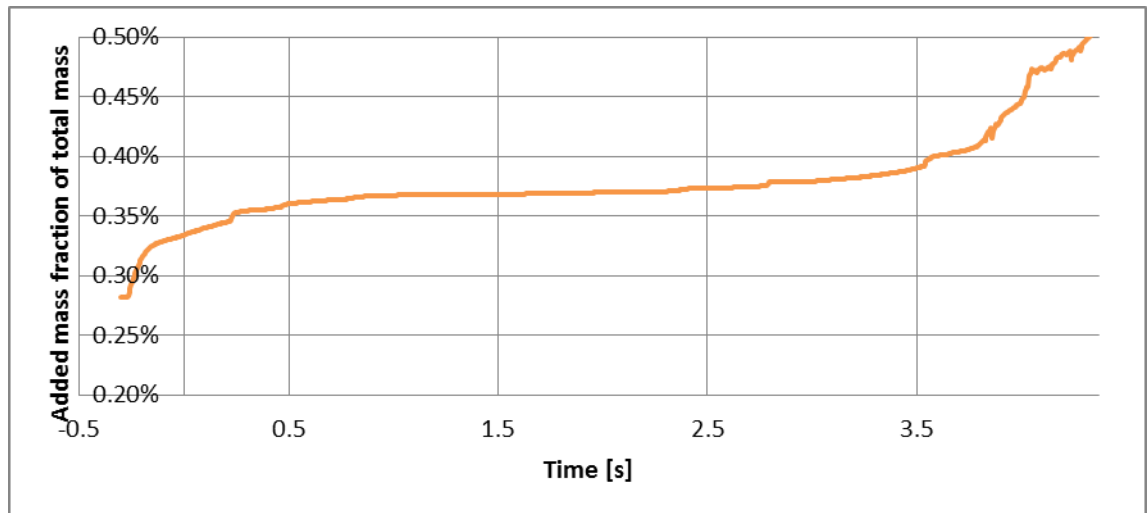


Chart 5.23. Added mass as a percentage of total mass.

The scaled elements are shown in Figure 5.7. Scaling is highest in triangular “filler” elements and in ill shaped quadrilateral elements.

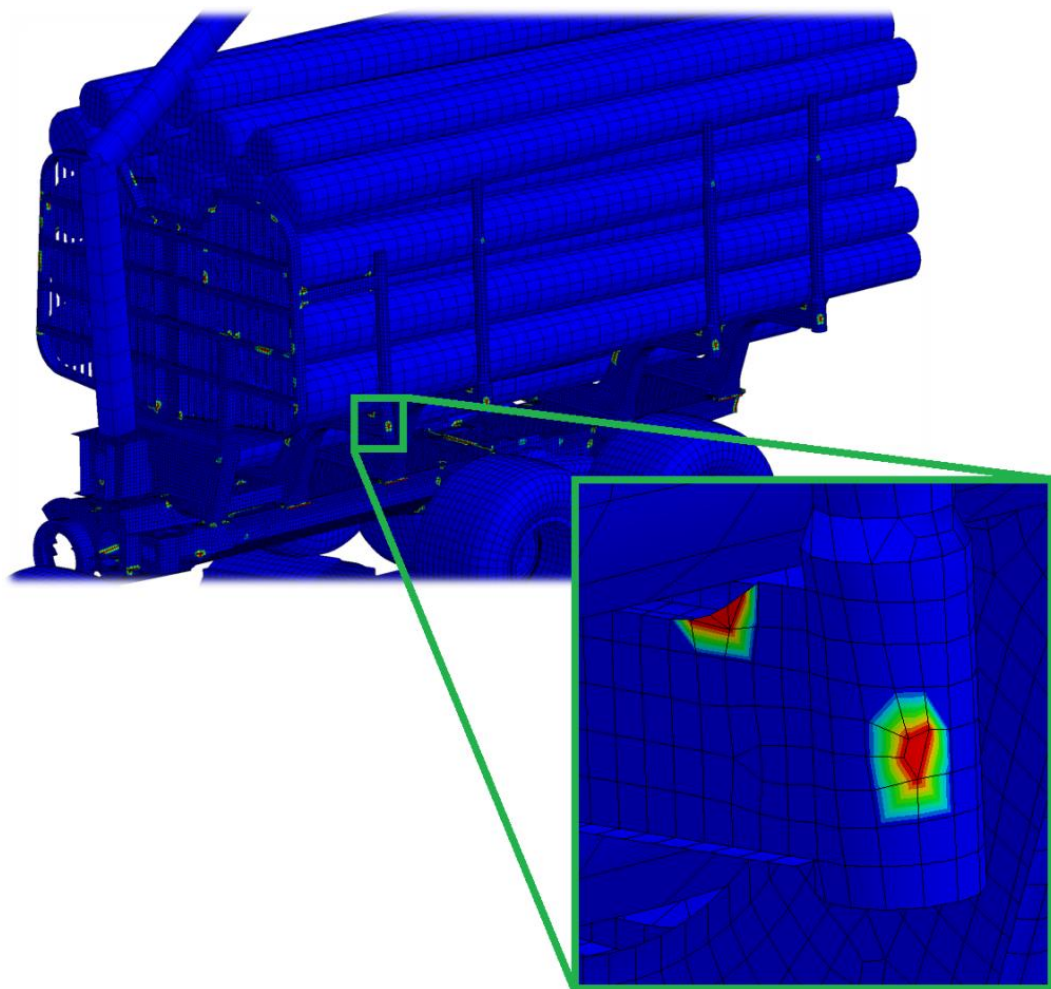


Figure 5.7. Elements with mass scaling (zero in blue elements and maximum in red elements).

5.4.4 Tire friction

As was stated earlier in Sections 4.9.7 and 5.1, the magnitudes of the friction coefficients acting in the contact between tire and ground affect the results. Therefore a sensitivity study is conducted using different friction coefficients (see Equations (13) and (71)) as shown in Table 5.1.

Table 5.1. *Studied friction coefficient combinations and resulting force peaks (12 ton load case) in kN. Combination 6-4 is used in the simulation model.*

Combination	μ_s	μ_d	RF to bump no. 1	Compared to measured value	LF to bump no. 2	Compared to measured value
8-5	0.8	0.5	84.7	+2 %	103.6	+16 %
6-4	0.6	0.4	86.9	+5 %	113.2	+27 %
4-3	0.4	0.3	94.2	+14 %	114.6	+29 %
2-2	0.2	0.2	105.2	+27 %	115.9	+30 %

The effects of the friction coefficients to RF tire radial forces (in 12 ton load case) are shown in Chart 5.24 (Curve marked “6-4” corresponds to simulated values of Chart 5.6). Similarly, results for LF tire are shown in Chart 5.25. The force peaks of RF and LF tire hitting bumps no. 1 and 2, respectively, are also listed in Table 5.1 with comparison to measured values (measured values from Charts 5.6 and 5.7).

The force peaks seem to increase in magnitude as coefficients of friction get smaller. This is likely to be caused by the decrease in “braking” (friction) forces of other tires as the tire hits the bump. The tires have (as discussed earlier in Section 4.9) coarse treads which might, in conjunction with the “grip plates” (L-beams welded to bumps, shown in figures of Sections 3.2 and 4.3) dramatically increase the grip force of the tire as it crosses the bump. The tire model used in the simulation does not have treads modeled, which might partly explain the overshoots of simulated force peaks.

Force peaks (after bump no. 1) are also “delayed” in smaller friction values. This is caused by slipping tires; the friction forces are not large enough to allow for the tire contacts to have a relative velocity equal to zero (thus $\mathbf{u}_f \neq 0$ in Equation (71)).

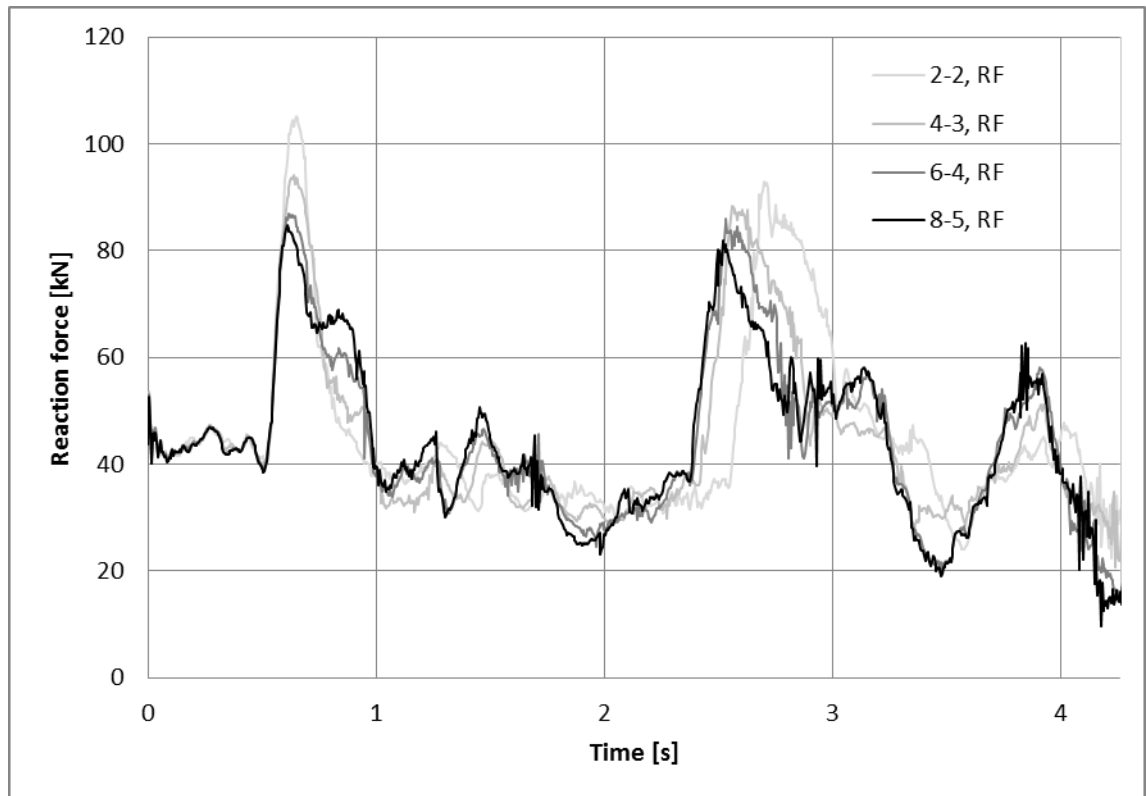


Chart 5.24. Comparison of effect of different friction coefficient combinations of Table 5.1 to RF radial tire forces.

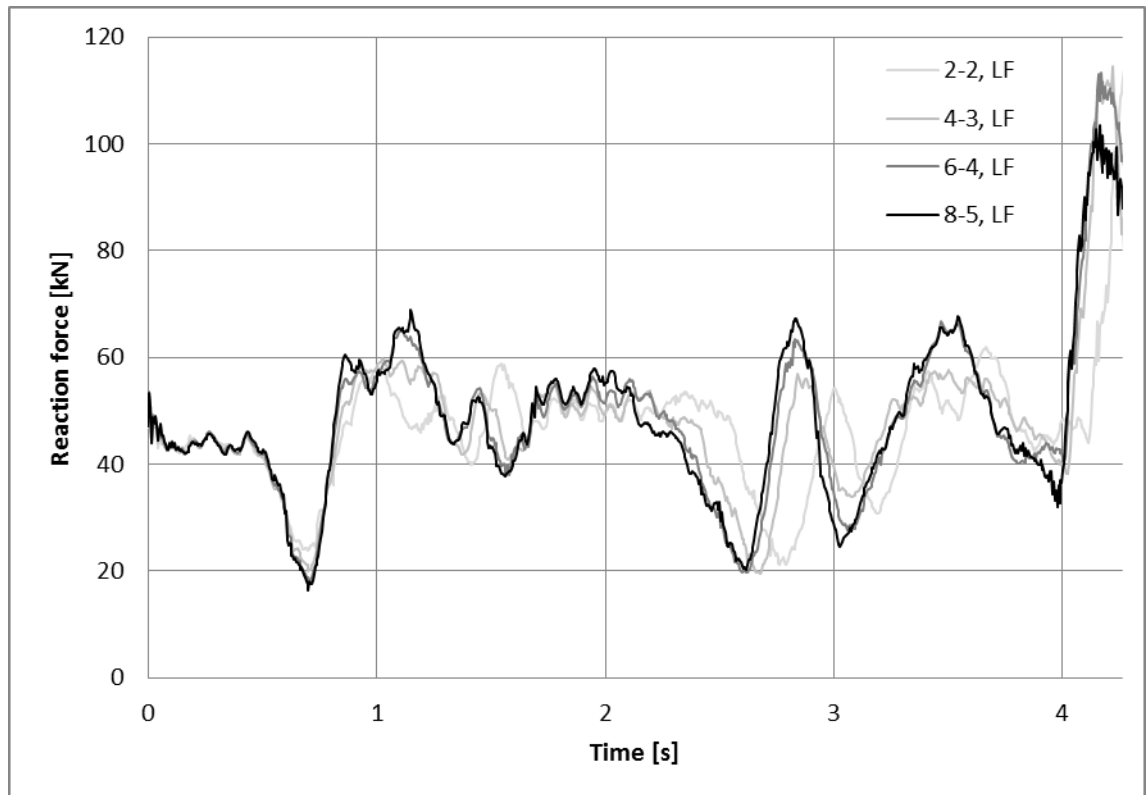


Chart 5.25. Comparison of effect of different friction coefficient combinations of Table 5.1 to LF radial tire forces.

5.5 Computing time

The computing time required to simulate the 12 ton load case (duration 5 seconds) was approximately 10 hours using *MPP* (*Massively Parallel Processing*) LS-DYNA with 20 processor cores at 2.8 GHz. Other load cases were cheaper to compute.

6. SUGGESTED FURTHER WORK

Some ideas for further development and use for the model introduced in this work are presented in the following sections.

6.1 Cargo loading

The forces caused by loading of the logs (e.g. log drop to load space or collision to load space posts) can be analyzed using a model similar to the one presented in this report.

6.2 Collision simulation

Some issues with the durability of underframe hatches and shields have been observed in the past [26]. Results from simulating these hatches/shields with a model similar to the one used in this report can be used for optimizing the design of them. Realistic conditions can be simulated by colliding the entire machine with an obstacle hitting the shield, e.g. a stone or a tree stump (the modeling of rocks with *Discrete Element Method* (DEM)/FEM has been studied by Larsson [38]). A material model capable of simulating plasticity (such as *multilinear isotropic hardening* or *multilinear kinematic hardening* for cyclic plasticity) must be used in the frame and hatches in this kind of simulation since stresses above the yield limit are expected. In addition to hatches/shields, this type of simulation can also be used for determining dozer blade or bumper loads in collision (or when turning the machine against an obstacle).

6.3 Implicit dynamic fatigue model

The reaction force/moment history from the explicit dynamic simulation results can be used as input for a *mode superposition linear implicit dynamics* model. The reactions transmitting from the bogie, the middle joint and the load space must be included in order to study the rear frame using this method. The implicit model can also be modeled using shell elements. Due to mode superposition and linearity this model is computationally relatively inexpensive (when compared to implicit transient *non-linear* solution with *full method*). [7]

It is important to calculate this model using a *dynamic* solver rather than a *static* solver. For impulse loadings (*step load* or *square impulse*) with a duration much shorter than the eigenfrequency of interest the resulting stress state will be lower than that of the static solution, i.e. the results of static analysis are *over-conservative*. Systems with

damping lower than critical damping and long duration impulse loadings (duration equal to or longer when compared to the duration of eigenfrequency) will respond with a stress state that is higher than the static solution, i.e. the static solution becomes *un-conservative*.

The results of the static analysis are erroneous due to the neglected inertial effects (in static analysis Equation (1) is in a form that does not include time derivatives of displacement vector, only internal and external force vectors). A static solver should only be used if the loading is applied slowly enough (*ramped loading* with ramp time equal to or higher than the eigenfrequency duration), i.e. when the solution becomes *quasi-static* (inertial effects are negligible even though the loading is transient).

After solving the implicit model, the deformations (deformation based sub-modeling, “*cut-boundary displacement method*”, is implemented in ANSYS® [6], but some other codes use force based sub-modeling) of the region of interest can be interpolated to boundaries of an *effective notch stress method* [27] *sub-model* constructed with solid elements. Inertial effects on the localized sub-model should be negligible and therefore the use of a static solver should be acceptable (this needs to be verified).

6.4 Other machines

One of the goals of this work was to study the ability of the simulation model to predict forces acting on the machine. As results are reasonable, the construction of computational models for larger forwarders (and possibly harvesters) would be profitable. The modeling effort required for simulating other machines is greatly reduced when compared to the machine simulated in this report since suitable methods have now been developed.

6.5 Power train

A more sophisticated (compared to method described in Section 4.1) method for transmitting torque to wheels, explained in following sections, was also tested. Due to accuracy, stability and software issues these features were not however implemented in the final simulation model. By fine tuning these methods, they might be used in future models.

6.5.1 Differential

The movement of the forwarder during the simulation is done by adding a constant rotational velocity to each joint between the rims and the bogie hubs (see Section 4.1). This can be interpreted as a 100 % locking differential which is not exactly the case in the physical machine, as the bogie does not have a locking differential and therefore the tires on the left can rotate at a different speed compared to the right side. Both tires on

one side (LF and LR tires have equal velocity, RF and RR tires have equal velocity) of the bogie are forced to rotate at an equal speed since they are mechanically connected via gears. The forwarder has a central differential lock that fixes the relative speed of the front and rear frame bogie power intakes. The tires going over the test track bump (see figures in Section 3.2) travel a distance 16 % longer compared to the tires on the other side that travel on a planar surface. A traditional differential gear allowing a difference in the rotational velocity provides an equal torque to each wheel pair (left and right) [51]. A differential gear shown in Figure 6.1 is modeled to achieve these properties.

The ring gear is connected to the planet gear via *gear joint* (LS-DYNA® keyword `*CONSTRAINED_JOINT_GEAR` [44]), as are both sun gears to planet gear. Both of the sun gears transmit the rotation to rear axle wheels through pulley joints (LS-DYNA® keyword `*CONSTRAINED_JOINT_PULLEY` [44]). Input file for the differential can be found from Appendix D.

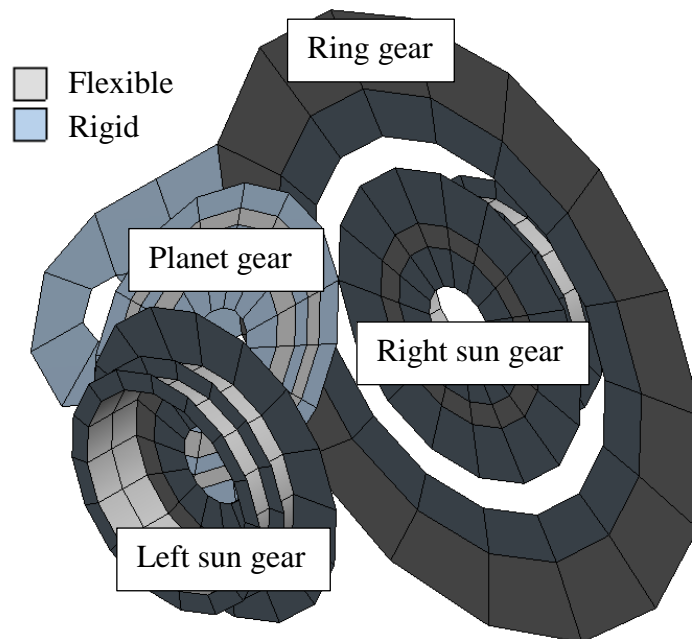


Figure 6.1. *Components of differential gear.*

It was observed that some numerical instability emerged when using multiple joint definitions for a single rigid body. Therefore a flexible body (see Figure 6.1) was added between each connecting rigid body. It was also found that the default joint formulation (LS-DYNA® card `*CONTROL_RIGID` variable `LMF=0`, explicit penalty formulation [44]) was incapable of modeling the joints of differential gear (non-physical behavior observed during simulation). To fix this, `LMF=1` (Implicit formulation with Lagrange multipliers) was used instead [10].

This method was not used since the gears would start traveling out of their intended paths after experiencing a certain level of rigid rotation. It is estimated that this is a numerical accuracy issue.

6.5.2 Torque limiter

As the machine is driven in altering terrain and a constant rotational velocity, ω , is defined for the differential, the required torque varies with respect to time.

It was found that the torque required for keeping up ω includes some peaks higher than the maximum torque output of the machine. If the torque is exceeded more than it was in this analysis, it might result as unrealistic force peaks monitored on the tires. To address this problem, a torque limiter could be added to the differential using *SENSOR keywords [44]. A visual flowchart of this ideal sequence is shown in Figure 6.2.

First, the torque input to the differential by ω (see Section 6.5.1) would be monitored via *SENSOR_DEFINE_FORCE. If the torque exceeds the limit defined by *SENSOR_SWITCH, *SENSOR_CONTROL disables ω . After disabling ω , another *SENSOR_CONTROL would turn on the constant torque and the resulting ω would be monitored (possibly via *SENSOR_DEFINE_NODE). When ω exceeds the originally defined constant value, control is again switched from constant torque to constant ω . This sequence would keep both ω and torque within the limits set. [45]

The ideal sequence described above could not be used since *SENSOR keywords do not support using the keyword *LOAD_RIGID_BODY, which would be used in defining the constant torque for the differential. Instead, a draft for torque limiter (tested in R7.1.1) shutting down ω for a defined time (TIMWIN) after torque is exceeded is presented in Appendix E

The reason for not using the limiter (neither of the forms described above) was a software bug found on LS-DYNA® version R8.0.0 that results as an error when attempting to use *SENSOR keywords in conjunction with *CONSTRAINED_JOINT keywords [39]. LS-DYNA® version R7.1.1 could not be used since it does not support NREP (NREP enables looping of the specified sensor) within keyword *SENSOR_CONTROL.

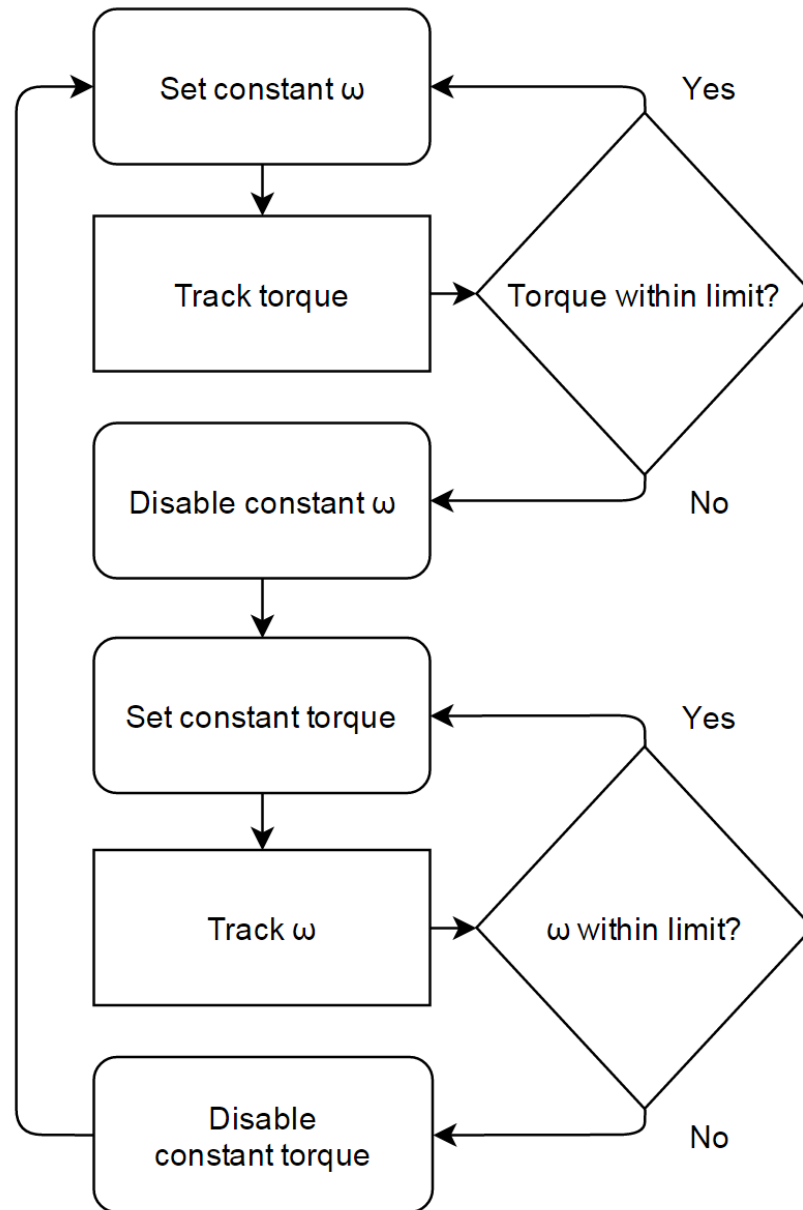


Figure 6.2. Flowchart clarifying the ideal torque limiter.

6.6 Special terrains

Softer terrains, such as snow, mud or forest floor can be modeled using DEM. Tire and soft soil interactions using DEM have been studied earlier, for example by Li [40] and Smith *et al.* [61]. The machine can then be driven in these soft terrains and, for example, in steep hills to simulate machine rollovers. Rollover (ROPS) and falling object (FOPS) test are required for forestry machine cabins. The properties of these protective systems can be computed in different scenarios using explicit dynamics model (element failure is easier to model in explicit dynamics than it is in implicit dynamics). The laboratory tests required by corresponding ISO standards can also be simulated.

6.7 Tire model improvement

In the future, when computing power further increases, the tire model could be made more accurate by using denser mesh (for mesh-independent results) and possibly solid elements (this might remove tire stability issues; the fact that tire instabilities emerged after a rigid rotation of 180 degrees, despite all of the stabilization mechanisms used, suggests that the problem might be in shell element formulation). Tire might even be simplified to be modeled without composite structure (using isotropic material and layer properties) without significantly affecting the accuracy (or at least by using an isotropic transverse reinforcement, layer B in Figure 4.23).

The tire was attached to the rim using a bonded contact as shown in Figure 6.3. The contacting elements in the tire were found to deform abnormally when the tire was pressurized. This was probably due to high bending moments experienced by these elements (bonded contact ties rotational DOFs in addition to translational DOFs). This deformation might be avoided by modeling the rim lip (the area in which the tire and the rim connect) with higher accuracy and using a frictional contact between the parts. This would also require modeling the reinforcement beads to the tire. The distorted elements connected to the rim via bonded contact are shown in Figure 6.4.

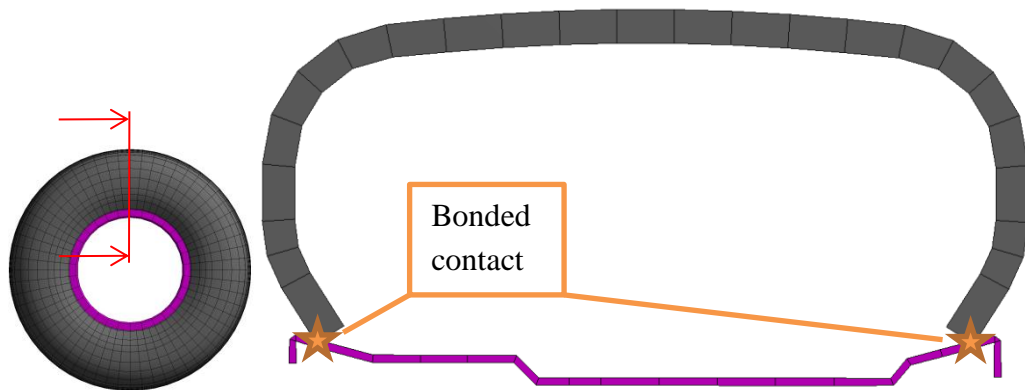


Figure 6.3. Mesh at tire cross section.

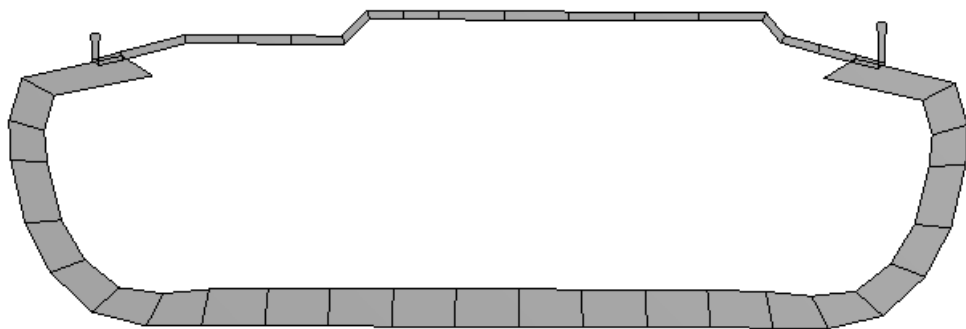


Figure 6.4. Highly distorted elements at cross section of a tire inflated to 400 kPa and compressed using a force of 100 kN.

7. SUMMARY

The goal of creating a simulation model capable of replicating the forces measured from the physical test was achieved with reasonable accuracy. The simulated tire forces correlated well with measured values with only one major deviance at ~2.7 seconds (see Section 5.1 for explanation, especially Charts 5.3 and 5.5). The correct evaluation of the largest force peaks is important since they contribute most to the fatigue life of the machine components. The measured and simulated force peak results and their comparison is shown in Table 7.1. For example, the difference between simulated and measured values of RF tire (see Figure 3.4) hitting bump no. 1 (see Figure 3.1) in 12 ton load case is approximately 5 % (shown in Chart 5.6). The RF tire forces are also evaluated with good accuracy^Q in 9 ton load case but are underestimated in unloaded case. The forces on LF tire, when hitting bump no. 2, are overestimated in 12 ton load case, but underestimated in 9 ton and unloaded cases. This might imply that there is some deviation in the measurement process since the differences are not consistent between load cases. The underestimation of both force peaks in unloaded case is most likely due to oscillatory behavior shown in results (Section 5.1.3), which in turn is estimated to be caused by coarse modeling of the boom and its contact to the load space^R.

Table 7.1. Comparison of measured and simulated radial force peaks [kN].

Load case	Force peak	Measured	Simulated	Difference
12 ton	RF to bump no. 1	83	87	+5 %
	LF to bump no. 2	89	113	+27 %
9 ton	RF to bump no. 1	76	77	+1 %
	LF to bump no. 2	91	84	-7 %
Unloaded	RF to bump no. 1	44	37	-16 %
	LF to bump no. 2	47	37	-20 %

The stiffness properties of the tires were found to be a dominant factor in the dynamic behavior of the entire machine^S. Test results for tire dynamic properties were unavailable and therefore the validity of the used tire model in terms of dynamic properties could not be evaluated. In addition to tire stiffness, the precision of modeling the torque

^Q The simulated force peak of RF tire hitting bump no. 1 is, however, narrower than the measured one, thus containing less energy.

^R The exact position of the grapple in the load space during measurement is also unknown.

^S As was stated in Section 4.9, the studied machine does not have a suspension system in addition to the tires; this is why correct stiffness of the tires is crucial.

transmitted to tires via the power train was found to be a major contributor in the resulting tire forces^T (see Sections 4.1 and 6.5). Tire friction depends on ambient conditions, thus the values of friction coefficients have to be more or less “guessed”. A sensitivity analysis (see Section 5.4.4) showed that the magnitudes of the force peaks are sensitive to the used values of friction coefficients.

The stress levels of the rear frame and load space were observed to be governed by the forces exerted from the weight of the cargo. The rear frame stresses had larger oscillations due to the tire forces compared to the stresses on the load space (see Section 5.2). Since shell elements with coarse discretization were used, the results of local stress concentrations are not accurate.

The force results of this simulation can be used as boundary conditions in a consequent implicit fatigue analysis for which a workflow is suggested in Section 6.3. The model built in this work can also be used as a basis for simulating other load cases such as cargo loading (Section 6.1), collisions (Section 6.2) and ROPS/FOPS cases (Section 6.6). Studying other machine sizes in the product family (and possibly other product families) would be efficient since methods are now developed (Section 6.4).

Controlling the tire high frequency vibrations proved to be a challenging task and therefore the tire model requires some further development if it is desired to be used in a simulation with a long duration. Energy ratio and amount of mass scaling start to dramatically rise after the tires begin to rupture, both of which in conjunction with the rupture itself will eventually invalidate the results (this happens approximately after 5 seconds of simulation). The use of solid elements in the tires instead of shell elements might solve this problem and testing them should be the next step in improving the model (see Section 6.7).

^T Unfortunately, due to instabilities of the differential mechanism, no sensible comparison between different methods of applying tire rotation could be made.

REFERENCES

- [1] ANSYS Inc., ANSYS Help 16.1 help/ans_elem/Hlp_E_ElemTOC.html, 2015.
- [2] ANSYS Inc., ANSYS Help 16.1 help/ans_lsd/Hlp_G_LsdTOC.html, 2015.
- [3] ANSYS Inc., ANSYS Help 16.1 help/ans_thry/thy_str1.html, 2015
- [4] ANSYS Inc., ANSYS Help 16.1 help/wb_sim/ds_Home.html, 2015
- [5] ANSYS Inc., ANSYS Help 16.1 help/wb_sim/exp_dyn_theory.html, 2015.
- [6] ANSYS Inc., ANSYS Help 16.2 help/ans_adv/Hlp_G_ADV4.html, 2015.
- [7] ANSYS Inc., ANSYS Help 16.2 help/ans_thry/thy_anproc2.html, 2015.
- [8] ANSYS Inc., Information for Media, 2012
- [9] Austrell P. E., Modeling of Elasticity and Damping for Filled Elastomers, Report TVSM-1009, Division of Structural Mechanics, Lund University, 1997, 210 p. Available (accessed 26.10.2015):
<http://www.byggmek.lth.se/fileadmin/byggnadsmekanik/publications/tvsm1000/web1009.pdf>
- [10] Bala S., Limitations of Penalty Joint Treatment in LS-DYNA, 2006. Available (accessed 2.2.2016): <http://www.d3view.com/119rigidbody-joints-in-ls-dyna/>
- [11] Barsotti M., Optimization of a Passive Aircraft Arrestor with a Depth-varying Crushable Material Using a Smoothed Particle Hydrodynamics (SPH) Model, The University of Texas, 2008, 227 p. Available (accessed 8.4.2016):
<https://books.google.fi/books?id=SVzNXayvLcsC&pg=PA40&lpg=PA40&dq=s+hell+16+%22full+projection+warping+stiffness%22&source=bl&ots=DnENqo-sSe&sig=xIJxCWM5ZuGWDC6P0FXHpeusiE8&hl=fi&sa=X&ved=0ahUKEwiij5nIm-rLAh-VBkywKHWq8B5cQ6AEIIDAB#v=onepage&q=shell%2016%20%22full%20projection%20warping%20stiffness%22&f=false>
- [12] Bathe K. J., Ramm E. and Wilson E. L., Finite Element Formulations for Large Deformation Dynamic Analysis, International Journal for Numerical Methods in Engineering, Vol. 9, 1975, pp. 353-386. Available (accessed 26.11.2015):
http://web.mit.edu/kjb/www/Publications_Prior_to_1998/Finite_Element_Formulations_for_Large_Deformation_Dynamic_Analysis.pdf

- [13] Bischoff M., Modeling of Shells With Three-dimensional Finite Elements, Institute of Structural Mechanics, University of Stuttgart, 2008, 81 p. Available (accessed 21.10.2015):
https://ecommons.cornell.edu/bitstream/1813/11662/8/04_Plenary_by_Bischoff.pdf
- [14] Blundell M., Lecture 5- Tyre Modelling, 2012, 59 p. Available (accessed 8.4.2016):
https://www.google.fi/url?sa=t&rct=j&q=&esrc=s&source=web&cd=2&cad=rja&uact=8&ved=0ahUKEwjw0-SH-P7LAhWDOSwKHdqODaMQFggjMAE&url=http%3A%2F%2Fmech.unibg.it%2F~lorenzi%2FVD%26S%2FProf_Blundell_Lect%2FBergamo%2520Lecture%25205%2520-%2520Tyre%2520Modelling.ppt&usg=AFQjCNF-vYmK67RDjNeUsWA4gfUq7zNERw&sig2=tKIH_Yxab9HB0dKYFnecCw
- [15] Calladine C. R., Theory of Shell Structures, Cambridge University Press, Cambridge, 1983, 763 p.
- [16] Conover D., Verification and Validation of FEA Simulations, ANSYS Inc., 2008
- [17] Courant R., Friedrichs K. and Lewy H., On the Partial Difference Equations of Mathematical Physics, IBM Journal of Research and Development, Volume 11 Issue 2, Pages 215-234, 1967.
- [18] Crisfield M. A., Non-Linear Finite Element Analysis of Solids and Structures Vol.1: Essentials, ISBN 047197059X, Wiley, 1996, 360 p.
- [19] Dassault Systèmes, Abaqus 6.13 Theory Guide, 2013.
- [20] Deere & Company, Feet on the Ground, Eyes on the Horizon, Annual Report 2014. Available (accessed on 3.10.2015):
https://investor.deere.com/files/doc_financials/annual_reports/2015/2014_annual_report_v001_g1fx1i.pdf
- [21] Deere & Company, John Deere History. Available (accessed on 3.10.2015):
http://www.deere.fi/en_US/corporate/our_company/about_us/history/timeline/timeline.page?
- [22] Do I. and Day J., Overview of ALE Method in LS-DYNA, Livermore Software Technology Corporation, 2005.
- [23] DYNAmore GmbH, Energy Data. Available (accessed 22.4.2016):
<http://www.dynasupport.com/tutorial/ls-dyna-users-guide/energy-data>

- [24] DYNAmore GmbH, Shell Formulations. Available (accessed 29.3.2016): <http://www.dynasupport.com/howtos/element/shell-formulations>
- [25] Erhart T. and Borrvall T., Drilling Rotation Constraint for Shell Elements in Implicit and Explicit Analyses, 9th European LS-DYNA Conference, 2013, 22 p. Available (accessed 28.3.2016): <https://www.dynamore.de/de/download/papers/2013-ls-dyna-forum/documents/drilling-rotation-constraint-for-shell-elements-in-implicit-and-explicit-analyses>
- [26] Eskelinen J., Metsäkoneiden Panssareiden ja Pohjan Luukkujen Laadun Kehittäminen, Lappeenranta University of Technology, Mechanical Engineering, 2015, 130 p. Available (accessed 7.1.2016): <http://urn.fi/URN:NBN:fi-fe201505198497>
- [27] Fricke W., Guideline for the Fatigue Assessment by Notch Stress Analysis for Welded Structures, IIW-Doc. XIII-2240r2-08/XV-1289r2-08, Hamburg University of Technology, 2010, 38 p.
- [28] Green D. W., Winandy J. E. and Kretschmann D. E., Mechanical Properties of Wood, Forest Products Laboratory, 1999, 45 p. Available (accessed 30.10.2015): <http://www.fpl.fs.fed.us/documnts/fplgtr/fplgtr113/ch04.pdf>
- [29] Håkansson P., Finite Element Modelling of a Rubber Block Exposed to Shock Loading, Department of Mechanics and Materials, Lund University, 2000, 76 p. Available (accessed 26.10.2015): <http://www.solid.lth.se/fileadmin/hallfasthetslara/utbildning/examensarbete/TFH F5087.pdf>
- [30] Hall W., Mottram J. T. and Jones R. P., Tire Modeling Methodology with the Explicit Finite Element Code LS-DYNA, School of Engineering, University of Warwick, Coventry, 45 p. Available (accessed 24.10.2015): https://www.researchgate.net/publication/274412057_Tire_Modeling_Methodology_with_the_Explicit_Finite_Element_Code_LSDYNA
- [31] Ikonen K., Levy- Laatta- Ja Kuoriteoria, ISBN 951-672-111-7, Otatiето Oy, Helsinki, 1990, 333 p.
- [32] Indian Institute of Technology Delhi, Finite Element Analytical Techniques and Applications to Structural Design, Available (accessed on 24.9.2015): http://web.iitd.ac.in/~achawla/public_html/736/9-Finite_Element_analytical_tecniques.pdf

- [33] John Deere Forestry Oy, John Deere 1010E Forwarder product page. Available (accessed on 22.9.2015):
http://www.deere.fi/fi_FI/products/equipment/forwarders/1010e/1010e.page?
- [34] John Deere Forestry Oy, John Deere History. Available (accessed on 3.10.2015):
http://www.deere.fi/en_US/industry/forestry/learn_more/about_construction_and_forestry/history/history.page
- [35] Katona M. G., Thompson R. and Smith J., Efficiency Study of Implicit and Explicit Time Integration Operators for Finite Element Applications, Civil Engineering Laboratory, California, 1977, 26 p. Available (accessed 4.2.2016):
<http://www.dtic.mil/dtic/tr/fulltext/u2/a043968.pdf>
- [36] Kaw A. K., Mechanics of Composite Materials, Second Edition, Taylor & Francis Group, 2006, 473 p. Available (accessed 11.2.2016):
http://www.rjafari.iut.ac.ir/sites/rjafari.iut.ac.ir/files//files_course/1mechanics_of_composite_materials.pdf
- [37] Kouhia R. and Tuomala M., Rakennetekniikan Numeeriset Menetelmät, Luentomoniste, 2009, 427 p.
- [38] Larsson S., Characterization and Modeling of Rock Impact on Steel Plates, Luleå University of Technology, Department of Engineering Sciences and Mathematics, Division of Mechanics of Solid Materials, 2014, 86 p. Available (accessed 8.1.2016): <https://pure.ltu.se/portal/files/96975337/LTU-EX-2014-96944214.pdf>
- [39] Larsson, J., EDR&Medeso support, private e-mail conversation, 2016
- [40] Li H., Analysis of Off-Road Tire-Soil Interaction through Analytical and Finite Element Methods, Vom Fachbereich Maschinenbau und Verfahrenstechnik der Technischen Universität Kaiserslautern zur Verleihung des akademischen Grades, 2013, 181 p. Available (accessed 8.1.2016): <http://nbn-resolving.de/urn/resolver.pl?urn:nbn:de:hbz:386-kluedo-36443>
- [41] Li H., Kwasniewski L., Malachowski J. and Wekezer J., Development of Finite Element Models of Heavy Vehicles, Department of Civil and Environmental Engineering, FAMU – FSU College of Engineering, 10 p. Available (accessed 22.10.2015): <http://road-transport-technology.org/Proceedings/9%20-%20ISHVWD/Session%209/Development%20of%20Finite%20Element%20Models%20of%20Heavy%20Vehicles%20-%20Li.pdf>
- [42] Livermore Software Technology Corporation (LSTC), LS-DYNA Support, Double Precision. Available (accessed 12.1.2016):
<http://www.dynasupport.com/howtos/general/double-precision>

- [43] Livermore Software Technology Corporation (LSTC), LS-DYNA® Keyword User's Manual, Volume II, Material Models (r: 5442), 2014, 1265 p. Available (accessed 22.2.2016): <http://www.dynasupport.com/manuals>
- [44] Livermore Software Technology Corporation (LSTC), LS-DYNA® Keyword User's Manual, Volume I, (r: 5471), 2014, 2281 p. Available (accessed 22.2.2016): <http://www.dynasupport.com/manuals>
- [45] Livermore Software Technology Corporation (LSTC), LS-DYNA® Keyword User's Manual, Volume I, (r: 6319), 2015, 2482 p. Available (accessed 22.2.2016): <http://www.dynasupport.com/manuals>
- [46] Livermore Software Technology Corporation (LSTC), LS-DYNA® Theory Manual (r: 6702), 2015, 862 p. Available (accessed 22.2.2016): <http://www.dynasupport.com/manuals>
- [47] Mohsenimanesh A., Ward S. M. and Gilchrist M. D., Stress Analysis of a Multi-Laminated Tractor Tyre Using Non-Linear 3D Finite Element Analysis, *Materials and Design* 30, 2009, pp. 1124-1132. Available (accessed 8.2.2016): <http://citeseerx.ist.psu.edu/viewdoc/download?doi=10.1.1.552.5984&rep=rep1&type=pdf>
- [48] Mooney M., A Theory of Large Elastic Deformation, *Journal of Applied Physics*, 11(9), 1940, pp. 582-592
- [49] Nikishkov G. P., Introduction to the Finite Element Method, University of Aizu, 2004. Available (accessed 9.10.2015): <http://homepages.cae.wisc.edu/~suresh/ME964Website/M964Notes/Notes/introfem.pdf>
- [50] Nokian Heavy Tyres Technical manual / Forestry tyres 3.0.1, 2014. Available (accessed 26.10.2015): http://www.nokianheavytyres.us/files/nht/technical_manual/NokianHeavyTyres_Technical_manual_03_Forestry_20140609.pdf
- [51] Pearlman A., How a Differential Works, Massachusetts Institute of Technology, 1999. Available (accessed 11.1.2016): <http://web.mit.edu/2.972/www/reports/differential/differential.html>
- [52] Pulkki R., Cut-to-length, Tree Length or Full Tree Harvesting?, Lakehead University, Faculty of Forestry, Available (accessed 28.9.2015): <http://www.borealforest.org/world/innova/compare.htm>
- [53] Reid J. D., Boesch D. A. and Bielenberg R. W., Detailed Tire Modeling for Crash Applications, ICrash 2006, Athens Greece, 4th-7th July 2006, 11 p. Availa-

ble (accessed 28.3.2016):

<http://citeseerx.ist.psu.edu/viewdoc/download?doi=10.1.1.477.7263&rep=rep1&type=pdf>

- [54] Rivlin R. S., Large Elastic Deformations of Isotropic Materials. IV. Further Developments of The General Theory, Philosophical Transactions of the Royal Society of London. Series A, Mathematical and Physical Sciences, 241(835), 1948, pp. 379-397
- [55] Salmi T. and Kuula K., Rakenteiden mekaniikka, Pressus Oy, Tampere, 2012
- [56] Salmi T., 23140 Rakenteiden Dynamiikka, Luennot kl. 2003, Tampere, 2003, 175 p.
- [57] Sargent R. G., Verification and Validation of Simulation Models, Proceedings of the 2011 Winter Simulation Conference, 2011, pp. 39-48. Available (accessed 26.11.2015): <http://www.courses.vcu.edu/MATH-jrm/OPER641/Papers/ValidationVerification.pdf>
- [58] Shen R.W. and Lei G., Introduction to the Explicit Finite Element Method for Non-linear Transient Dynamics, New Jersey, John Wiley & Sons Inc., 2012, 352 p.
- [59] Shiraishi M., Yoshinaga H., Iwasaki N. and Hayashi K., Making FEM Tire Model and Applying it for Durability Simulation, Sumimoto Rubber Industries, 2000, 22 p. Available (accessed 9.11.2015): <http://www.dynalook.com/international-conf-2000/session2-3.pdf>
- [60] Shokouhfar S., Rakheja S. and El-Gindy M., Verification of the Part-Composite Approach for Modeling the Multi-Layered Structure of a Rolling Truck Tire, 10th European LS-DYNA Conference, Würzburg, 2015, 12 p. Available (accessed 9.11.2015): <https://www.dynamore.de/de/download/papers/2015-ls-dyna-europ/documents/sessions-g-5-8/verification-of-the-part-composite-approach-for-modeling-the-multi-layered-structure-of-a-rolling-truck-tire>
- [61] Smith W., Melanz D., Senatore C., Iagnemma K., and Peng H., Comparison of DEM and Traditional Modeling Methods for Simulating Steady-State Wheel-Terrain Interaction for Small Vehicles, Department of Mechanical Engineering, University of Michigan, 2013, 16 p. Available (accessed 8.1.2016): http://web.mit.edu/mobility/publications/Comparison_of_DEM_and_Traditional_ISTVS_2013.pdf
- [62] Steele C. R. and Balch C. D., Introduction to the Theory of Plates, Division of Mechanics and Computation, Department of Mechanical Engineering, Stanford

- University, 41 p. Available (accessed 14.10.2015):
<http://web.stanford.edu/~chasst/Course%20Notes/Introduction%20to%20the%20Theory%20of%20Plates.pdf>
- [63] Szurgott P., Kwasniewski L. and Wekezer J. W., Dynamic Interaction Between Heavy Vehicles and Speed Bumps, Military University of Technology, 2009, 7 p. Available (accessed 22.10.2015): http://www.scs-europe.net/conf/ecms2009/ecms2009%20CD/ecms2009%20accepted%20papers/ese_0005_47bbe86c.pdf
- [64] Vainionpää, T. Nokian Tyres, private e-mail conversation, 2015
- [65] Valkila J., 2015_1010G_NGtakarunko_painopöytäkirja, John Deere Forestry Oy, 2015
- [66] Ventsel E., Krauthammer T., Thin Plates and Shells - Theory, Analysis, and Applications, The Pennsylvania State University, 2001, 651 p. Available (accessed 26.5.2016):
https://www.google.com/url?sa=t&rct=j&q=&esrc=s&source=web&cd=5&ved=0ahUKEwicnNiTtvfMAhVMGZoKHxzmAiwQFghGMAQ&url=http%3A%2F%2Fnumgeom.ams.sunysb.edu%2Ffrac%2Fraw-attach-ment%2Fwiki%2Fshells%2FThinPlatesAndShellsTheoryAnalysisAndApplications.pdf&usq=AFQjCNFYC94EYSYAEdkxRQGVidBIPGavCw&sig2=KfcVm0-q_xk2QQEyesJsIw&bvm=bv.122852650,d.bGs&cad=rja
- [67] Wriggers P., Non-Linear Finite Element Methods, ISBN 978-3-540-71000-4, Springer, Verlag Berlin Heidelberg, 2008, 566 p. Available (accessed 26.11.2015):
https://www.researchgate.net/publication/51992328_Nonlinear_Finite_Element_Methods
- [68] Zienkiewicz O. C. and Taylor R. L., The Finite Element Method for Solid and Structural Mechanics, Sixth Edition, Butterworth-Heinemann, 2005, 654 p.
- [69] Zienkiewicz O. C. and Taylor R. L., The Finite Element Method, Fifth Edition, Volume 1: The Basis, Butterworth-Heinemann, 2000, 708 p.

APPENDIX A GENERAL CONTROLS, LS-DYNA INPUT

```

$# LS-DYNA Keyword file
*KEYWORD
*DATABSE_FORMAT
$  iform  ibinary                                unused
  0      0
*CONTROL_TERMINATION
$  endtim  endcyc  dtmin  endeng  endmas                                unused
  6      1000000  0.001  0      100000
*CONTROL_TIMESTEP
$  dtinit  tssfacs  isdo  tslimt  dt2ms  lctm  erode  ms1st
  0      0.9      0      0      0      0      1      0
$  dt2msf  dt2mslc  imsc1
  0      0      0
*CONTROL_CONTACT
$  slsfacs  rwnpal  islchk  shlthk  penopt  thkchg  orien  enmass
  0      0      1      1      1      0      2      0
$  usrstr  usrfric  nsbcs  interm  xpene  ssthk  ecdt  tiedprj
  0      0      0      0      0      0      0      0
$  sfric  dfric  edc  vfc  th  th_sf  pen_sf  unused
  0      0      0      0      0      0      0      0
$  ignore  frceng  skiprwg  outseg  spotstp  spotdel  spothin  unused1
  2      1      0      1      0      1      0.5
$  isym  nserod  rwgaps  rwgdt  rwksf  icov  swradf  ithoff
  0      0      0      0      0      0      0      0
$  shldg  pstiff  ithcnt  tdcnof  ftall
  1      0      0      0      1
*CONTROL_ENERGY
$  hgen  rwen  slnten  rylen                                unused
  2      2      2      2
*CONTROL_ACCURACY
$  osu  inn  pidosu                                unused
  1      4      0
*CONTROL_BULK_VISCOSITY
$  q1  q2  type                                unused
  1.5  0.06  -2
*CONTROL_SOLID
$  esort  fmatrx  niptets  swloc1                                unused
  1      0      0      0
$  pm1  pm2  pm3  pm4  pm5  pm6  pm7  pm8  pm9  pm10
  0      0      0      0      0      0      0      0      0      0
*CONTROL_SHELL
$  wrpang  esort  irnxx  istupd  theory  bwc  miter  proj
  20      1      -1      4      2      1      1      1
$  rotasc1  intgrd  lamsht  cstyp6  tshell  nfail1  nfail4  psnfail
  0      0      0      0      0      1      1      0
$  pstupd  irquad  cntco
  0      0      2
*CONTROL_OUTPUT
$  npopt  neecho  nrefup  iaccop  opifs  ipnint  ikedit  iflush
  1      0      0      0      0      0      0      0
$  iprtf  ierode  tet10  msgmax  ipcurv
  0      0      0      0      0
*CONTROL_PARALLEL
$  ncpu  numrhs  consti  para                                unused
  0      0      1      0
*CONTROL_SOLUTION
$  soln  nlq  isnan  lcint                                unused
  0      0      0
*CONTROL_HOURLASS
$  ihq  qh                                unused1
  2      0.05
*CONTROL_ALE
$  dct  nadv  meth  afac  bfac  cfac  dfac  efac
  0      1      1      -1      0      0      0      0
$  start  end  aafac  vfact  prit  ebc  pref  nsidebc
  0      1E+20  0      0      0      0      0      0
*CONTROL_RIGID
$  lmf  jntf  orthmd  partm  sparse  metalf  plotel  rbsms
  1      0      0      0      0      0      0      0

```

APPENDIX B MANUAL INPUT, RELATIVE DAMPING

```

$***** RELATIVE DAMPING start *****
$***** Create Load Curve *****
*DEFINE_CURVE
$ LCID, SIDR, SCLA, SCLO, OFFA, OFFO
2001,
$ ABSCISSA, ORDINATE
0,10
0.5,10
0.51,5
0.52,0
6,0
$***** End of Create Load Curve *****
*DAMPING_RELATIVE
, 40, 680, 688,, 2001
*DAMPING_RELATIVE
, 40, 682, 690,, 2001
*DAMPING_RELATIVE
, 40, 681, 689,, 2001
*DAMPING_RELATIVE
, 40, 683, 691,, 2001
*DAMPING_RELATIVE
, 40, 684, 692,, 2001
*DAMPING_RELATIVE
, 40, 686, 694,, 2001
*DAMPING_RELATIVE
, 40, 685, 693,, 2001
*DAMPING_RELATIVE
, 40, 679, 687,, 2001
*SET_PART_LIST
688, 0, 0, 0, 0, MECH
688, 0, 0, 0, 0, 0, 0, 0
*SET_PART_LIST
690, 0, 0, 0, 0, MECH
690, 0, 0, 0, 0, 0, 0, 0
*SET_PART_LIST
689, 0, 0, 0, 0, MECH
689, 0, 0, 0, 0, 0, 0, 0
*SET_PART_LIST
691, 0, 0, 0, 0, MECH
691, 0, 0, 0, 0, 0, 0, 0
*SET_PART_LIST
692, 0, 0, 0, 0, MECH
692, 0, 0, 0, 0, 0, 0, 0
*SET_PART_LIST
694, 0, 0, 0, 0, MECH
694, 0, 0, 0, 0, 0, 0, 0
*SET_PART_LIST
693, 0, 0, 0, 0, MECH
693, 0, 0, 0, 0, 0, 0, 0
*SET_PART_LIST
687, 0, 0, 0, 0, MECH
687, 0, 0, 0, 0, 0, 0, 0
$***** RELATIVE DAMPING end *****

```

APPENDIX C MANUAL INPUT, MASS DAMPING

```
$***** MASS DAMPING start *****
$***** Create Load Curve *****
*DEFINE_CURVE
$ LCID, SIDR, SCLA, SCLO, OFFA, OFFO
2002,
$ ABSCISSA, ORDINATE
0,1680.5259
0.5,1680.5259
0.51,420.1315
0.52,42.0131
6,42.0131
$***** End of Create Load Curve *****
*DAMPING_PART_MASS
573,2002,1
*DAMPING_PART_MASS
574,2002,1
*DAMPING_PART_MASS
575,2002,1
*DAMPING_PART_MASS
576,2002,1
*DAMPING_PART_MASS
577,2002,1
*DAMPING_PART_MASS
578,2002,1
$***** MASS DAMPING end *****
```


APPENDIX D MANUAL INPUT, DIFFERENTIAL GEAR

```

$***** REAR DIFFERENTIAL start *****
$***** Create Joint RIGHT_side_gear_out to Differential_pinion_right *****
*CONSTRAINED_JOINT_COOR_GEAR_ID
$ ID, HEADING
1000,RIGHT_side_gear_out_to_Differential_pinion_right
$ RBID_A,RBID_B,RPS,DAMP,TMASS,RMASS
729,718,0.1,,
$X,Y,Z
0,-50,-16.999
50,0,-16.999
0,-100,-16.999
100,0,-16.999
35.355,-50,18.356
50,35.355,18.356
$# PARM, LCID, TYPE, R1
1,,50
$***** End of Create Joint RIGHT_side_gear_out to Differential_pinion_right *****
$***** Create Joint Differential_pinion_left to LEFT_side_gear_out *****
*CONSTRAINED_JOINT_COOR_GEAR_ID
$ ID, HEADING
1001,Differential_pinion_left_to_LEFT_side_gear_out
$ RBID_A,RBID_B,RPS,DAMP,TMASS,RMASS
743,727,0.1,,
$X,Y,Z
50,0,-16.999
0,50,-16.999
100,0,-16.999
0,100,-16.999
50,35.355,18.356
35.355,50,18.356
$# PARM, LCID, TYPE, R1
1,,50
$***** End of Create Joint Differential_pinion_left to LEFT_side_gear_out *****
$***** Create Joint LEFT_side_gear_LF to LF_rim_in *****
*CONSTRAINED_JOINT_COOR_PULLEY_ID
$ ID, HEADING
1002,LEFT_side_gear_LF_to_LF_rim_in
$ RBID_A,RBID_B,RPS,DAMP,TMASS,RMASS
725,744,0.1,,
$X,Y,Z
0,50,-16.999
700,1055,-192
0,100,-16.999
700,1105,-192
35.355,50,18.356
735.355,1055,-156.645
$# PARM, LCID, TYPE, R1
1,,50
$***** End of Create Joint LEFT_side_gear_LF to LF_rim_in *****
$***** Create Joint LEFT_side_gear_LR to LR_rim_in *****
*CONSTRAINED_JOINT_COOR_PULLEY_ID
$ ID, HEADING
1003,LEFT_side_gear_LR_to_LR_rim_in
$ RBID_A,RBID_B,RPS,DAMP,TMASS,RMASS
726,747,0.1,,
$X,Y,Z
0,50,-16.999
-700,1055,-192
0,100,-16.999
-700,1105,-192
35.355,50,18.356
-664.645,1055,-156.645
$# PARM, LCID, TYPE, R1
1,,50
$***** End of Create Joint LEFT_side_gear_LR to LR_rim_in *****
$***** Create Joint RIGHT_side_gear_RF to RF_rim_in *****
*CONSTRAINED_JOINT_COOR_PULLEY_ID
$ ID, HEADING
1004,RIGHT_side_gear_RF_to_RF_rim_in
$ RBID_A,RBID_B,RPS,DAMP,TMASS,RMASS
730,745,0.1,,
$X,Y,Z
0,-50,-16.999
700,-1055,-192
0,-100,-16.999
700,-1105,-192
35.355,-50,18.356
735.355,-1055,-156.645
$# PARM, LCID, TYPE, R1
1,,50
$***** End of Create Joint RIGHT_side_gear_RF to RF_rim_in *****
$***** Create Joint RIGHT_side_gear_RR to RR_rim_in *****
*CONSTRAINED_JOINT_COOR_PULLEY_ID
$ ID, HEADING
1005,RIGHT_side_gear_RR_to_RR_rim_in
$ RBID_A,RBID_B,RPS,DAMP,TMASS,RMASS
728,746,0.1,,
$X,Y,Z
0,-50,-16.999
-700,-1055,-192
0,-100,-16.999

```

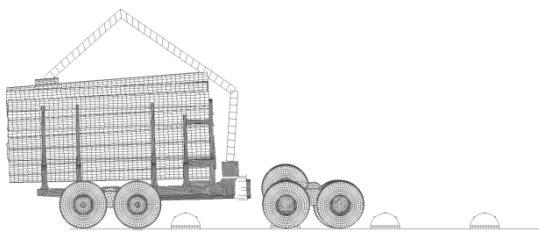
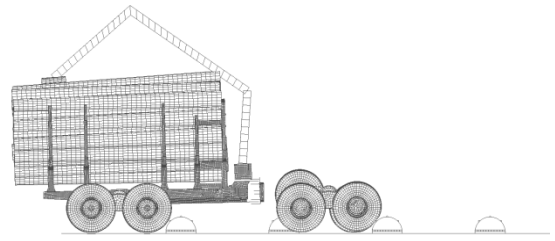
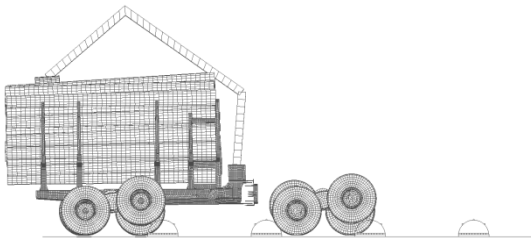
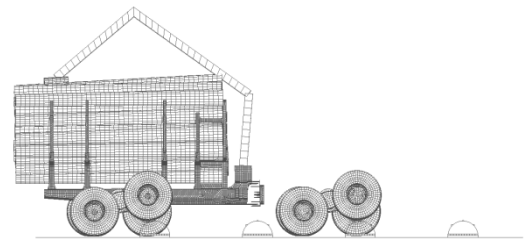
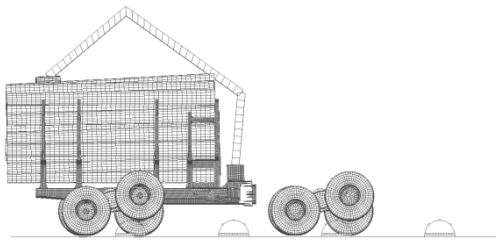
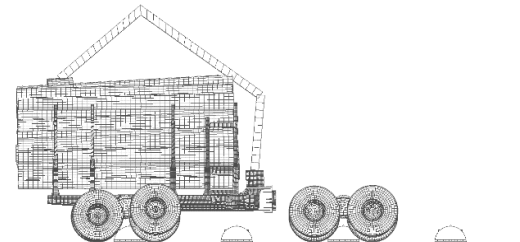
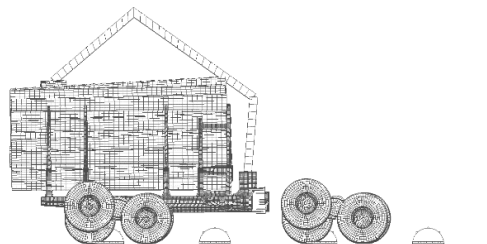
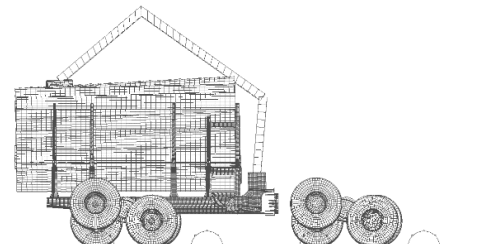
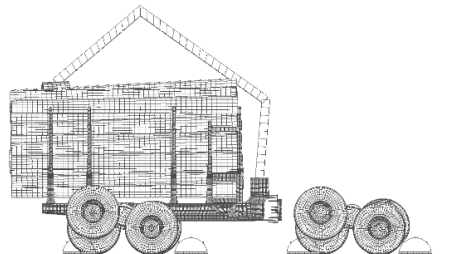
```

-700,-1105,-192
35.355,-50,18.356
-664.645,-1055,-156.645
$# PARM, LCID, TYPE, R1
1,,50
$***** End of Create Joint RIGHT_side_gear_RR to RR_rim_in *****
$***** Create Load Curve 2000 *****
*DEFINE_CURVE
$ LCID, SIDR, SCLA, SCLO, OFFA, OFFO
2000,
$ ABSCISSA, ORDINATE
0,0
0.3,0
0.3,-1.2647
6,-1.2647
$***** End of Create Load Curve 2000 *****
$***** Create Joint Ring_gear_inner to Housing *****
*CONSTRAINED_JOINT_COOR_ROTATIONAL_MOTOR_ID
$ ID, HEADING
1006, Ring_gear_inner_to_Housing
$ RBID_A, RBID_B, RPS, DAMP, TMASS, RMASS
722,10,0.1,,
$X,Y,Z
0,-50,-16.999
0,-50,-16.999
0,-100,-16.999
0,-100,-16.999
35.355,-50,18.356
35.355,-50,18.356
$# PARM, LCID, TYPE, R1
,2000,0,
$***** End of Create Joint Ring_gear_inner to Housing *****
$***** REAR DIFFERENTIAL end *****

```

APPENDIX E MANUAL INPUT, TORQUE LIMITER

```
$***** Create Restrict torque on differential *****
$ Track torque input to differential
*SENSOR_DEFINE_FORCE
$ SENSID, FTYPE, TYPEID, VID, CRD
1007, JOINT,1006, YMOMENT,
$ Set maximum allowable torque
*SENSOR_SWITCH
$ SWITID, TYPE, SENSID, LOGIC, VALUE, FILTRID, TIMWIN
1008,SENSOR,1007,GT,22875000,,0.000045
$ Control constant rotational velocity of the differential (constant velocity terminated when torque exceeds maximum)
*SENSOR_CONTROL
$ CNTLID, TYPE, TYPEID, TIMEOFF, NREP
1010, JOINT,1006,0,-1
$ INITSTT, SWIT1, SWIT2, SWIT3, SWIT4, SWIT5, SWIT6, SWIT7
On,1008,
$***** End of Create Restrict torque on differential *****
```

APPENDIX F ANALYSIS WALKTHROUGH $t = 0 \text{ s}$  $t = 0.5 \text{ s}$  $t = 1 \text{ s}$  $t = 1.5 \text{ s}$  $t = 2 \text{ s}$  $t = 2.5 \text{ s}$  $t = 3 \text{ s}$  $t = 3.5 \text{ s}$  $t = 4 \text{ s}$